Strål säkerhets myndigheten
Swedish Radiation Safety Authority

2019:16

SSM's external experts' reviews of SKB's safety assessment SR-PSU –
consequence analysis and hydrogeological aspects
Main review phase

SSM perspective

Background

The Swedish Radiation Safety Authority (SSM) received an application for the expansion of SKB's final repository for low and intermediate level waste at Forsmark (SFR) on the 19 December 2014. SSM is tasked with the review of the application and will issue a statement to the government who will decide on the matter. An important part of the application is SKB's assessment of the long-term safety of the repository, which is documented in the safety analysis named SR-PSU.

The present report compiles results from SSM's external experts' reviews of SR-PSU during the main review phase. The general objective of these reviews has been to give support to SSM's assessment of the license application. More specifically, the instructions to the external experts have been to make an in depth assessment of the specific issues defined for the different disciplines.

Project information

Contact person at SSM: Henrik Öberg

Contact persons and registration numbers for the different review contributions are given in the report.

Table of contents

Strål säkerhets myndigheten

Swedish Radiation Safety Authority

2019:16

SSM's external experts' reviews of SKB's safety assessment SR-PSU – consequence analysis and hydrogeological aspects
Main review phase

This report concerns a study which has been conducted for the Swedish Radiation Safety Authority, SSM. The conclusions and viewpoints presented in the report are those of the author/authors and do not necessarily coincide with those of the SSM.

Authors: Rebecca Newson[1] and George Towler[1]
[1]Quintessa Limited, Henley on Thames, UK

Further review of 1BMA and updated 2BMA design – Main review phase

Abstract

The Swedish Radiation Safety Authority (SSM) received an application for the expansion of SKB's final repository for low and intermediate level waste at Forsmark (SFR) on 19 December 2014. SSM is tasked with the review of the application and will issue a statement to the government who will decide on the matter. An important part of the application is SKB's assessment of the long-term safety of the repository, which is documented in the safety analysis named SR-PSU.

SSM's review is divided into an initial review phase and a main review phase. This assignment contributes to the main review phase. In a study already undertaken as part of the main review phase, some of SKB's radionuclide transport models were reimplemented using the information provided in the SR-PSU documentation. The results were compared with the results of SKB's models, and model sensitivity and reasons for differences in the results were explored. The models reimplemented were SKB's near-field model for the proposed 2BMA vault, and SKB's model for the geosphere. SKB used the ECOLEGO code. The models were reimplemented using the AMBER code.

This assignment explores key issues that have emerged during the main review phase, and the implications of recent further design and assessment work undertaken by SKB for the 2BMA vault. This assignment includes two tasks:
1. Reimplementing SKB's models for the 1BMA vault to explore some of the key SR-PSU results. In particular, to explore the role of the 1BMA concrete structure as a barrier to radionuclide release from the vault.
2. Reimplementing SKB's models of an updated design for the 2BMA vault.

An additional task was then undertaken to investigate the effect of removing the grout around the bitumen-solidified wastes in the 1BMA vault.

For both tasks SKB's models have been reimplemented in AMBER. The AMBER models used in this assignment represent a single concrete compartment (1BMA) or caisson (2BMA). The 1BMA AMBER models broadly reproduce SKB's results, but generally give higher peak fluxes than SKB's ECOLGEO models. This may be an artefact of only representing a single concrete compartment, so retardation of radionuclides by transport through downgradient compartments is not modelled. (This process is likely less significant for 2BMA, where the caissons are separated by Macadam backfill).

The AMBER models confirm that the concrete walls in the 1BMA vault are a key barrier to radionuclide transport. However, the radionuclide fluxes from the 1BMA vault to the geosphere are less sensitive to fracturing of the walls than for the 2BMA vault. The difference seems to be due to the greater concentrations of organic complexing agents in 1BMA compared with 2BMA. Cracking of the concrete walls results in transport through the walls without sorption. Complexing agents reduce sorption onto the concrete walls, and therefore as complexation increases, sensitivity to cracking of the walls decreases. The treatment of organic complexation in SKB's models, particularly apparent differences in the treatment of complexation in 1BMA and 2BMA, would benefit from clarification.

Removal of grout from around the bitumen-solidified waste packages in the 1BMA vault increases the flux of high-sorbing radionuclides to the geosphere. Radionuclides which do not sorb strongly to cement are not significantly affected by removal of the grout. However, the calculations do not include the impact of

removing the grout on water flows through the wastes. Removing the grout could increase water flows through the wastes, and further increase the releases of all radionuclides.

SKB's assessment shows that the new design for 2BMA has little impact on the radionuclide fluxes from the near-field to the geosphere. Therefore, the calculated doses are little changed compared with SR-PSU. We found that the new design results in increased radionuclide fluxes from the near-field to the geosphere. The magnitude of the increase is small for radionuclides that do not sorb onto cement, but larger for radionuclides that sorb strongly onto cement. The main cause of the increased fluxes is removal of the grout fill around the waste packages, inside the caisson. So, there is no grout for radionuclides to sorb onto. It is not clear whether the grout has been removed from SKB's models of the new 2BMA design.

Contents

1 Introduction

The Swedish Radiation Safety Authority (SSM) has received an application for the expansion of SKB's final repository for low and intermediate level waste at Forsmark (SFR) on 19 December 2014. SSM is tasked with the review of the application and will issue a statement to the government who will decide on the matter. An important part of the application is SKB's assessment of the long-term safety of the repository, which is documented in the safety analysis named SR-PSU.

SSM's review is divided into an initial review phase and a main review phase. This assignment contributes to the main review phase.

Earlier in the main review phase, Towler and Penfold (2017a) reimplemented some of SKB's radionuclide transport models using the information provided in the SR-PSU documentation. The results were compared with the results of SKB's models, and model sensitivity and reasons for differences in the results were explored. Towler and Penfold (2017a) reimplemented SKB's near-field model for the proposed 2BMA vault, and SKB's model for the geosphere. Towler and Penfold (2017a) implemented the models using the AMBER code (Quintessa, 2016), while SKB used the ECOLEGO code[1].

This assignment explores key issues that have emerged during the main review phase, and the implications of recent further design and assessment work, undertaken by SKB for the 2BMA vault. This assignment includes two tasks.

The 1BMA vault concrete structure and 2BMA concrete caissons have been identified as key features for containment of radionuclides. Defects have been identified in the concrete structure in the existing 1BMA vault. The scope of the first task is to understand the potential impacts of the defects further, by reimplementing SKB's near-field radionuclide transport model for a single concrete compartment in the 1BMA vault and:
   a. Comparing the radionuclide fluxes from the near-field to the geosphere with those calculated by SKB in SR-PSU for the Global Warming calculation case (CCM_GW).
   b. Modifying the radionuclide transport model by adding the concrete fracture model, which was included in subsequent complementary information provided by SKB (2017), and comparing the impact on the radionuclide fluxes from the near-field with SKB's findings.
   c. Running the model for SKB's Accelerated Concrete Degradation calculation case (CCM_BC) and reporting the impact on the radionuclide fluxes from the near-field.

An additional task was then undertaken to investigate the effect of removing the grout around the bitumen-solidified wastes. This was done by running a new AMBER model in which the 1BMA single compartment model was adapted to contain only bitumen-solidified wastes with no surrounding grout. The radionuclide fluxes from the near-field were compared with the model in (b).
SKB have recently proposed a revised design for the 2BMA vault. SKB's radionuclide transport model for the 2BMA design that was assessed in SR-PSU, has already been reimplemented in the AMBER code (Towler and Penfold, 2017a). This included development of a simplified model that considers a single caisson for

---

[1] http://ecolego.facilia.se/ecolego/show/HomePage

the Global Warming calculation case. The scope of the second task in this assignment is to modify the AMBER single caisson model to reflect the new engineering design. The impact of the new design on the radionuclide fluxes from the near-field is assessed and compared against the results of SKB's calculations.

Approach

There are two tasks in this assignment: reimplementing SKB's models for 1BMA, and reimplementing SKB's models for the new 2BMA design. Towler and Penfold (2017a) showed that a simplified model of a single caisson could produce very similar results to a model of all the caissons in the 2BMA vault. Therefore, models of a single compartment in the 1BMA vault, and a single caisson in the 2BMA vault, are used in this assignment.

Towler and Penfold (2017a) did not reimplement SKB's models for 1BMA, so the 1BMA models presented in this report have been developed during this assignment. The 2BMA single caisson model, developed by Towler and Penfold (2017a), has been updated during this assignment: to include the improved understanding of SKB's approach described by Towler and Penfold (2017b), and additional clarifications recently provided to SSM by SKB. The updated 2BMA single caisson model forms the basis for the second task in this assignment.

Report Structure

This report is structured as follows:
- Section 2 presents the AMBER model of the 1BMA vault.
  - Section 2.1 presents a description of the 1BMA vault.
  - Section 2.2 presents the results for the CCM_GW case with and without the fracture model implemented.
  - Section 2.3 presents the results for the CCL_BC case.
  - Section 2.4 presents the results for bitumen-solidified waste not surrounded by grout.
- Section 3 presents the results for the CCM_GW case for the updated 2BMA vault design.
  - Section 3.1 describes the updated 2BMA single caisson model for the corrected CCM_GW case.
  - Section 3.2 presents the results of a sensitivity analysis where organic complexants are included in the model.
  - Section 3.3 presents the results for the CCM_GW case and SKB's new 2BMA design.
- Section 4 presents the conclusions from this further review assignment.

2 Single-Caisson Model of the 1BMA Vault

2.1 Description of the Vault

2.1.1 Layout

The 1BMA vault is the existing vault for intermediate-level waste in SFR. Unlike the 2BMA vault in which waste is stored in caissons separated by backfill, the 1BMA vault is a single concrete structure with waste stored in adjacent sections separated by concrete walls (Figure 2-1).
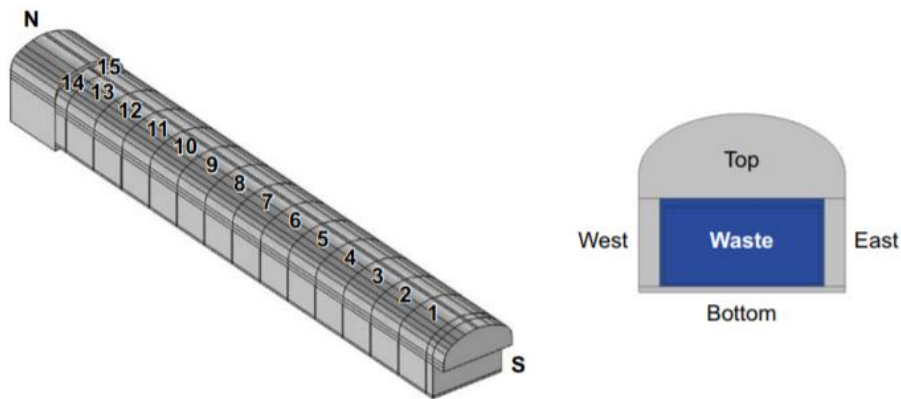
Figure 2-1. Layout of the 1BMA vault (left) and a cross-section of the vault (right). Image reproduced from SKB, 2014b (TR-14-09).

Within each section of the concrete structure, the wastes are embedded in grout. The 1BMA vault will be backfilled, around the concrete structure, with Macadam.

2.1.2 Wastes

The 1BMA vault contains the following waste types:

- Concrete-embedded wastes in concrete moulds (CM_E)
- Cement-solidified wastes in concrete moulds (CM_CS)
- Concrete-embedded wastes in steel moulds (SM_E)
- Cement-solidified wastes in steel moulds (SM_CS)
- Bitumen-solidified wastes in steel moulds (SM_BS)
- Concrete-embedded wastes in steel drums (SD_E)
- Bitumen-solidified wastes in steel drums (SD_BS)

The numbers of waste packages associated with each waste stream is described in Appendix A of SKB, 2014a (TR-14-02). These have been categorised into the waste types above, as summarised in Table 2-1.

Table 2-1. Waste streams in 1BMA.

Waste Stream	Packages in 1BMA	Model Waste Type
B.05/B.05:9	3360	SD_BS
B.05:2	224[1]	
B.23	33	SM_E
C.01:9	7	CM_CS
C.01:9-30	61	
C.23	63	CM_E
F.05:1	1454	SD_BS
F.05:2	258	
F.15	11	SM_CS
F.17/F.17:1	1187	SM_BS
F.17cellulose	195	
F.23C	57	CM_E
F.23	220	SM_E
F.99:1	2	SM_BS
O.01:9	397	CM_CS
O.01:9-30	278	
O.23/O.23:9	509	CM_E
R.01/R.01:9	1689	CM_CS
R.10	121	CM_CS
R.15	186	SM_CS
R.23C	338	CM_E[2]
R.23	172	SM_E[2]
R.29	188	CM_CS
S.21	488	SD_E
S.23	113	CM_CS

[1] There are actually 892 drums of B.05:2 waste in 1BMA but these are represented as 224 'units' to normalise the inventory in each drum (TR-14-02).

[2] SKB docID 1601415 classifies R.23 and R.23C as cement-solidified rather than concrete-embedded, which contradicts TR-14-02.

The total resulting number of packages of each type is given in Table 2-2. In Table 2-2, waste streams have been assigned to different waste types using the mapping in SKB docID 1601415.

Table 2-2. Number of packages of each waste type in 1BMA at 2075 AD.

Waste Type	Number
Concrete-embedded waste in steel moulds	253
Concrete-embedded waste in concrete moulds	629
Concrete-embedded waste in steel drums	488
Cement-solidified waste in steel moulds	369
Cement-solidified waste in concrete moulds	3192
Bitumen-solidified waste in steel moulds	1384
Bitumen-solidified waste in steel drums	5964

SKB (2013: R-13-37) details the radionuclide inventories per package for each waste stream. This data was combined with the data in Table 2-1 and Table 2-2 to calculate the radionuclide inventories for each model waste type (Table 2-3).

The inventories in Table 2-3 have been verified by comparing them with the total inventories in Appendix A of TR-14-09. There are small discrepancies in the total

inventories of many radionuclides. The only significant difference is for Mo-93, for which the inventory calculated from R-13-37 and the given number of packages is just over half of the inventory given in TR-14-09. For the 1BMA AMBER models, we used the inventories calculated from R-13-37 and so the AMBER models may give lower fluxes for Mo-93 than SKB's models (by a factor of ~2).

Table 2-3. Initial inventories in 1BMA.

	SM_E	CM_E	SD_E	SM_CS	CM_CS	SM_BS	SD_BS
Ag-108m	6.00E+08	9.59E+08	5.27E+05	8.95E+08	9.00E+09	5.57E+09	2.12E+09
C-14-inorg	0.00E+00	0.00E+00	0.00E+00	3.13E+10	4.25E+11	1.42E+12	1.78E+10
C-14-org	0.00E+00	0.00E+00	0.00E+00	8.14E+09	1.12E+11	2.65E+10	4.28E+08
Cl-36	6.68E+06	1.08E+07	5.81E+03	1.33E+07	1.47E+08	4.39E+07	1.04E+08
Cs-135	1.44E+06	1.10E+07	9.17E+04	5.29E+07	6.88E+08	8.67E+07	6.92E+05
I-129	3.53E+05	3.26E+06	2.75E+04	8.48E+06	9.72E+07	3.62E+07	6.53E+05
Mo-93	1.37E+07	6.49E+07	9.61E+03	1.85E+07	4.29E+08	1.76E+08	7.78E+07
Nb-93m	1.02E+09	1.34E+09	6.59E+05	1.18E+09	3.80E+09	9.01E+09	7.89E+08
Ni-59	8.02E+10	1.02E+11	9.71E+06	1.84E+11	1.58E+12	9.85E+10	4.06E+10
Pu-240	5.93E+07	9.01E+07	4.63E+07	3.01E+08	3.01E+09	3.22E+08	3.75E+07
Ra-228	0.00E+00	0.00E+00	0.00E+00	0.00E+00	0.00E+00	0.00E+00	0.00E+00
Se-79	4.84E+05	3.50E+06	3.67E+04	1.11E+07	1.26E+08	5.54E+07	1.07E+07
Tc-99	8.70E+07	3.60E+08	9.47E+05	3.55E+08	4.11E+09	1.12E+09	1.63E+08
Th-228	0.00E+00	0.00E+00	0.00E+00	0.00E+00	0.00E+00	0.00E+00	0.00E+00
Th-232	0.00E+00	0.00E+00	0.00E+00	0.00E+00	0.00E+00	0.00E+00	0.00E+00
U-236	2.97E+04	4.57E+04	2.76E+04	1.56E+05	1.69E+06	1.66E+05	4.48E+05
Zr-93	0.00E+00	1.80E+07	9.71E+03	1.66E+07	1.73E+08	1.02E+08	4.09E+07

2.1.3 Material Properties

The material properties of the concrete walls, Macadam backfill and grout are the same as those used in the 2BMA model (Towler and Penfold, 2017a).

There has been further clarification from SKB regarding the properties of the concrete-embedded and cement-solidified waste types (SKB docID 1601415). These waste types are given a fractional cement content of 1 and 'effective' densities that reflect their cement content. They use the K_d values of cement. These properties are summarised in Table 2-4.

Table 2-4. Properties of cement-based waste forms in 1BMA.

Property	Time (years AD)	Cement-solidified waste	Concrete-embedded waste
Porosity (-)	2000-102,000	0.33	0.34
Effective density (kg/m^3)	2000-102,000	560	75
Effective diffusivity (m^2/s)	2000-2100	3.0×10^{-10}	3.0×10^{-10}
	2100-2500	3.5×10^{-10}	3.5×10^{-10}
	2500-3000	5.0×10^{-10}	5.0×10^{-10}
	3000-102,000	1.0×10^{-9}	1.0×10^{-9}

There were no bitumen-solidified wastes in 2BMA, so material properties for bitumen have been found for 1BMA. SKB (docID 1601415) assumed that there is no retardation in the bitumen-solidified wastes, so they are assigned an effective diffusivity of 2×10^{-9} m^2 s^{-1} and K_d of 0 m^3 kg^{-1}, with a density of 1030 kg m^{-3} (Table 6-1 in TR-14-10). No information is given on the porosity of the bitumen-solidified wastes, so these are assumed to have a porosity of 1, to be consistent with the effective diffusivity, which is for free water.

K_d reduction factors have been used to account for the presence of organic complexants, taken from Table 7-11a in TR-14-10.

2.2 Global Warming Calculation Case (CCM_GW)

2.2.1 Model Implementation

A near-field single concrete compartment model of the 1BMA vault was implemented in AMBER. The approach mirrors that used by Towler and Penfold (2017a) to build a simplified single caisson model for the 2BMA vault.

The waste is discretised using the same approach as the ECOLEGO model, as clarified in SKB's presentation to SSM on 28 October 2016 (Åstrand, 2016). The concrete-embedded and cement-solidified wastes are represented with two compartments each; an 'inner' and 'outer' compartment (see Figure 2-2). Where wastes are disposed in concrete moulds, the moulds are represented using a single compartment. Bitumen-solidified wastes are also represented with a single compartment.
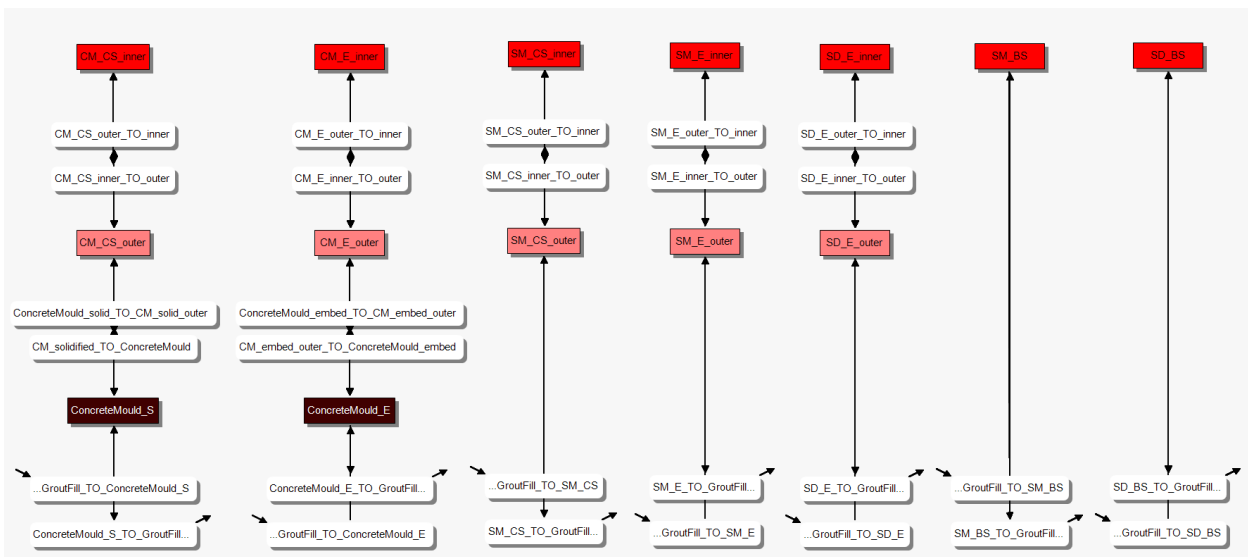
Figure 2-2. Compartment configuration to represent that waste types in the 1BMA single concrete compartment model. (Waste and mould compartments are coloured. Transfers between compartments are white).

There has been further clarification from SKB on the compartment lengths and areas used in the model to calculate diffusion. These have been taken from Tables 9, 10 and 12 in docID 1601415 and used in the AMBER model.

The grout inside the concrete structure, that surrounds the waste packages, is represented by a single compartment. The six concrete walls are then represented individually. Each wall is represented by five compartments (Figure 2-3). So, there is a total of 30 concrete wall compartments in the AMBER model.

SKB have modelled flows through the 1BMA vault in 6 directions; North, South, East, West, up and down. The flows were taken from spreadsheets provided by SSM (2018), and the average (arithmetic mean) flow through caissons 1-13 in each direction was calculated to provide a representative flow through the single concrete compartment model[2]. The timings of cement degradation and shoreline displacement for the global warming calculation case (CCM_GW) are as given in Towler and Penfold (2017a). Flows were linearly interpolated between shoreline positions but there are step-changes in flows at different cement degradation stages.

The geosphere is not explicitly modelled since the output of interest is the radionuclide flux from the near-field to the geosphere.
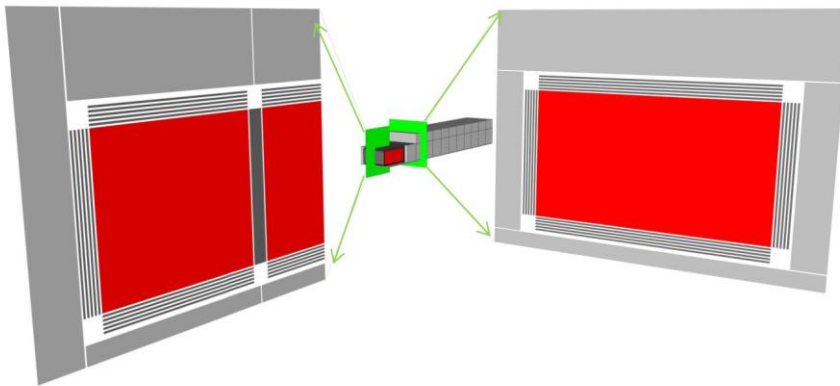
Figure 2-3. SKB's discretisation of a single concrete compartment in the 1BMA vault (Åstrand, 2016).

2.2.2 Fracture Model

The concrete fracture model described in Appendix D of TR-14-09 was originally omitted from SKB's models. This was subsequently corrected following clarifications (SKB, 2017). For comparison, the global warming calculation case (CCM_GW) has been implemented in AMBER both with and without the fracture model.

Once the concrete walls have become severely or completely degraded, radionuclide transport through them is calculated using the fracture flow model. In the Global Warming calculation case, this occurs at 22,000 AD. As interpreted from Appendix

---

[2] Compartments 14 and 15 are smaller than the rest of the compartments so were deemed not to be representative.

D in TR-14-09, in the fracture flow model there is assumed to be no sorption of radionuclides onto the concrete. SKB docID 1601415 suggests that in the fracture model, 10% of the flow is assumed to pass through the bulk concrete so that some sorption continues after 22,000 AD. However, it is unclear how this flow division has been implemented. Therefore, to be consistent with previous 2BMA modelling and the description in TR-14-09, sorption on concrete is entirely switched off in the AMBER model once the concrete is severely / completely degraded.

As discussed in Section 4.1 of Towler and Penfold (2017b), it is unclear whether the fracture model also applies to the concrete moulds. In the AMBER 2BMA model, the radionuclide fluxes from the near-field were not significantly affected by fracturing of the concrete moulds. Therefore, in the 1BMA model, we have taken the same approach as Towler and Penfold(2017a), and the concrete moulds are assumed to fracture at the same time as the concrete walls.

2.2.3 Results

Selected radionuclide fluxes from the near-field to the geosphere calculated by AMBER for the CCM_GW with the concrete fracture model are compared with the corrected results from SKB (2017) in Figure 2-4. The AMBER results from the CCM_GW with and without the concrete fracture model are compared in Figure 2-5.

The radionuclide fluxes calculated by AMBER for radionuclides that are not sorbed, or are only weakly sorbed, (e.g. C-14_org, Ag-108m) are initially slightly higher than the ECOLEGO fluxes. For some radionuclides, e.g. Cs-135, the fraction of the inventory calculated to be released from the near-field before 22,000 AD is larger for AMBER than ECOLEGO. So, post-22,000 AD, the AMBER fluxes decrease significantly more rapidly than the ECOLEGO fluxes.

The peak fluxes are generally higher in AMBER than in the ECOLEGO results, with the exception of Se-79 and Mo-93 (not shown in Figure 2-4). This difference is most significant for Ni-59.

In both the AMBER and ECOLEGO models, there are step changes in the fluxes at 7000 AD and 22,000 AD. These are due to changes in flows through the vault at both times, and degradation, including fracturing, of concrete at 22,000 AD.

The higher fluxes calculated by AMBER may be a consequence of only representing a single concrete compartment in AMBER. Post-3000 y, the dominant flow direction in the waste is along the long axis of the vault, from one compartment into the adjacent compartment. Therefore, in the ECOLEGO model radionuclides can be retarded through sorption onto cementitious materials in the downgradient compartments. This this process is not represented in the AMBER model as it only considers a single compartment.

This effect is not seen in the AMBER model of a single 2BMA caisson, because the caissons in 2BMA are not connected. The caissons are separated by Macadam backfill. Therefore, radionuclides transported out of a caisson will tend to be transported in the backfill rather than into a downgradient caisson.
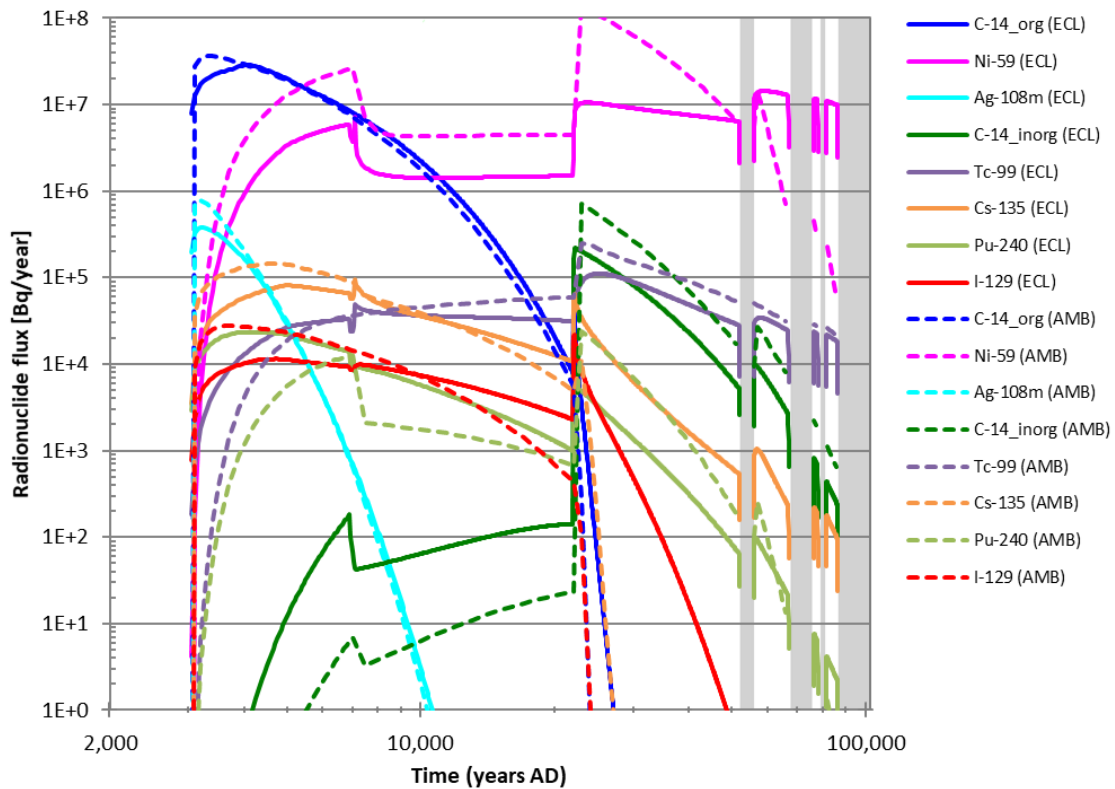
Figure 2-4. Comparison of radionuclide fluxes from the 1BMA vault to the geosphere calculated by AMBER (AMB) for the CCM_GW, compared with the corrected ECOLEGO (ECL) results.

Figure 2-5 shows that for most radionuclides, the fracture model does not make significant difference to the flux from the near-field. The exception is C-14_inorg which has a peak flux almost 70 times higher when the fracture model is included. This is because C-14_inorg has the highest K_d value for cement and therefore experiences the most sorption in intact concrete. Sorption of C-14_inorg is not reduced by organic complexation. When sorption is switched off in the concrete fracture model, this has a significant impact on the C-14_inorg fluxes. Other radionuclides which are usually highly-sorbing (e.g. Pu, Tc) have high sorption reduction factors in the presence of organic complexants, so they experience less sorption and are less affected by the concrete fracture model.

This is unlike the findings from the 2BMA model in which the fracture model made a significant difference to the radionuclide fluxes.
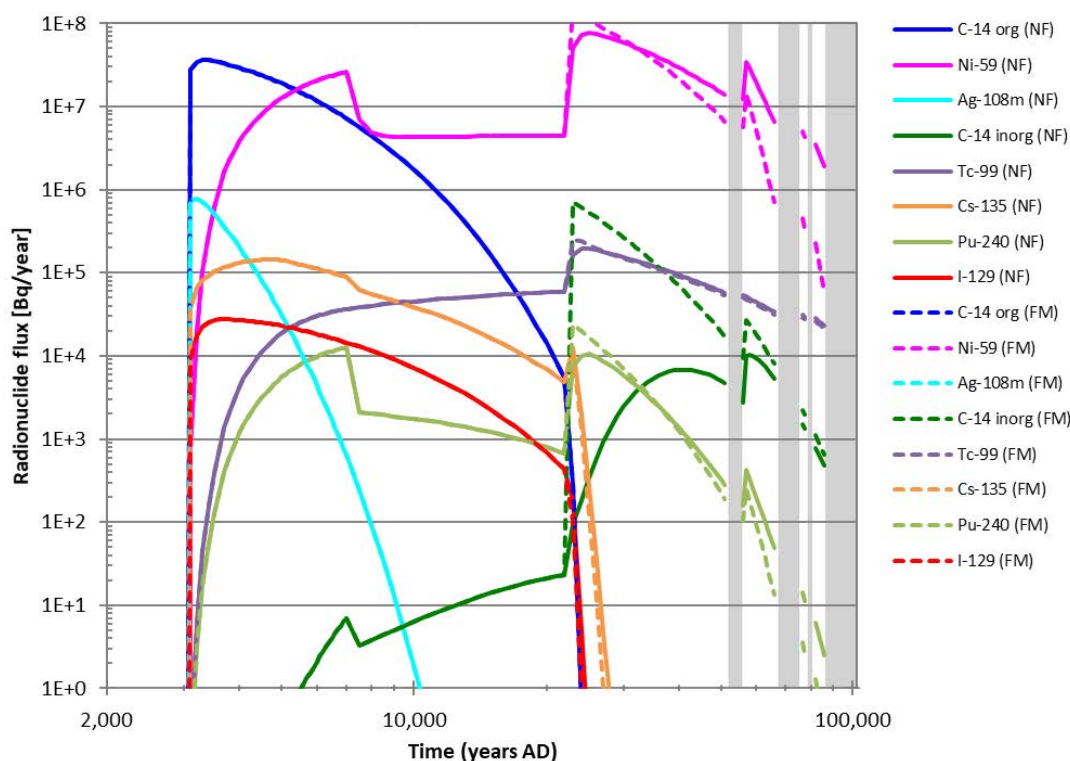
Figure 2-5. Comparison of radionuclide fluxes from the 1BMA vault to the geosphere calculated by AMBER for the CCM_GW without the fracture model (NF) and with the fracture model (FM).

2.2.4 Conclusions

There is a reasonable agreement between the radionuclide fluxes from the near-field for 1BMA calculated by AMBER and ECOLEGO. The fit is good for radionuclides that are not sorbed, or are only weakly sorbed, but becomes worse as sorption increases. The AMBER model generally gives higher peak fluxes, but this may be an artefact of only representing a single concrete compartment.

With the exception of C-14_inorg, the fracture model has very little effect on the 1BMA near-field radionuclide fluxes. This behaviour is different to 2BMA, in which the fracture model has a much more significant effect on the radionuclide fluxes. This may be because of the use of sorption (K_d) reduction factors in the 1BMA model. This reduces the retardation of the most highly-sorbing radionuclides, so there is less impact when sorption is turned off once the concrete has fractured. As discussed later in Section 3.2, these reduction factors do not appear to be used in the 2BMA model and therefore the impact of the sorption being turned off is greater in the 2BMA model.

2.3 Accelerated Concrete Degradation (CCL_BC)

The Accelerated Concrete Degradation calculation case (CCL_BC) is described in Section 4.2.3 of TR-14-09. The case assumes the vault concrete structure physically degrades much more rapidly than in the CCM_GW. This leads to higher flow rates through the concrete structure, and hence the wastes and grout inside the structure, at earlier times compared with the CCM_GW. However, accelerated chemical degradation is not considered, as the CCM_GW is already considered to cautiously overestimate the rate of chemical degradation.

Table 4-7 in TR-14-09 shows that the CCL_BC assumes the concrete to be severely degraded from 3000 AD to 22,000 AD and completely degraded thereafter. In addition, the walls of the concrete structure are assumed to be fractured throughout the assessment timeframe.

The changes made to the AMBER model for the CCM_GW (with the corrected fracture model) to implement the CCL_BC case were:
- flows through the near-field (Table 4-7 in TR-14-09 and spreadsheets provided by SKB (2018));
- effective diffusivities (Table 4-8 in TR-14-09);
- porosities (Table 4-9 in TR-14-09); and
- the nature of the concrete - it is assumed to be fractured at all times (Table 4-7 in TR-14-09).

2.3.1 Results

The effects of accelerated concrete degradation are shown by comparing the results from the AMBER models for CCM_GW and CCL_BC in Figure 2-6. Both models include the concrete fracture model.

In the CCL_BC, there are higher flows through the wastes at early times compared with the CCM_GW. This results in higher peak fluxes of radionuclides that are not sorbed, or are only weakly sorbed, e.g. C-14_org and I-129, and more rapid decrease in the fluxes beyond the peak.

In the CCL_BC, concrete is assumed to be fractured from 3000 AD. The fluxes of radionuclides that sorb onto concrete increase to a greater extent, due to the combined effects of increased flow and reduced sorption. So, radionuclides which have the highest K_d values for cement (such as C-14_inorg) are most affected by accelerated concrete degradation.

Tc-99 is less significantly affected by accelerated concrete degradation than other strongly sorbing radionuclides. This is because Tc-99 sorbs moderately to the Macadam. The Macadam is unaffected by the concrete degradation and therefore, although the Tc-99 reaches the Macadam more quickly in the CCL_BC case, it is retarded in the backfill before being released to the geosphere. This 'buffers' the effect of the quicker release from the concrete structure.
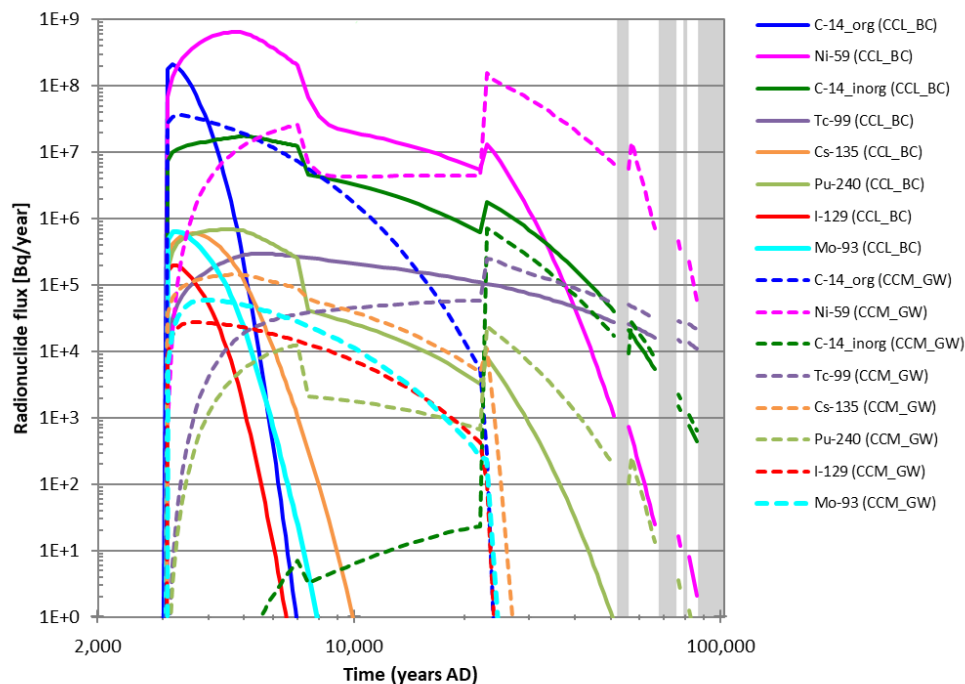
Figure 2-6. Comparison of radionuclide fluxes from the 1BMA vault to the geosphere calculated by AMBER for the Global Warming calculation case (CCM_GW) and Accelerated Concrete Degradation calculation case (CCL_BC).

The ratios of the peak near-field fluxes calculated by AMBER for the CCM_GW and CCL_BC are given in Table 2-5. These show that for all radionuclides, the peak flux from the near-field is increased in the accelerated concrete degradation case. The largest increase in peak flux is for Pu-240, followed by C-14_inorg.

Pu-240 is predominantly found in packages with cement moulds. In the accelerated concrete degradation case, in the AMBER model, the cement moulds are also assumed to fracture from 3000 AD. Therefore, the flux of Pu-240 increases significantly as it does not sorb onto the concrete moulds or the concrete vault structure.

C-14_inorg experiences the largest increase in flux during the first 20,000 years. This is consistent with the high sensitivity of the flux of C-14_inorg to fracturing of the concrete, and loss of sorption, shown previously.

Table 2-5. Comparison of peak radionuclide fluxes from the 1BMA vault to the geosphere calculated by AMBER for the Global Warming calculation case (CCM_GW) and Accelerated Concrete Degradation calculation case (CCL_BC).

Radionuclide	Peak radionuclide flux (Bq/y)		Ratio
	CCM_GW	CCL_BC	
C-14_org	3.65E+07	2.09E+08	5.7
C-14_inorg	7.06E+05	1.77E+07	25.1
Cl-36	6.08E+04	4.39E+05	7.2
Ni-59	1.55E+08	6.43E+08	4.1
Se-79	4.05E+04	7.98E+04	2.0
Mo-93	5.97E+04	6.39E+05	10.7
Nb-93m	1.80E+04	2.49E+04	1.4
Tc-99	2.48E+05	2.97E+05	1.2

17

Ag-108m	7.80E+05	4.73E+06	6.1
I-129	2.74E+04	1.97E+05	7.2
Cs-135	1.44E+05	5.99E+05	4.2
Pu-240	2.38E+04	6.85E+05	28.8
Zr-93	1.77E+04	2.46E+04	1.4

We do not have access to the timeseries 1BMA near-field radionuclide fluxes from SKB's ECOLEGO model of the CCL_BC. However, peak fluxes are reported in Appendix E of TR-14-09. In Table 2-6, SKB's peak fluxes are compared against the peak fluxes calculated by AMBER.

The peak fluxes are generally within a factor of four, with Ni-59, Pu-240 and I-129 exhibiting larger differences. It is noted that the AMBER results include the fracture model. The reasonable match to SKB's ECOLEGO model for C-14_inorg suggests that the fracture model was included in the CCL_BC results presented in Appendix E of TR-14-09.

Table 2-6. Comparison of peak radionuclide fluxes from the 1BMA vault to the geosphere calculated by ECOLEGO and AMBER for the Accelerated Concrete Degradation calculation case (CCL_BC).

Radionuclide	Peak radionuclide flux (Bq/y)		Ratio
	ECOLEGO	AMBER[1]	(AMB/ECL)
C-14 org	7.5E+07	2.09E+08	2.8
C-14_inorg	8.0E+06	1.77E+07	2.2
Cl-36	1.1E+05	4.39E+05	4.0
Ni-59	5.4E+07	6.43E+08	11.9
Se-79	1.7E+05	7.98E+04	0.5
Mo-93	4.6E+05	6.39E+05	1.4
Nb-93m	3.6E+04	2.49E+04	0.7
Tc-99	3.4E+05	2.97E+05	0.9
Ag-108m	2.5E+06	4.73E+06	1.9
I-129	4.3E+04	1.97E+05	4.6
Cs-135	1.8E+05	5.99E+05	3.3
Pu-240	7.9E+04	6.85E+05	8.7
Zr-93	1.8E+04	2.46E+04	1.4

[1]Including the fracture model

2.3.2 Conclusions

The effect of accelerated concrete degradation is to increase the radionuclide fluxes from the near-field at early times. This is because the concrete walls are assumed to be initially fractured and radionuclides therefore experience no sorption onto the concrete. The flows through the concrete structure are also higher. Since the radionuclide inventory is released more quickly, the long-term fluxes decrease more quickly.

The comparison between the CCL_BC results from AMBER and ECOLEGO is limited as we do not have access to the timeseries 1BMA near-field radionuclide fluxes. However, the peak fluxes from the near-field to the geosphere can be compared and the agreement is reasonable for many radionuclides. The peak fluxes

calculated by AMBER are generally higher than calculated by ECOLEGO. As for the CCM_GW, this may be a consequence of only including a single concrete compartment in the AMBER model.

It is notable that the fluxes are within a factor of 2.2 for C-14_inorg. The fluxes of this radionuclide are very sensitive to the fracture model, so this result indicates that that fracture model was included in SKB's CCL_BC results presented in TR-14-09.

2.4 Bitumen-Solidified Waste

In the AMBER and ECOLEGO models described above, the different waste types are assumed to be evenly distributed throughout the 1BMA vault. Within each compartment of the concrete structure, the wastes are embedded in grout.

In reality, it is likely that there will be no grout in compartments where bitumen-solidified waste is stored, to allow space for the wastes to swell. To test the impact of this against the previous modelling assumption that bitumen-solidified waste packages are spread throughout the vault, a new AMBER model was built in which the single concrete compartment contained only bitumen-solidified waste packages and no grout. The model is otherwise identical to the previous Global Warming calculation case. The flows through the vault have not been altered. In reality, the flows are likely to increase in the absence of grout, so the radionuclide fluxes reported from this case may be an underestimate.

The radionuclide fluxes from the near-field calculated using this model can be compared with the equivalent fluxes per package of bitumen-solidified waste from a model where bitumen-solidified waste packages are dispersed throughout the 1BMA, as in the reference assumption. In both models, the concrete fracture model is applied and organic complexants are included.

2.4.1 Inventory

As given in Table 2-2, there are a total of 1384 packages of bitumen-solidified waste in steel moulds and 5964 packages of bitumen-solidified waste in steel drums in the 1BMA vault. To estimate the number of packages that could fit in a single concrete compartment if this was only filled with bitumen-solidified waste, the available compartment volume and package volume must be calculated.

The available concrete compartment volume was calculated assuming that 20% of the total compartment volume is left as void space for the waste to swell into. This is equivalent to the volume of grout in the previous 1BMA Global Warming calculation case. The bitumen-solidified waste packages can therefore occupy 80% of a concrete compartment, or 1063 m^3.

It was decided to divide the total number of packages in the compartment between steel moulds and steel drums containing bitumen-solidified wastes according to the ratio of their total numbers of packages. This facilitates comparison of the radionuclide flux per package with the model in which the bitumen-solidified wastes are distributed throughout the vault.

In the AMBER models presented in Sections 2.2 and 2.3, the waste package volumes have been taken from SKB docID 1601415. This is thought to be consistent with the package volumes used in the ECOLEGO models which the AMBER model results were compared with. According to this reference, the volume of each steel drum and steel mould is 1 m^3. Using this package volume, approximately 1062 bitumen-solidified waste packages can fit in one concrete compartment. Using the package ratio described above, this is equivalent to 200 packages of bitumen-solidified waste in steel moulds and 862 packages of bitumen-solidified waste in steel drums.

However, SKB have issued a correction regarding the volume of three types of waste package (SKB docID 1585177). Rather than 1 m^3, the volume of the steel drums is 0.238 m^3 and the volume of the steel moulds containing cement-solidified or concrete-embedded waste is 1.7 m^3. Here we assume the steel moulds containing bitumen-solidified waste should also have a volume of 1.7 m^3. The steel moulds are assumed to be cubic and the steel drums are assumed to be cylindrical with the same height as the steel moulds (as in Figure 3-2 of SKB, 2014a). Although these volumes were not used in the previous 1BMA AMBER models for consistency with the ECOLEGO results, it may be useful to consider the impact of using the corrected volumes here in a sensitivity case.

With these corrected package dimensions, the grout content is increased from 20% to 40% per concrete compartment. If we assume that the bitumen-solidified waste in steel drums have a volume of 0.238 m^3 per package and the bitumen-solidified waste in steel moulds have a volume of 1.7 m^3 per package, then a total of 292 packages of bitumen-solidified waste in steel moulds and 1259 packages of bitumen-solidified waste in steel drums can fit in one concrete compartment. This assumes that 60% of the interior volume of the concrete compartment is filled with waste packages and 40% is void space.

In each case, the radionuclide inventory can be calculated using the inventory per package as before.

2.4.2 Results

For the results from the bitumen-only case to be meaningful, it was decided to compare the radionuclide flux per package with the Global Warming calculation case in which bitumen-solidified packages are spread throughout the repository, as in the previous AMBER models. To do this, the existing 1BMA model was modified to 'track' radionuclides arising from the bitumen-solidified waste, so that this could be distinguished from radionuclide fluxes arising from the other waste types. This was done by adding new isotopes, such as 'Ni-59_bitumen' and 'Pu-240_bitumen', to represent the radionuclide inventory arising from the bitumen-solidified waste. The bitumen-solidified waste packages contain only '_bitumen' radionuclides and the other waste packages contain only the original radionuclides. These new isotopes otherwise have identical properties to the original radionuclides.

Since diffusion is calculated from the relative concentration of each radionuclide in each compartment, it is possible that there will be too much diffusion of the '_bitumen' radionuclides from the grout into the other waste packages, as these packages have a zero concentration of the '_bitumen' radionuclides. Two bounding

cases were therefore run; one where the diffusion transfers are not amended (so there is likely to be too much diffusion of bitumen-originating radionuclides into other waste packages), and one where diffusion into other waste packages is turned off (so there is likely to be too little diffusion of bitumen-originating radionuclides into other waste packages).

Original Package Volumes

The radionuclides fluxes from the near-field are compared in Figure 2-7. These are calculated using package volumes of 1 m^3 for the steel drums and steel moulds.
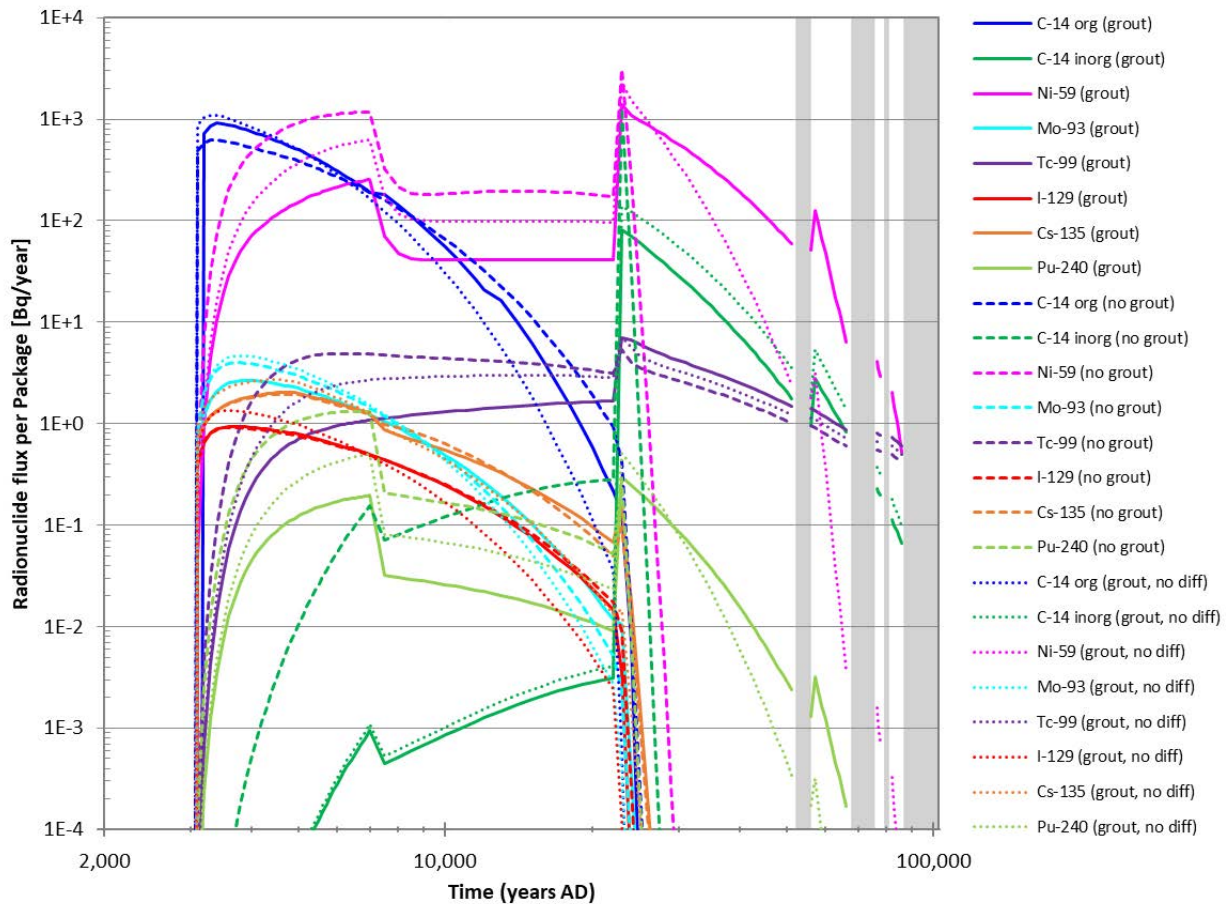
Figure 2-7. Comparison of radionuclide fluxes to the geosphere per package of bitumen-solidified waste calculated by AMBER for three cases: bitumen-solidified waste dispersed through vault with diffusion from grout into other packages (grout); bitumen-solidified waste dispersed through vault with no diffusion from grout into other packages (grout, no diff); and bitumen-solidified waste in one concrete compartment with no grout (no grout).

Turning off diffusion of bitumen-originating radionuclides from the grout to the packages containing non-bituminized waste slightly increases the fluxes from the near-field by a factor of 1 to 1.8. The actual fluxes from the near-field will be somewhere within the range of these two bounding cases. The flux per package for the case where the concrete compartment only contains bituminised wastes and the grout is removed can therefore be compared with this range.

For radionuclides with low cementitious K_d values, there is no significant difference between the cases with and without grout around the bitumen-solidified waste packages. Radionuclides which sorb more strongly to grout (particularly C-14_inorg and Pu-240), experience significantly higher early peak fluxes once the grout is removed. These fluxes then fall faster as the inventory decreases faster.

The peak fluxes per package are compared in Table 2-7. The maximum and minimum ratios between the peak flux with grout and without grout around the bitumen are given; this range comes from the sensitivity case regarding diffusion into the other waste packages.

Most of the radionuclide fluxes are not significantly affected by the removal of the grout and the peak flux ratios are close to a factor of 1. The largest difference in peak flux is for C-14_inorg, followed by Pu-240 and Ni-59. As explained previously, this is because C-14_inorg has the highest K_d for grout (once sorption reduction factors are taken into account), so is therefore most affected by the removal of the grout.

Some radionuclides (C-14_org, Tc-99 and Ag-108m) experience slightly lower peak fluxes in the case where there is no grout around the bitumen-solidified waste packages. In the case of Tc-99, removal of the grout reduces the retardation of Tc-99 so it has an initially higher flux from the near-field. The peak flux occurs when the concrete fractures. This peak is lower in the model with no grout since more of the initial inventory has already been released at the time when fracturing occurs. C-14_org and Ag-108m do not sorb to grout. The reduced fluxes of these two radionuclides occurs because the volume of water around the waste has increased (the void space has a porosity of 1 compared to the grout porosity of 0.3-0.5) but the volumetric flow rate through the vault has not changed, so the advective transfer rate has decreased. This affects all the radionuclides, but for those that sorb to cement, the effect of the removal of the grout outweighs the effect of the increased pore volume.

Table 2-7. Comparison of peak radionuclide fluxes to the geosphere per package of bitumen-solidified waste calculated by AMBER for the case where bitumen-solidified waste packages are surrounded by grout, with or without diffusion into other waste packages (Grout & Grout, No Diff), or surrounded by void space (No Grout). The Min Ratio is No Grout ÷ Grout. The Max Ratio is No Grout ÷ Grout, No Diff (except for Se-79, where Min and Max are reversed).

Radionuclide	Peak radionuclide flux per package (Bq/y)			Ratio	
	Grout	Grout, No Diff	No Grout	Min	Max
C-14_org	9.11E+02	1.10E+03	6.20E+02	0.6	0.7
C-14_inorg	8.13E+01	1.40E+02	1.29E+03	9.2	15.9
Cl-36	3.76E+00	5.41E+00	3.64E+00	0.7	1.0
Ni-59	1.40E+03	2.34E+03	3.09E+03	1.3	2.2
Se-79	1.74E+00	6.46E-01	7.46E-01	0.4	1.2
Mo-93	2.66E+00	4.67E+00	3.97E+00	0.9	1.5
Nb-93m	9.93E-01	1.26E+00	1.50E+00	1.2	1.5
Tc-99	6.95E+00	7.11E+00	5.42E+00	0.8	0.8
Ag-108m	4.29E+01	5.20E+01	2.90E+01	0.6	0.7
I-129	9.40E-01	1.35E+00	9.10E-01	0.7	1.0
Cs-135	2.03E+00	2.71E+00	1.95E+00	0.7	1.0
Pu-240	2.98E-01	5.04E-01	1.32E+00	2.6	4.4
Zr-93	9.79E-01	1.25E+00	1.46E+00	1.2	1.5

Corrected Package Volumes

The three cases were then re-run using the corrected steel drum and steel mould volumes of 0.238 m^3 and 1.7 m^3 respectively. This had a small effect on the radionuclide fluxes to the geosphere.

For the case where the bitumen-solidified waste is not surrounded by grout, the peak radionuclide fluxes per package were little changed when the package volumes were updated. This is because the only difference between the two cases is the relative amount of bitumen and void space. Both have the same assumed transport properties in the AMBER model (i.e. no credit is taken for sorption onto the bitumen-solidified waste, and both are given the diffusivity of water), so the radionuclide fluxes are unaffected.

For the cases where the bitumen-solidified waste is dispersed throughout the vault, the peak radionuclide fluxes are within a factor of 2 when comparing the original and corrected waste package volumes (see Table 2-8). The ratios are similar regardless of whether diffusion into the waste packages is allowed. High-sorbing radionuclides (C-14_inorg, Pu-240 and Ni-59) experience slightly lower peak fluxes when the package volumes are updated. This is because the overall volume of waste decreases and hence the volume of grout increases, onto which these radionuclides will sorb. Non-sorbing radionuclides (C-14_org and Ag-108m) have slightly higher peak fluxes when the package volumes are updated.

Table 2-8. Comparison of peak radionuclide fluxes to the geosphere per package of bitumen-solidified waste calculated by AMBER for the case where bitumen-solidified waste packages are surrounded by grout, using the original or corrected package volumes. Diffusion of bitumen-originating radionuclides into the other waste packages is permitted.

Radionuclide	Peak radionuclide flux per package (Bq/y)		Ratio
	Original Volume	**Corrected Volume**	
C-14 org	9.11E+02	1.11E+03	1.2
C-14_inorg	8.13E+01	4.99E+01	0.6
Cl-36	3.76E+00	3.88E+00	1.0
Ni-59	1.40E+03	1.04E+03	0.7
Se-79	1.74E+00	1.79E+00	1.0
Mo-93	2.66E+00	2.46E+00	0.9
Nb-93m	9.93E-01	8.54E-01	0.9
Tc-99	6.95E+00	6.14E+00	0.9
Ag-108m	4.29E+01	5.27E+01	1.2
I-129	9.40E-01	9.72E-01	1.0
Cs-135	2.03E+00	2.08E+00	1.0
Pu-240	2.98E-01	2.13E-01	0.7
Zr-93	9.79E-01	8.43E-01	0.9

The radionuclide fluxes to the near-field for the three cases using the corrected package volumes are compared in Figure 2-8. The relative peak fluxes are similar to the cases using the original package volumes; C-14_inorg, Pu_240 and Ni-59 experience the largest increases in flux when the grout is removed from around the bitumen-solidified waste packages, whereas most other radionuclides experience a slight decrease.
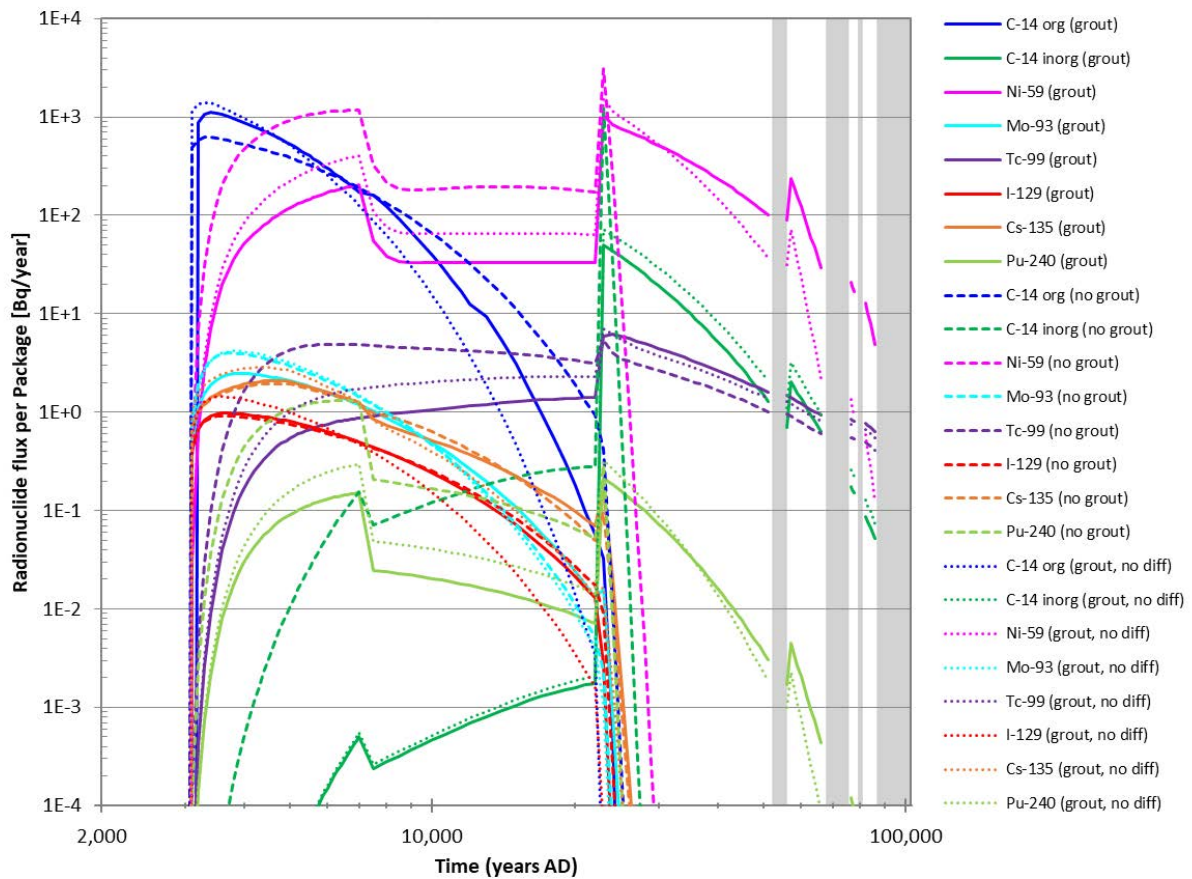
Figure 2-8. Comparison of radionuclide fluxes to the geosphere per package of bitumen-solidified waste calculated by AMBER for three cases: bitumen-solidified waste dispersed through vault with diffusion from grout into other packages (grout); bitumen-solidified waste dispersed through vault with no diffusion from grout into other packages (grout, no diff); and bitumen-solidified waste in one concrete compartment with no grout (no grout).

2.4.3 Conclusions

The effect of removing the grout around the bitumen-solidified waste packages is most significant for radionuclides which sorb strongly to grout (particularly C-14_inorg and Pu-240). These radionuclides are released more quickly from the near-field and the peak radionuclide flux per package to the geosphere is increased up to a factor of 15.9 for C-14_inorg. This effect is likely to be underestimated since the total flow through the vault has not been updated to account for the removal of the grout.

Sensitivity to waste package volume has also been tested. This has little effect on the flux per package from the compartment with no grout, since the bitumen-solidified waste and surrounding void space have the same transport properties. There is some effect on the reference model due to the overall decrease in package volume and respective increase in grout, but radionuclide fluxes to the near-field remain within a factor of 2. It is unclear whether the corrected volume of steel moulds applies to the bitumen-solidified waste or only the concrete-embedded waste; in the sensitivity to waste package volume case, it has been assumed to apply to both waste types.

3 Updated Single-Caisson Model of 2BMA Vault with New Design

3.1 Single-Caisson Model of 2BMA for the Global Warming Calculation Case (CCM_GW)

3.1.1 Description

The basis for this model is the single-caisson model developed during the main review phase for the global warming calculation case (Towler and Penfold, 2017a). Two further updates have subsequently been made to the model based on further information from SKB:

- Updated representation of the waste packages, in which the Tetramoulds were added to AMBER as a new package type.
- Updated waste properties.

The updated representation of the waste packages was described and tested in Section 4.5 of Towler and Penfold (2017b). The updated waste properties are taken from new information supplied in SKB docID 1601415 regarding the material properties of the cement-based waste forms, as used in the 1BMA AMBER model (see Section 2.1.3).

All of the 2BMA single-caisson models described in this report include the concrete fracture model.

3.1.2 Results

The radionuclide fluxes from the near-field for each AMBER model are compared against the ECOLEGO results in Figure 3-1 to Figure 3-4.

Comparing Figure 3-1 and Figure 3-2 shows that the single-caisson model gives very similar results to the full model. Updating the representation of the waste types makes little difference to the results (Figure 3-3).
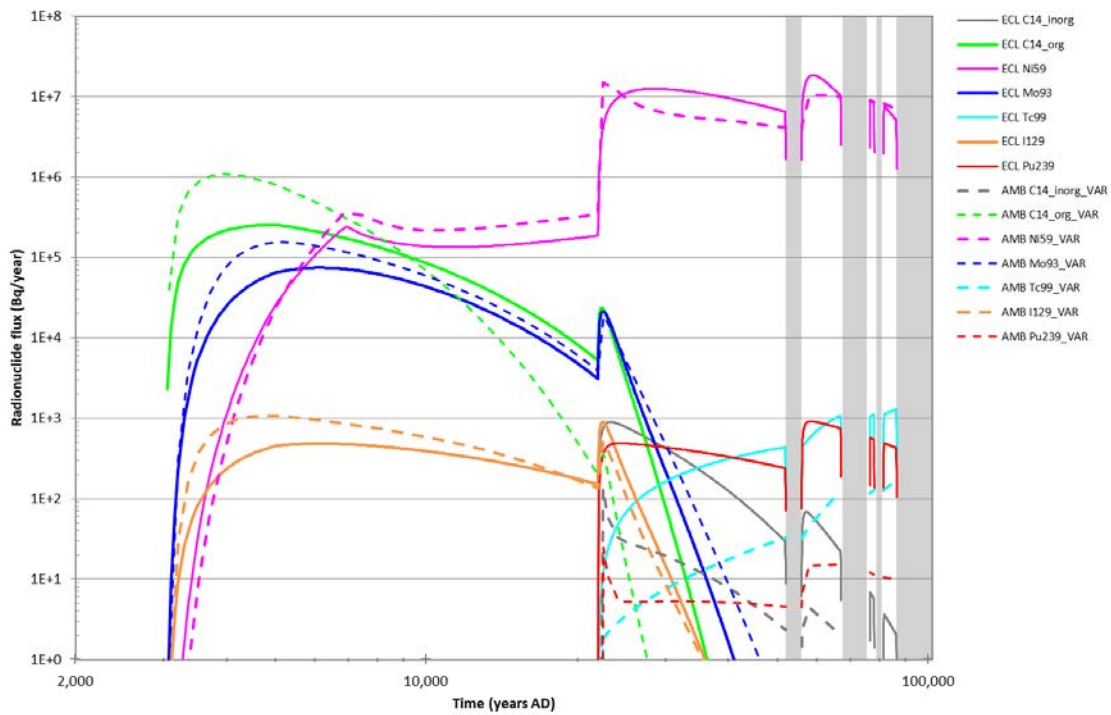
Figure 3-1. Comparison of radionuclide fluxes from the 2BMA vault to the geosphere calculated by the full 2BMA AMBER model (Towler and Penfold, 2017a) for the Global Warming calculation case (CCM_GW), compared against the corrected ECOLEGO model.
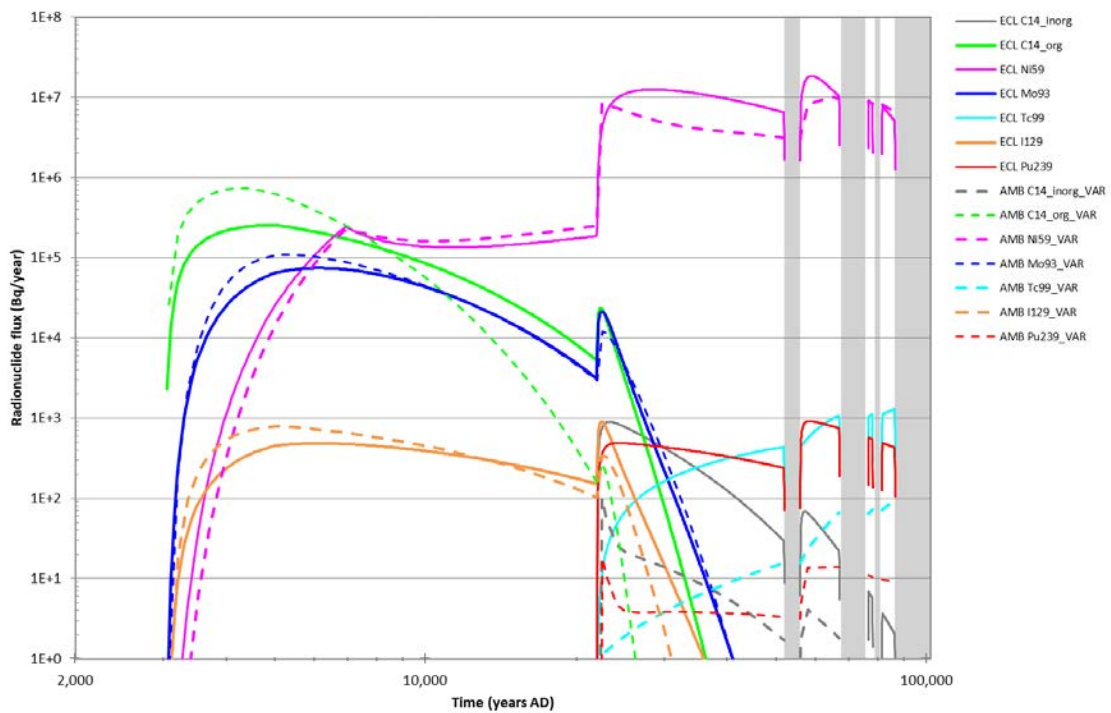
Figure 3-2. Comparison of radionuclide fluxes from the 2BMA vault to the geosphere calculated by the AMBER single-caisson model (Towler and Penfold, 2017a) for the Global Warming calculation case (CCM_GW), compared against the corrected ECOLEGO model.
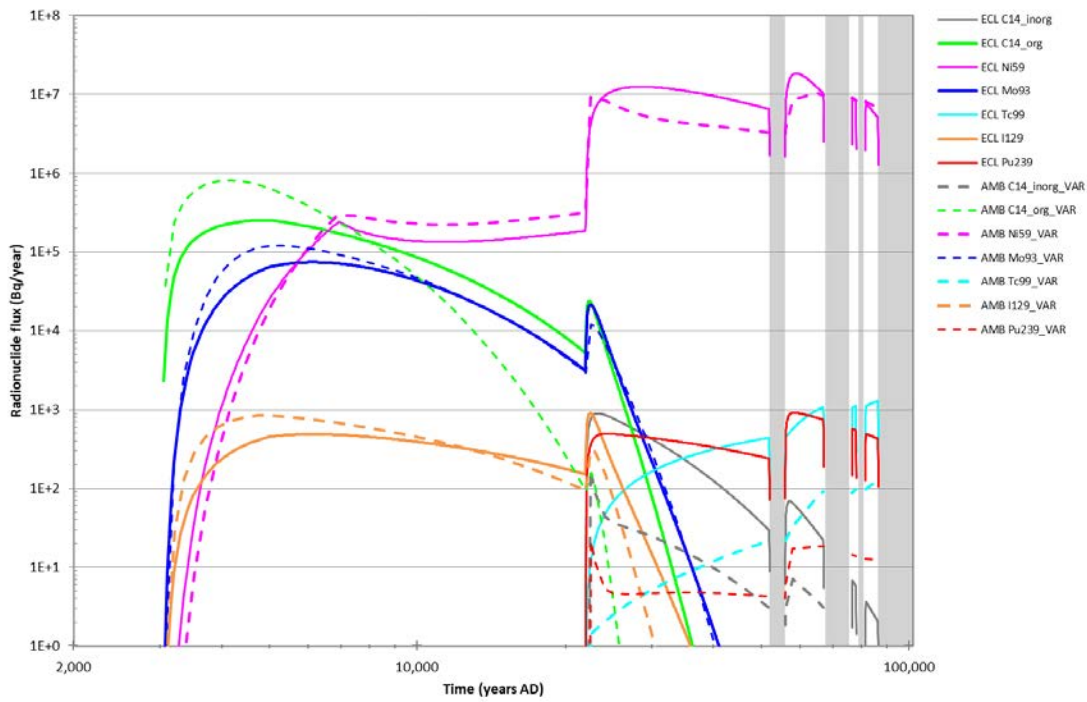
Figure 3-3. Comparison of radionuclide fluxes from the 2BMA vault to the geosphere calculated by the AMBER single-caisson model with updated representation of the waste types (Towler and Penfold, 2017b) for the Global Warming calculation case (CCM_GW), compared against the corrected ECOLEGO model.
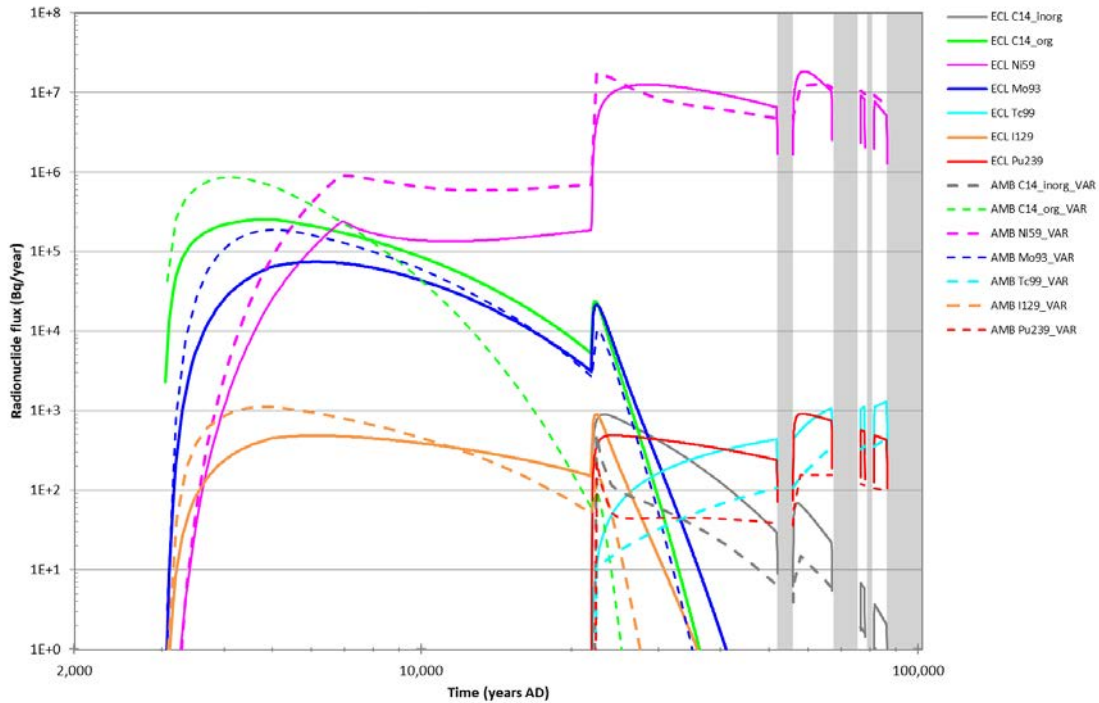
Figure 3-4. Comparison of radionuclide fluxes from the 2BMA vault to the geosphere calculated by the AMBER single-caisson model with updated representation of the waste types and waste properties for the Global Warming calculation case (CCM_GW), compared against the corrected ECOLEGO model.

Updating the waste properties has a bigger effect on the results (Figure 3-4). The fluxes have generally increased. The fluxes are now a worst match against ECOLEGO before 22,0000 AD but a better match against ECOLEGO after this time. Highly-sorbing radionuclides with peak fluxes after 22,000 AD are therefore a better match against ECOLEGO (such as C-14_inorg and Pu-239) whilst other radionuclides are a worse match (such as Ni-59).

3.1.3 Conclusions

The updated representation of the waste types in the AMBER single-caisson model matches the configuration of ECOLEGO. The correction to the representation of the waste packages may be important for the new design, as the new design alters flows through the caisson and hence the packages. The updated waste properties match those described by SKB (docID 1601415) and improve the match between ECOLEGO and AMBER for highly-sorbing radionuclides, although the comparison for non-sorbing and weakly-sorbing radionuclides is similar or worse.

It was decided to use the 2BMA single-caisson model with both updates as the base model for the rest of the 2BMA calculation cases, to be consistent with the waste representation and properties used in the 1BMA model, and with SKB's ECOLEGO model.

3.2 Organic Complexants Sensitivity Analysis

3.2.1 Description

As noted in Section 2.1.3, the 1BMA model in AMBER uses sorption (K_d) reduction factors to account for the presence of organic complexants. This reduces the sorption of some key radionuclides (e.g. Pu, Tc, Zr) by up to a factor of 100. The K_d reduction factors were not used in the previous 2BMA AMBER models described in Section 3.1.1 and Towler and Penfold (2017a,b).

It is not clear from the documentation whether SKB have applied these K_d reduction factors in the CCM_GW calculation case for 1BMA and/or 2BMA, or only in an alternative 'high concentration of complexing agents' calculation case. In TR-14-09 Section 4.1.1 (Global warming calculation case CCM_GW), it is stated, "*Due to the presence of complexing agents, the K_d values were reduced with sorption reduction factors for the radionuclides affected*". However, in TR-14-10 Section 7.11 (Data recommended for use in SR-PSU modelling), it is stated, "*The recommended sorption reduction factors given in Table 7-11a to Table 7-11c. These factors together with the concentrations of complexing agents anticipated in SFR (Keith Roach et al., 2014) are recommended to be used in the high concentration of complexing agents scenario*".

A sensitivity analysis has therefore been carried out to investigate the impact of including organic complexants in the 2BMA model. The K_d reduction factors given

in Table 7-11a in TR-14-10 were added to the AMBER 2BMA single caisson model.

3.2.2 Results

The radionuclide fluxes from the near-field are compared in Figure 3-5 for the AMBER models with and without organic complexants, and the ECOLEGO 2BMA model. Only radionuclides with Kd reduction factors > 1 are shown; for the remaining radionuclides, the two AMBER models give identical results.
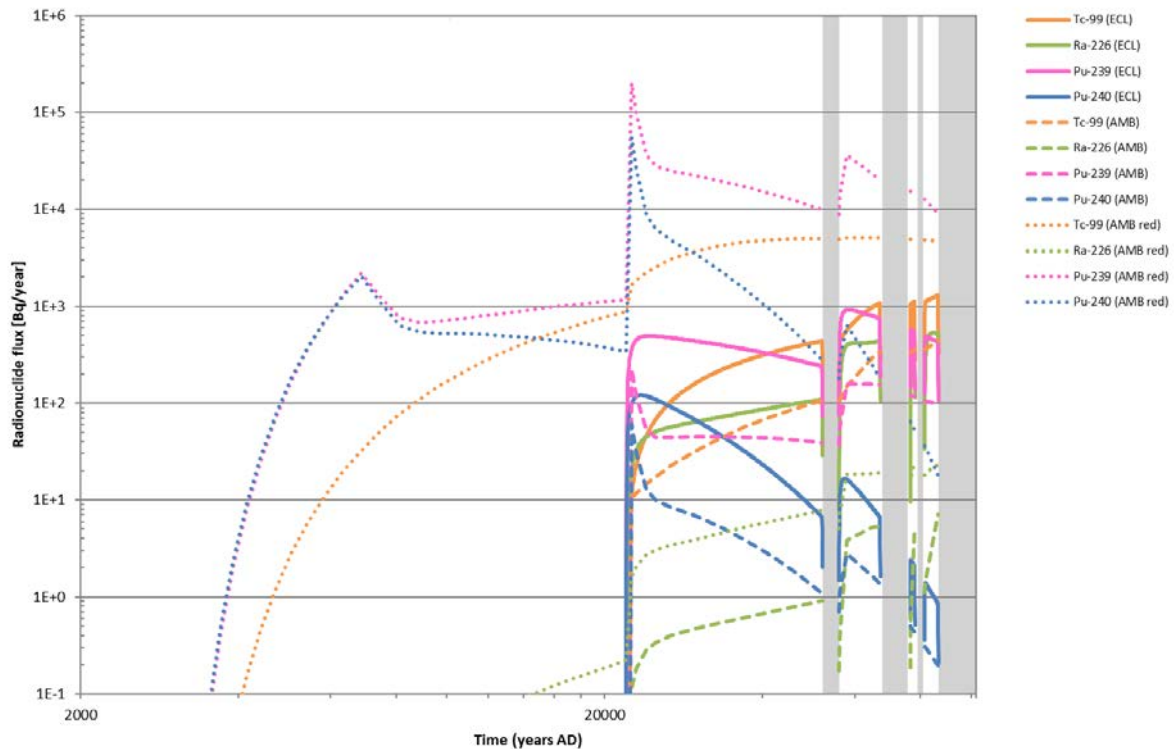
Figure 3-5. Comparison of radionuclide fluxes from the 2BMA vault into the geosphere calculated by the AMBER (AMB) models without and with Kd reduction factors (red), and the ECOLEGO model (ECL).

The radionuclides shown in Figure 3-5 are all highly sorbing. For the AMBER model without organic complexants, the radionuclide fluxes from the near-field are lower than those calculated by the ECOLEGO model by an approximate factor of 10. Introducing Kd reduction factors to the AMBER model to account for the presence of organic complexants causes the near-field fluxes to increase by approximately 2-3 orders of magnitude for the radionuclides shown. This is because the transfer rates are inversely proportional to retardation, so reducing the sorption increases the transfer rates from the waste and also increases the amounts of contaminants in compartments outside the waste. These effects are multiplicative so the transfer flux from the near-field increases by more than the decrease in sorption. The near-field fluxes in the case with sorption reduction factors are around two orders of magnitude higher than the EGOLEGO results (with the exception of Ra-226, which is an order of magnitude lower than the ECOLEGO results).

3.2.3 Conclusions

The radionuclide fluxes from the near-field in the existing 2BMA AMBER model are lower than the ECOLEGO results for highly-sorbing radionuclides. However, applying K_d reduction factors to the AMBER model to account for the presence of complexants increases the fluxes disproportionately, leading to a worse fit with the ECOLEGO results. This suggests that SKB have not used the K_d reduction factors in their CCM_GW case for 2BMA. Therefore, K_d reduction factors have not been included in the AMBER model for the updated 2BMA design.

As shown previously, it appears that the K_d reduction factors have been used in the 1BMA model. The SR-PSU documentation does not clearly explain where K_d reduction factors have been used in SKB's models, where they have not been used, and why. We note Section 4.1 in Keith-Roach et al. (2014: R-14-03) states, "*SKB will limit disposals of cellulose in future waste packages (SKB 2014b) to minimise the potential impact of ISA in 2BMA*." This may explain why organic complexation, and consequent sorption reduction, has been considered in the CCM_GW for 1BMA but not 2BMA.

3.3 Updated 2BMA Design

3.3.1 Description of the Updated Design

The conceptual design of 2BMA has been updated in response to assessment of the mechanical loads that may be applied to the vault throughout its lifetime. There are three main differences between the updated 2BMA design and the design which was previously implemented in AMBER (as described in Section 3.1.1 and Towler and Penfold 2017a pp.6-29):

- Inner walls have been introduced. There is now no need to backfill the space between the waste packages and the walls with grout; instead, this space is left empty to allow space for the waste to swell.
- The dimensions of the outer concrete walls, cap and floor have been adjusted to handle expected loads (i.e. their thickness has been increased).
- Gas relief ducts/channels have been introduced along the concrete walls, filled with a more permeable medium to allow gas to escape.

In SKB's updated ECOLEGO model, they conservatively ignored the new inner walls and changes to the dimensions of the vault and instead only investigated the effect of introducing the gas relief channels / ducts. The updated AMBER model therefore takes the same approach.

The gas relief channels are aligned along one concrete wall; either perpendicular to or parallel to the vault (Figure 3-6). Advection and diffusion are modelled through the gas relief channels.
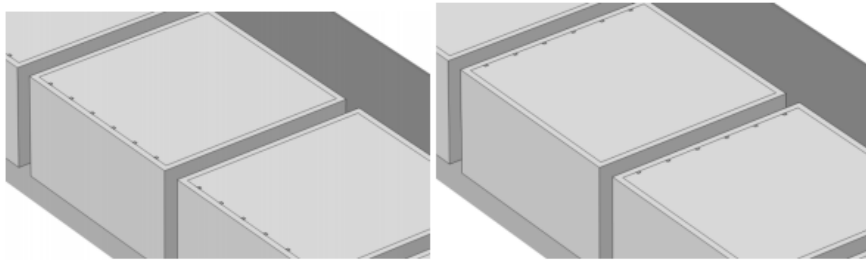
Figure 3-6. Close-up of the geometry of the gas relief channels from SKB's contaminant hydrology model (reproduced from SKB docID 1569813). In one case, the series of gas relief channels has been placed parallel to the length of the vault (left) and in another case perpendicular to the length of the vault (right).

The channels are assumed to be filled with porous mortar, although a variant case has been tested in which the channels are filled with sand and have an even higher porosity and permeability. There are therefore four variant cases to be tested (shown in Table 3-1).

Table 3-1. Summary of calculation cases for updated 2BMA design. 'Channel orientation' refers to orientation of gas channels relative to the long axis of the vault.

Calculation Case	Channel Material	Channel Orientation
B1	Mortar	Parallel
B2	Mortar	Perpendicular
S1	Sand	Parallel
S2	Sand	Perpendicular

The material properties of the mortar and sand are given in SKB docID 1569813. The mortar is assumed to have the material properties of grout (including sorption). Sorption is neglected for the gas discharge channels filled with sand.

In the case of gas relief channels filled with mortar (cases B1 and B2), there is no significant change in flows compared with the previous design. In the case of gas relief channels filled with sand (cases S1 and S2), there is an increase in flow through the caissons for the first 20,000 years. These flows are given in Table 4-6 of SKB docID 1569813.

It is unclear how the flows through the waste have been divided between the gas relief channels and the concrete walls. We have assumed that, for the mortar-filled gas channels, flow through the concrete walls dominates, but for cases S1 and S2, flow is all through the highly permeable sand-filled gas channels. An alternative possibility is that only the 'additional' flow in cases S1 and S2 is transported through the gas channels (with the remainder flowing through the concrete walls). However, this does not seem to be consistent with SKB's results which show a significant difference in radionuclide fluxes between the sand and mortar cases. The difference cannot be entirely accounted for if only a small proportion of the flow travels through the gas relief channels. After the concrete walls fracture, flow is assumed to travel predominantly through the fractured walls.

3.3.2 Results

The AMBER model results show that the new design increases radionuclide fluxes from the near-field to the geosphere. The magnitude of the increase is small for radionuclides that do not sorb onto cement, but larger for radionuclides that sorb strongly onto cement. The main cause of the increased fluxes is removal of the grout fill around the waste packages, inside the caisson. So, there is no grout for radionuclides to sorb onto.

The radionuclide fluxes from the near-field for the four calculation cases are compared with the ECOLEGO results in Figure 3-7 to Figure 3-10. The comparative behaviour of the four cases is similar in AMBER and ECOLEGO, but the fluxes calculated by AMBER are greater than calculated by ECOLEGO.

In both the ECOLEGO and AMBER results, the fluxes from cases B1 and B2 are identical. This is because gas-relief channels filled with mortar are assumed not to affect the flows, and the orientation of the channels therefore makes no difference to radionuclide release.

The radionuclide fluxes are higher in the sand-filled cases (S1 and S2) than the mortar-filled cases. This is due to the increased flows and reduced sorption.

Beyond 22,000 AD, the fluxes from the near-field are identical in all four cases (for both the AMBER and ECOLEGO models). The flows in all cases are the same, and this result suggests that the radionuclides are predominantly travelling through the fractured concrete walls (hence there is no difference between mortar and sand filled channels, which have different sorption and material properties).
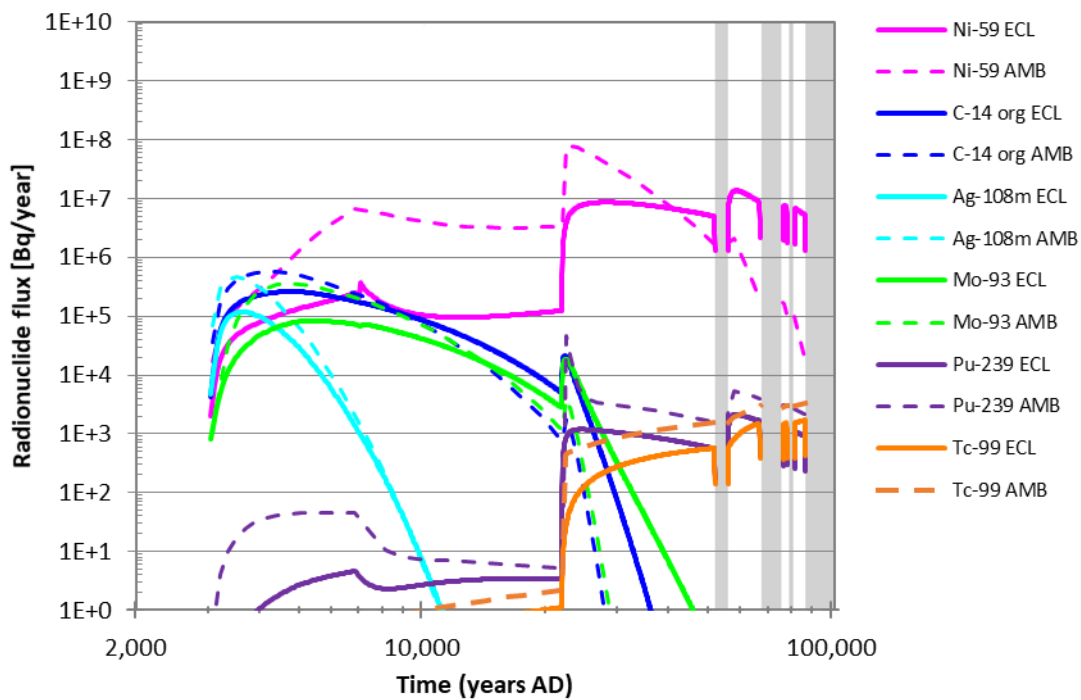
Figure 3-7. Comparison of radionuclide fluxes from the 2BMA vault into the geosphere calculated by the AMBER (AMB) and ECOLEGO model (ECL) for case B1 (gas channels filled with mortar, parallel to the vault).
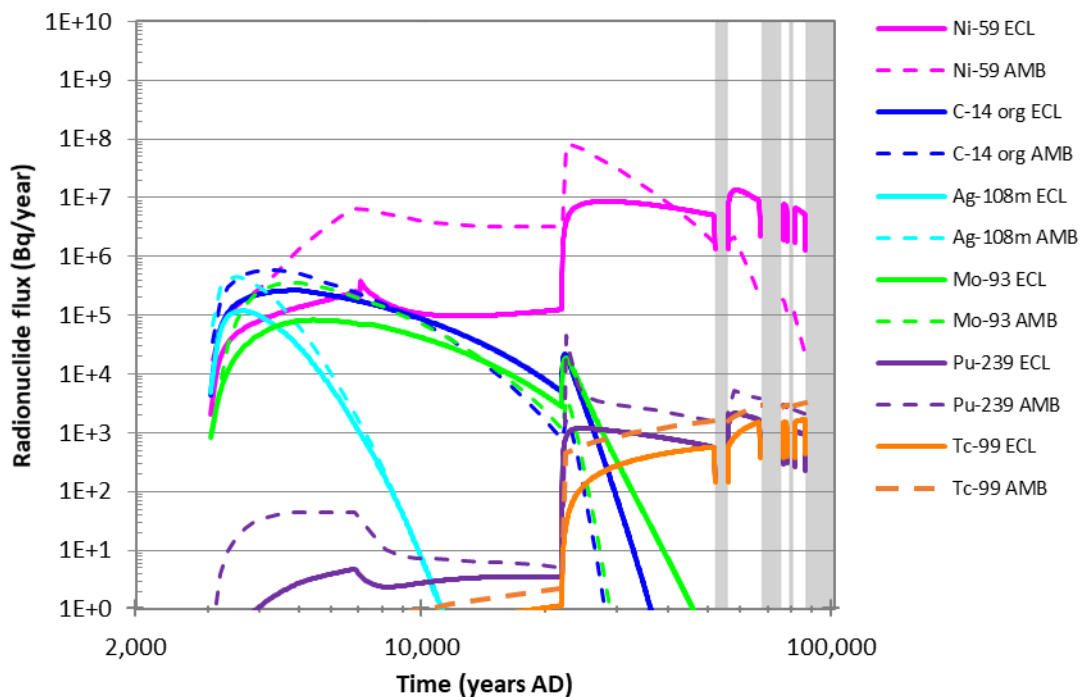
Figure 3-8. Comparison of radionuclide fluxes from the 2BMA vault into the geosphere calculated by the AMBER (AMB) and ECOLEGO model (ECL) for case B2 (gas channels filled with mortar, perpendicular to the vault).
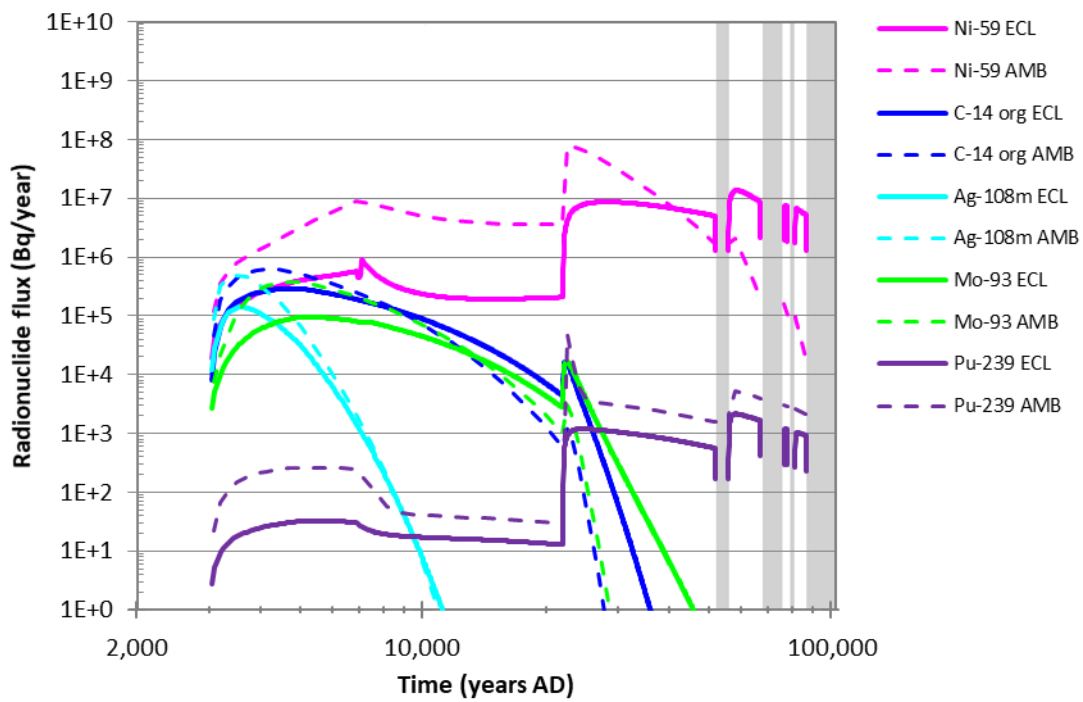
Figure 3-9. Comparison of radionuclide fluxes from the 2BMA vault into the geosphere calculated by the AMBER (AMB) and ECOLEGO model (ECL) for case S1 (gas channels filled with sand, parallel to the vault).
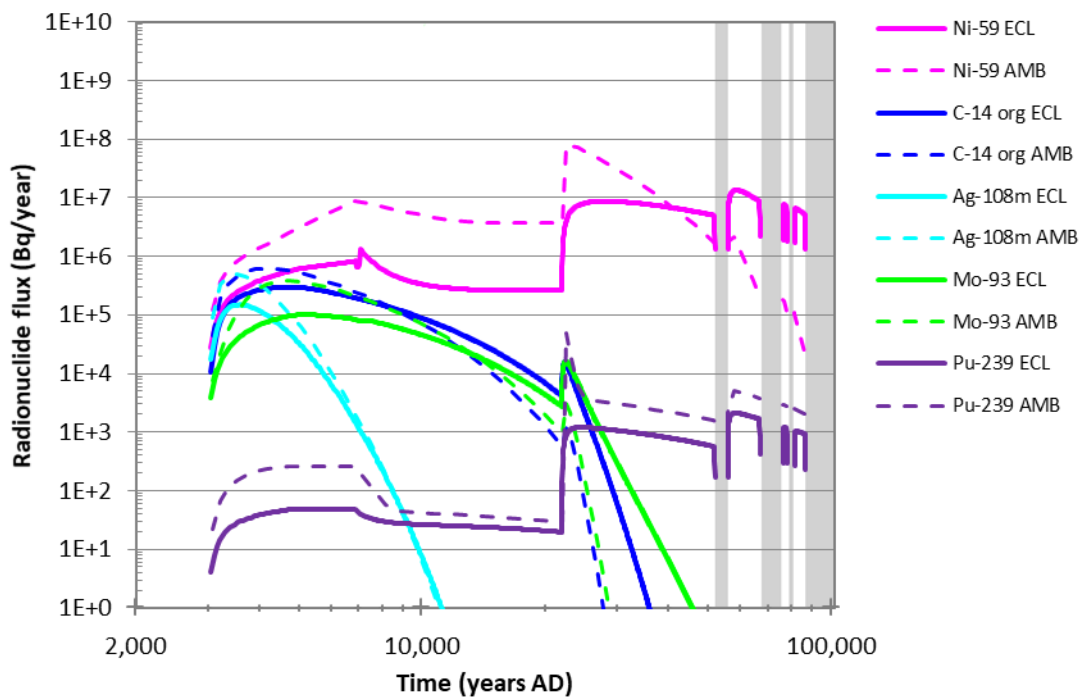
Figure 3-10. Comparison of radionuclide fluxes from the 2BMA vault into the geosphere calculated by the AMBER (AMB) and ECOLEGO model (ECL) for case S2 (gas channels filled with sand, perpendicular to the vault).

There are higher radionuclide fluxes in S2 than S1, because flows through the waste are higher in S2 than S1. In the ECOLEGO results, this effect is noticeable for the Ni-59 and Pu-239 fluxes (highlighted in Figure 3-11), but the difference is very small in the AMBER results and is not visible in Figure 3-11.
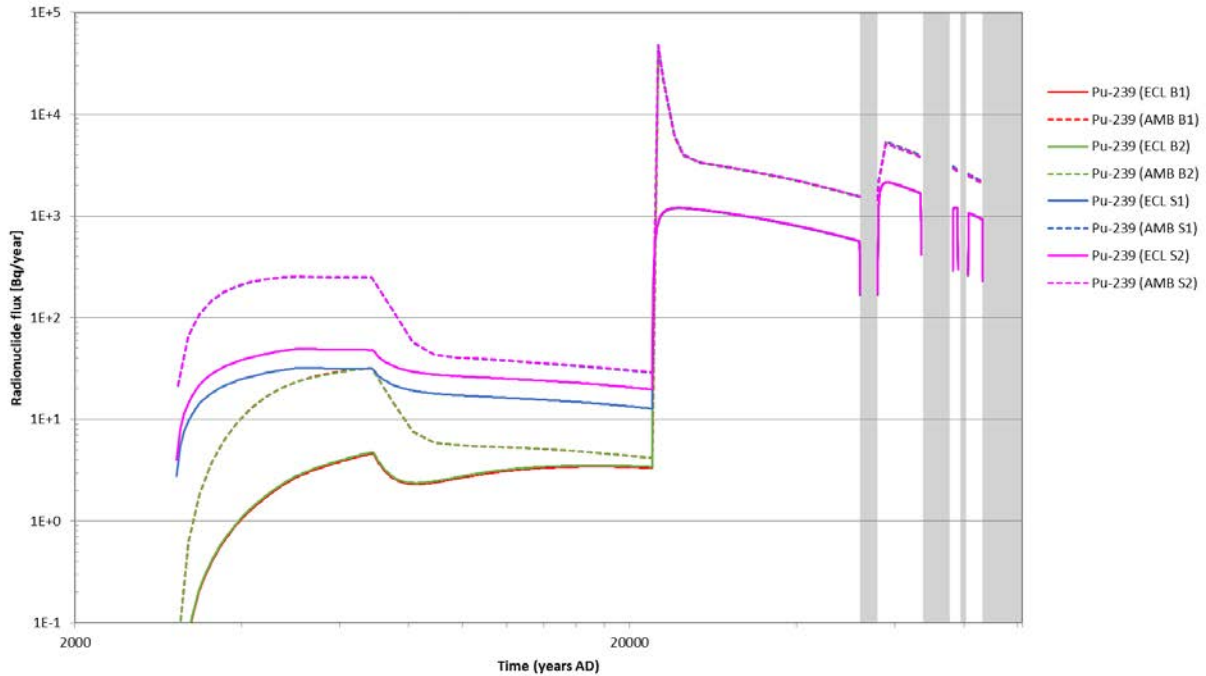
Figure 3-11. Comparison of Pu-239 fluxes from the 2BMA vault into the geosphere calculated by the AMBER (AMB) and ECOLEGO model (ECL) for the variant cases.

3.3.3 Conclusions

SKB's assessment shows that the new design for 2BMA has little impact on the radionuclide fluxes from the near-field to the geosphere. Therefore, the calculated doses are little changed compared with SR-PSU. We found that the new design results in increased radionuclide fluxes from the near-field to the geosphere. The magnitude of the increase is small for radionuclides that do not sorb onto cement, but larger for radionuclides that sorb strongly onto cement. The main cause of the increased fluxes is removal of the grout fill around the waste packages, inside the caisson. So, there is no grout for radionuclides to sorb onto. It is not clear whether the grout has been removed from SKB's models of the new 2BMA design.

The AMBER and ECOLEGO models show the same relative behaviour between the four variant updated designs of the 2BMA repository. The cases with sand-filled gas channels exhibit higher radionuclide fluxes, particularly when the channels are aligned along the wall perpendicular to the long axis (length) of the vault. This is because the highest flows through the repository are along the length of the vault, so the highest flows will intersect all the channels along this perpendicular wall.

Uncertainty about how SKB have divided flows between the gas relief channels and the concrete walls may also contribute to differences between the AMBER and ECOLEGO models.

Only the effect of the gas relief channels and the removed grout has been examined for the updated 2BMA design. There has been no consideration of the impact of the additional inner walls or the adjusted dimensions of the vault. This is for consistency with SKB's approach, as described in Section 4.2 of document 1569813.

4 Summary of Findings

An AMBER model of a single concrete compartment in the 1BMA vault has been implemented and the radionuclide fluxes from the near-field were compared to SKB's ECOLEGO results for certain key radionuclides. Both models used a concrete fracture model, although there is still some uncertainty about how SKB have implemented this.

There is reasonable agreement between the radionuclide fluxes from the near-field, calculated by AMBER and ECOLEGO, for the 1BMA global warming calculation case (CCM_GW). The fit is good for radionuclides that are not sorbed, or are only weakly sorbed, but becomes worse as sorption increases. The AMBER model generally gives higher peak fluxes, but this may be an artefact of only representing a single concrete compartment.

The AMBER model agrees with SKB's results that the concrete fracture model makes little difference to the near-field fluxes for 1BMA. The only exception was for C-14_inorg, which is highly sorbing. The reason for the low impact of the fracture model may be the use of K_d reduction factors in the 1BMA model, which do not appear to be present in the 2BMA model (see discussion below). The retardation in cementitious components of the 1BMA vault is therefore lower than in the 2BMA vault, for the CCL_GW, so the concrete fracture model has less impact.

An investigation was carried out into the effect of removing grout from around the bitumen-solidified waste packages. For radionuclides with high K_d values in cement, the removal of grout significantly increased the initial and peak radionuclide flux per package. This increase is likely to be an underestimate since the flows through the vault have not been updated to reflect the removal of the grout. Using SKB's corrected package volumes made little change to the fluxes from the bitumen-solidified waste packages.

The 2BMA single caisson model has been updated to include clarified waste representation and waste properties. The AMBER configuration is now closer to the ECOLEGO model configuration. This has improved the results for highly-sorbing radionuclides compared to ECOLEGO, although the near-field fluxes for other radionuclides are a slightly less good fit.

An investigation was carried out into the impact of including complexing agents in the 2BMA model. From comparison with the ECOLEGO near-field radionuclide fluxes, it appears that K_d reduction factors for organic complexants have been applied by SKB for 1BMA but not for 2BMA. SKB's documentation does not clearly describe where the K_d reduction factors have and have not been used.

The updated 2BMA vault design was also investigated in AMBER. SKB have only considered the impact of including gas relief channels in the vault and have conservatively ignored the increased concrete wall thickness and inclusion of inner walls in the new design. This approach was also taken in AMBER.

SKB's assessment shows that the new design for 2BMA has little impact on the radionuclide fluxes from the near-field to the geosphere. Therefore, the calculated doses are little changed compared with SR-PSU. We found that the new design results in increased radionuclide fluxes from the near-field to the geosphere. The

magnitude of the increase is small for radionuclides that do not sorb onto cement, but larger for radionuclides that sorb strongly onto cement. The main cause of the increased fluxes is removal of the grout fill around the waste packages, inside the caisson. So, there is no grout for radionuclides to sorb onto. It is not clear whether the grout has been removed from SKB's models of the new 2BMA design.

The AMBER and ECOLEGO models show the same relative behaviour between the four variant updated designs of the 2BMA repository. The highest fluxes are obtained for the 2BMA vault with sand-filled gas channels aligned perpendicular to the length of the vault.

There is some uncertainty about how SKB have parameterised the flows through the gas relief ducts, and this may also account for some of the differences between the AMBER and ECOLEGO model results.

5 References

Åstrand, P. G. 2016. Implementation of SR-PSU near-field models in Ecolego. SSM2015-756-7.

Quintessa. 2016. AMBER Version 6.1.
https://www.quintessa.org/software/AMBER/index.html

R-13-37: SKB. 2013. Låg-och medelaktivt avfall i SFR: Referensinventarium för avfall 2013. R-13-37.

R-14-03. Keith-Roach, M., Lindgren, M. and Källström, K. 2014. Assessment of complexing agent concentrations in SFR.

TR-14-02: SKB. 2014a. Initial state report for the safety assessment SR-PSU. TR-14-02.

TR:14-09: SKB. 2014b. Radionuclide transport and dose calculations for the safety assessment SR-PSU. TR-14-09.

TR-14-10: SKB. 2014c. Data report for the safety assessment SR-PSU. TR-14-10.

SKB. 2017. Corrected implementation of fracture model used for 1BMA and 2BMA in SR-PSU.

SKBdoc 1601415. Svar till SSM på begäran om komplettering av ansökan om utökad verksamhet vid SFR angående konsekvensanalys. (Response to SSM on request for completion of the application for expanded operations at SFR regarding impact assessment).

SKBdoc 1585177. Corrected waste volumes in radionuclide transport models used in SR-PSU.

SKBdoc 1569813. Vidareutvecklad utformning av förvarsutrymmet 2BMA i utbyggd del av SFR. (Further developed design of the 2BMA disposal space in the expanded part of SFR).

SSM. 2018. Qpar1_BMA1.xlsx, Qpar2_BMA1.xlsx, Qpar2_BMA1.xlsx. Received by email from Shulan Xu dated 25/5/2018.

Towler, G. and Penfold, J. 2017a. SR-PSU Main Review Phase: Radionuclide Transport Modelling. QRS-1735D-ModellingReport_V1.1.

Towler, G. and Penfold, J. 2017b. SR-PSU Main Review Phase: Further review of the importance of the caissons and SKB's modelling approach in connection with the caissons. QRS-1735E-CaissonReport_V1.2.

Authors: Joel E. Geier, Clearwater Hardrock Consulting, Corvallis, USA

Assessment of transport parameters and hydrogeological aspects of future human actions

Abstract

Transport parameters are evaluated and analyses are presented regarding additional hydrogeological questions that are potentially relevant for radionuclide release and migration from a proposed extension of the SFR repository for low- and intermediate-level radioactive waste.

Distributions of far-field transport resistance and advective travel times in the bedrock are estimated based on a simplified representative model approach. Transport resistance in brittle deformation zones (fracture zones) is found to be a significant part of the overall transport resistance. This contrasts with earlier results of modelling for a high-level radioactive waste repository, located much deeper in the bedrock.

More conservative estimates for the probability of the *intrusion wells scenario* are obtained by considering the possibility of future population increases and corresponding demand on groundwater resources, including more and deeper wells. A *surface-water-impoundment scenario* (not considered in the safety case) could potentially increase flowrates through the waste vaults by about a factor of four, while decreasing advective travel times and transport resistance by the same factor. Construction of a 40 m deep rock cavern within half a kilometre of the SFR could lead to similar effects.

A more conservative assessment of the *wells downstream scenario* is recommended. An increase in concentrations by up to a factor of six should be considered to represent enhanced capture by higher pumping rates combined with effects of spatial heterogeneity.

Exploratory calculations, using an analytical solution for advective-dispersive transport in a temporally varying groundwater velocity field, indicate a potential to affect early arrivals. These calculations must be seen as preliminary, as they do not account for matrix diffusion or sorption, which would require more complex numerical modelling to investigate.

Contents

1. Introduction

Since 1987 the Swedish Nuclear Fuel and Waste Management Co. (SKB) has operated an underground repository for low- and intermediate-level radioactive waste, the SFR, at a location near Forsmark, Sweden. On December 2014, the Swedish Radiation Safety Authority (SSM) received an application for a proposed extension of this facility. This report presents results of analyses to assist SSM in integrating results and resolving questions related to hydrogeology, which were identified in previous stages of SSM's review.

The main topics addressed here include:

- Flow related far-field transport parameters (far-field transport resistance and advective travel times in the bedrock);
- Hydrogeological aspects of future human actions;
- Conservatism in the wells downstream of the repository scenario;
- Impact of seasonal groundwater fluctuations on transport.

Analyses of these topics are presented in the following four chapters. Overall conclusions are presented in the final chapter.

2. Flow-related transport parameters

Flow-related far-field transport parameters (performance measures) have been derived by SKB using particle-tracking methods in hydrogeological models (Odén et al., 2014). Key performance measures for consequence calculations include:

- flow-related transport resistances F_r in the bedrock (integrated along the discharge path) and

- advective travel times t_{wr} in the bedrock (from the vaults to the geosphere-biosphere interface).

While these calculations were based on a complex, realistic model of the geology, they were limited in their exploration of variants with respect to the key components of the model, including the DFN model for the hydraulic rock domain (HRD) and properties of the hydraulic conductor domains (HCDs).

In support of prior stages of SSM's review, uncertainties in calculations of flowrates to vaults were scoped by Geier (2017), using a simplified representative model (SRM) approach as described by Geier et al. (2019) in which the groundwater passes through a series of segments (Figure 1):

   I.   Regolith (in the recharge area)
  II.   Deformation zone (in the recharge portion of the flow path)
 III.   Rock mass between the recharge deformation zone and the repository
 IV.   The repository components (vault or group of vaults)
  V.   Rock mass between the repository and the discharging recharge deformation
 VI.   Deformation zone (discharging)
VII.   Regolith (in the discharge area)

Supplementary calculations of flowrates (Geier, 2018) considered less conservative assumptions regarding hydraulic connections through the rock mass in SRM segments III and V, taking into account uncertainty that stems from a reasonable expectation of variability in properties of the discrete-fracture network (DFN) and probabilistic deformation zones (PDZs). Here these calculations are extended to scope plausible ranges of the performance parameters F_r and t_{wr}.
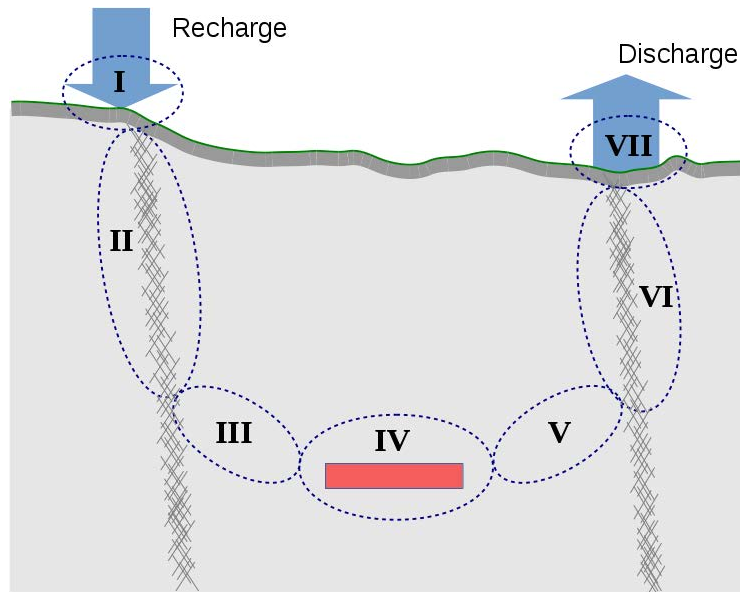
Figure 1: Simplified representative model of a recharge-discharge system for a waste storage facility in fractured crystalline bedrock with a recharge path consisting of (I) regolith in the recharge area, (II) fracture zone with relatively high transmissivity, and (III) sparsely fractured rock mass between (II) and the facility (IV), and a discharge path consisting of (V) sparsely fractured bedrock, (VI) a second fracture zone, and (VII) regolith in the discharge area.

2.1. Analysis

Calculations of performance parameters were performed for a base-case SRM and for several variants with respect to the rock mass segments. For each case, performance parameters were calculated based on the flowrate Q through the vaults, the effective hydraulic conductivity K_{rm} of the rock mass segment belonging to the discharge path, and the hydraulic properties of the discharging fracture zone. Travel time and transport resistance in the discharge-area regolith is neglected, on the grounds that this can be regarded as part of the biosphere, which is handled differently and using more complex models in consequence calculations.

2.1.1. Contribution of discharging rock mass

Advective travel times through the discharge-segment rock mass are calculated based on the following simple assumptions:

1. The flow through the rock mass is dominantly through a small number of pathways (consisting of single fractures or connected fracture networks) acting in parallel;
2. Cases of $N = 1$, 2, or 4 dominant pathways acting in parallel, each with identical properties, are considered

3. Four different models regarding the correlation between fracture transmissivity T and aperture b are considered.

Details are discussed below.

2.1.2. Flow-path complexity and transmissivity in rock mass

Calculation cases are considered within which flow through the rock-mass segment of the discharge path is dominantly via $N = 1$, 2, or 4 pathways in parallel, each with identical transmissivity.

The case $N = 1$ represents flow dominated by a single dominant, high-transmissivity feature. This leads to the highest advective velocities, shortest travel times, and least surface area for water-bedrock interaction, of these three cases.

The cases of $N = 2$ and $N = 4$ pathways are used to illustrate the effects of more distributed flow through the rock mass. In each of these cases, the transmissivity of each pathway is assumed to be identical to that of the other pathways acting in parallel. Although it's unrealistic to expect that parallel pathways will have identical hydraulic properties, this can be viewed as a bounding case, as it results in the lowest advective velocities in the main pathway, and the maximum flux-weighted transport resistance for a given number of pathways.

The transmissivity of each pathway for a given value of N is taken as:

$$T_N = \frac{1}{N}\left(\frac{A_{rm}}{W_{rm}}\right)K_{rm}$$

where W_{rm} is the nominal width of the rock mass (assumed to be on the order of the scale of the SFR vaults) and A_{rm} is the nominal cross-sectional area, as assumed in the previous SRM flowrate calculations. For the results presented here, values of $W_{rm} = 100$ m and $A_{rm} = 50,000$ m^2 were used, so effectively:

$$T_N = \left(\frac{500\ m}{N}\right)K_{rm}$$

The performance parameters are linear with respect to this relationship so the results of alternative values can easily be assessed.

2.1.3. Contributions of discharging deformation zone to performance

Based on experience from complex hydrogeological models where travel times and transport resistance in fracture zones have been taken into account, the contribution of the discharging fracture zone to t_{wr} and F_r is expected to be minor in relation to that of the rock mass. However, simple estimates are produced to scope the potential significance.

For scoping purposes, the discharging fracture zone is considered to be a tabular aquifer with transmissivity T_{DZ}, effective width W_{DZ}, and length in the discharging direction L_{DZ}. These parameters are specified as part of the SRM for flow.

Deformation zones in granitic rock can be expected to have relatively high porosity (so lower ratios of advective velocity to flux) and higher values of wetted surface a_w (so higher transport resistance) because the flow paths are through a relatively intense network of fractures and even breccias.

To represent this, calculations cases are considered within which flow through the deformation segment of the discharge path is dominantly via $N = 4$, 8 or 16 pathways in parallel, each with identical transmissivity, following the same methods as for the rock mass.

2.1.4. Aperture models

Transport-path apertures b_N for a given N are calculated based on specified correlations to transmissivity T_N, depending on the variant considered. Four variants have been considered in the present calculations (b_N expressed in units of m and T_N in units of m^2/s, in all cases):

Cubic law: Theoretical relationship for parallel-plate fractures which can be written as:

$$b_N = \left(12 \frac{\mu_w}{\rho_w g}\right)^{1/3} \cdot T_N^{1/3}$$

where μ_w is the dynamic viscosity of water, ρ_w is the density of water, and g is gravitational acceleration.

"Äspö" model: Empirical model based on data from Äspö, Sweden (Dershowitz et al. 2003):

$$b_N = 0.5 T_N^{0.5}$$

"Hjerne" model: Empirical model of Hjerne et al. (2010):

$$b_N = 0.28 T_N^{0.3}$$

"Stochastic" model: Based on the Äspö model but with a half-order-magnitude standard deviation:

$$b_N = 0.5 \cdot 10^{0.5N(0,1)} T_N^{0.5}$$

The models for transport aperture are compared in Figure 2. Among the deterministic models, the cubic-law case yields the smallest apertures and the Hjerne model yields the largest apertures for the range of transmissivities considered. The stochastic model produces the widest spread of apertures, and can occasional yield values even lower than the cubic law though its expected value for any given value of T conforms to the Äspö model.
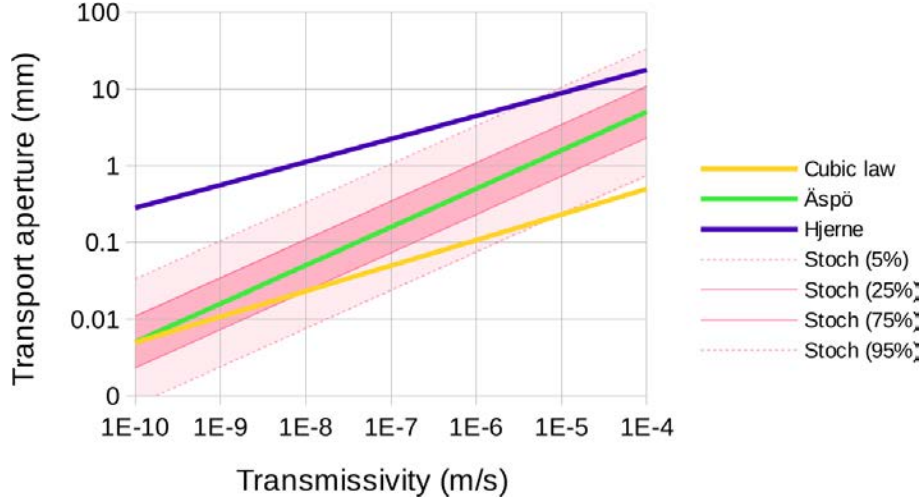
Figure 2: Comparison of the three deterministic models for transport aperture as a function of fracture transmissivity: the cubic law, the "Äspö" empirical model of Dershowitz et al. (2003), and the empirical model of Hjerne et al. (2010). The stochastic model considered in this report follows the Äspö model but with lognormally distributed random variation (represented by the darker pink band showing the 25% to 75% confidence interval and the lighter pink band showing the 5% to 95% confidence interval).

2.1.5. Calculation of performance parameters for the rock mass

The mean advective velocity is equal to the total flowrate through the rock mass divided by the cross-sectional area of the pathways:

$$u_{rm} = \frac{Q}{N b_N W_{rm}}$$

The advective travel time over a distance L_{rm} through the rock mass is then:

$$t_{wr,rm} = \frac{L_{rm}}{u_{rm}}$$

The transport resistance for each of the parallel pathways through the rock mass is:

$$F_{r,rm} = \frac{a_w L_{rm}}{u_{rm}}$$

where a_w is the flow-wetted surface per unit volume of water in the mobile zone (fractures). For a simple planar fracture $a_w = 2/b_N$ so:

$$F_{r,rm} = \frac{2 L_{rm}}{b_N u_{rm}}$$

Substituting in the above expression for u_{rm} yields:

$$F_{r,rm} = \frac{2 N L_{rm} W_{rm}}{Q}$$

From this it can be noted that, under these assumptions, $F_{r,rm}$ is not sensitive to the choice of aperture model for b_N, but only N, the assumed number of flow paths, along with the effective width and length of the rock mass through which discharge occurs.

2.1.6. Calculation of performance parameters for the discharging deformation zone

Performance parameters for the deformation zone portion of the discharge path are calculated analogously to those for the rock mass. The mean advective velocity is equal to the total flowrate divided by the cross-sectional area of the pathways through the deformation zone:

$$u_{DZ} = \frac{Q}{N b_N W_{DZ}}$$

The advective travel time over a distance L_{DZ} through the deformation zone is then:

$$t_{wr,DZ} = \frac{L_{DZ}}{u_{DZ}}$$

The transport resistance is:

$$F_{r,DZ} = \frac{2 N L_{DZ} W_{DZ}}{Q}$$

As for the rock mass, under these assumptions $F_{r,DZ}$ is not sensitive to the choice of aperture model for b_N, but only the assumed number of flow paths, along with the effective width and length of the deformation zone through which discharge occurs.

2.1.7. Flow calculation cases

Three calculation cases were considered with respect to the geosphere components of the SRM model (as labelled in Figure 1):

- Case RM: Segments III and V both considered as having hydraulic conductivity values sampled from effective porous continuum model estimates of the DFN properties.
- Case PDZ-RM: Segment III treated as probabilistic deformation zone (PDZ) with transmissivity T_{PDZ} sampled randomly from the set of all PDZ T values as listed in Table 2.2 of Geier (2017). Segment V treated as for Case RM.
- Case PDZ: Segments III and V are both treated as probabilistic deformation zone (PDZs) and assigned transmissivities T_{PDZ} sampled randomly from the set of all PDZ T values.

Flow calculations for the first case, RM, were reported by Geier (2017). The second case, PDZ-RM, was documented in a project memorandum (Geier, 2018). The third case, PDZ, differs from a more simplistic PDZ case of Geier (2017) which considered only the maximum PDZ T value.

For Segment V in Case PDZ-RM and both segments III & V in Case RM, effective hydraulic conductivity is based on **K** tensor values sampled randomly from geometric upscaling of SKB's DFN model as described in Section 2.6 of Geier (2017). K values based on SKB's "connectivity-analysis" (CA) variant of the DFN model for the SFR area are used; differences with SKB's alternative "tectonic continuum" (TC) DFN variant were determined to be very minor, in the previous analysis.

The case PDZ-RM, which combines a PDZ connection for just one of the rock-mass segments with an ECPM connection for the other segment, was taken as a plausible, conservative alternative, taking into account the possibility that a PDZ with high T, connecting directly between a major fracture zone and the repository, could be overlooked during site characterization and construction. Flow results for Case PDZ-RM are reproduced for reference in Figure 3, as these have previously been presented only in memorandum form (Geier, 2018).

The case PDZ considers the much lower likelihood that two separate PDZs would be overlooked. As implemented here, this is less extremely conservative than the PDZ case considered by Geier (2017), which used the maximum PDZ T values rather than sampling a distribution of values. Results corresponding to the more extreme version of this case can be inferred from the tails of the predicted parameters.

Each calculation case is simulated for 10,000 realizations, sampling values of both T_{PDZ} and rock mass K independently for each realization.
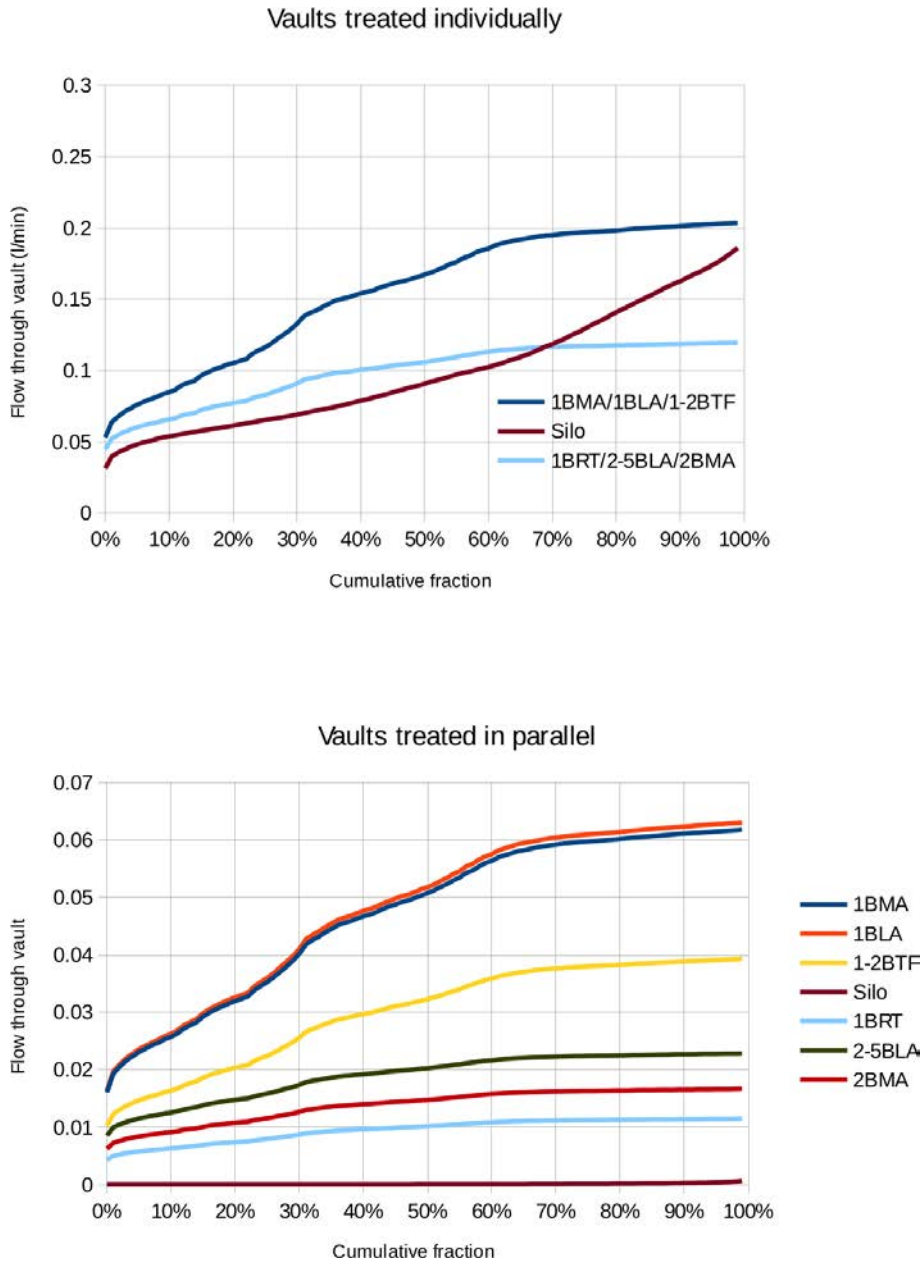
Figure 3: Distributions of flowrates for the simplified representative model with a PDZ connection (with randomly sampled T_{PDZ}) through the rock mass on the recharge path, and ECPM properties for the discharge path, based on 10,000 realizations. The upper plot shows flowrates for the case where each individual vault is considered separately. The lower plot shows flowrates for the case where each of the vaults within each section of the repository are treated as conductors in parallel.

2.2. Results

2.2.1. Advective travel times

Advective travel times t_{wr} as calculated by the SRM for the existing SFR1 (Figure 4) are generally in the range 0.006 yr to 20 yr in the rock mass, and 0.01 yr to 60 yr in the deformation zone portion of the discharge path.

The cubic-law model for aperture as a function of transmissivity produces much shorter advective travel times relative to the Äspö model and the Hjerne model. The latter consistently yields much longer transport times than the cubic-law and the Äspö model. These differences among the three deterministic aperture models are expected based on the quantitative relationships shown in Figure 2.

The stochastic model for aperture yields the widest range of t_{wr} for any of the aperture models. This range is even lower than the cubic law for a small percentage of the realizations, and comparable to the Hjerne model in some cases.

The effects of increasing the number of parallel pathways N by a factor of 2 or 4 are similar for all models. The effect for the ranges of N considered is less significant than the difference between different aperture models. The cubic-law model and the Hjerne model are slightly more sensitive to N than the Äspö model or its stochastic variant, as could be expected due to the different exponent governing the relationship between transmissivity and aperture.

Travel times through the deformation zone part of the discharge path are of comparable magnitude to the travel times through the rock mass, for a given model, but generally higher by a small factor. This results from the combination of effectively higher porosity in the deformation zones (represented by a greater number of parallel pathways for a given transmissivity which leads to a higher total transport aperture) and the longer transport distance for this portion of the discharge path.

The PDZ calculation case, which replaces the rock mass with PDZ connections in both recharge and discharge paths, produces only slightly smaller minimum values of t_{wr} than the minimum values produced by the RM case. The main effect of this case is to produce a longer tail of high t_{wr} values, which result from sampling low values of T_{PDZ}.

The discrete steps in the distribution (Figure 4c) correspond to the finite number of T_{PDZ} values in the sample. These steps are accentuated in the transport times through the DZ part of the model (Figure 4d). This happens because the total flow through the simple representative model in this case is controlled by the PDZ with the lowest value of T_{PDZ}, regardless of whether it occurs in the recharge path or the discharge path. For cases in which the recharge path has a low T_{PDZ}, the transport time in the discharging PDZ can still vary according to its transport aperture, depending on the sampled value of T_{PDZ} for the discharge segment, but the DZ part of the model doesn't vary.

The RM-PDZ case produces results that are intermediate between the RM case and the PDZ case. In this case there is a smoother distribution of travel times for the part of the distribution corresponding to low values of T_{PDZ}, due to the more continuous distribution of RM hydraulic conductivities in the recharge path.
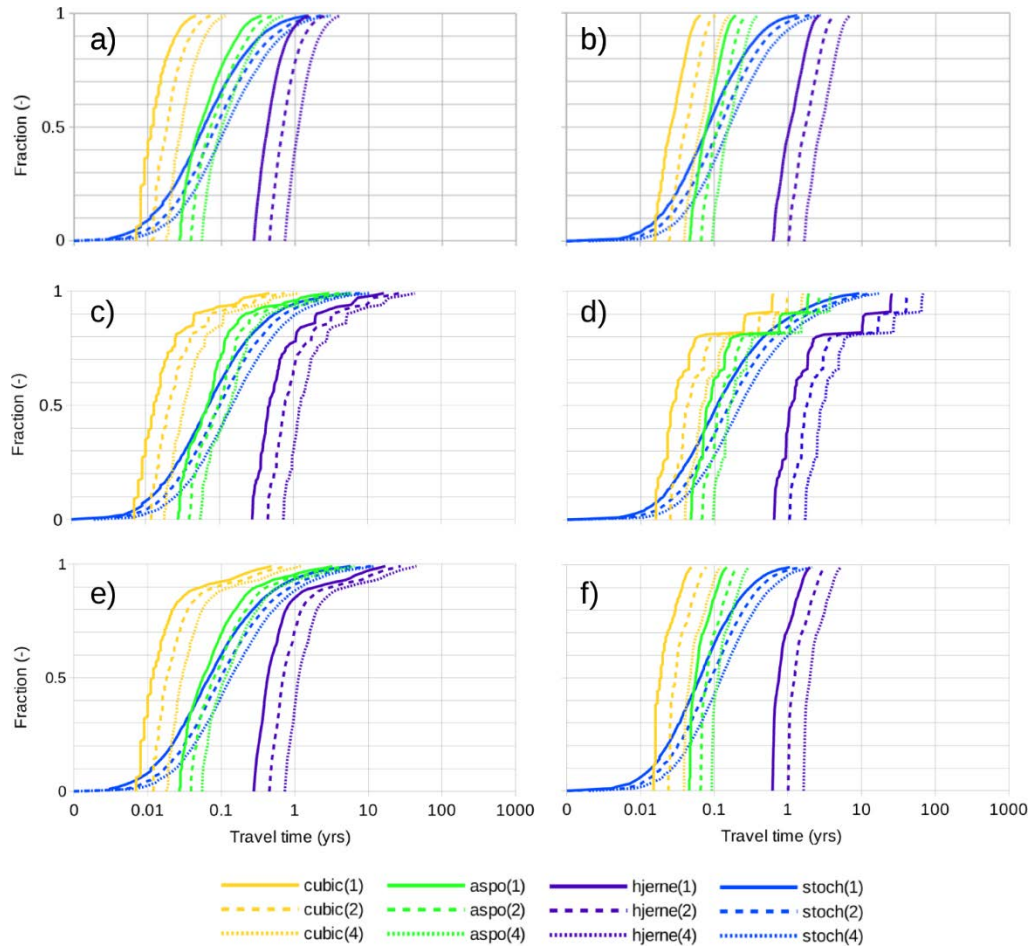
Figure 4: Cumulative distributions of advective travel times in the rock mass (left column, plots a, c, & e) and deformation zone (right column, plots b, d, and f) portions of the discharge path, for SFR1. The top row (a & b) shows results for Case RM, the middle row (c & d) shows results for Case PDZ, and the bottom row (e & f) shows results for Case PDZ-RM. The legend indicates the aperture model (Äspö, Hjerne, cubic-law, or stochastic) with the number of pathways *N* for the rock mass segment in parentheses.

Advective travel times t_{wr} for the proposed extension SFR3 (Figure 5) are qualitatively similar, though slightly higher. The difference is due to the longer transport path through the deformation zone (due to the greater depth) and the correspondingly lower gradients through the rock mass part of the discharge path, for the SFR as compared with SFR1.

Advective travel times t_{wr} as calculated by the SRM for the proposed SFR3 are generally in the range 0.01 yr to 50 years in the rock mass, and 0.015 yr to 80 years in the deformation zone portion of the discharge path.

Advective travel times for the SFR1 and SFR3 are compared in terms of the stochastic aperture model in Figure 6. In general the shift in values between SFR1 and SFR3 is stronger for the deformation-zone segment of the transport path than for the rock-mass segment, regardless of how the rock mass is represented. This can be attributed to the longer transport distances through the deformation zone segments, due to the greater depth of SFR3.
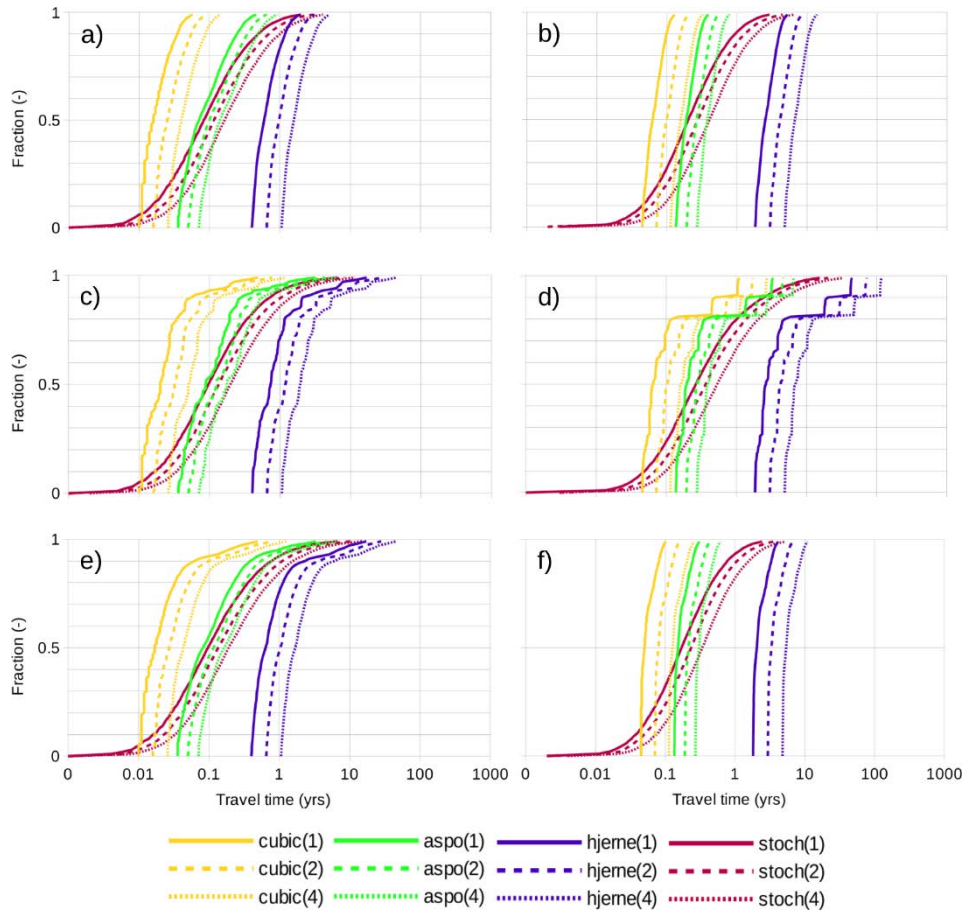
Figure 5: Cumulative distributions of advective travel times in the rock mass (left column, plots a, c, & e) and deformation zone (right column, plots b, d, and f) portions of the discharge path, for SFR3. The top row (a & b) shows results for Case RM, the middle row (c & d) shows results for Case PDZ, and the bottom row (e & f) shows results for Case PDZ-RM. The legend indicates the aperture model (Äspö, Hjerne, cubic-law, or stochastic) with the number of pathways *N* for the rock mass segment in parentheses.

SKB's results as given by Odén et al. (2014), based on more complex models but considering a very limited number of hydrogeological variants, predicted a range of t_{wr} from 0.5 yr to 25 yr for the rock-mass and deformation-zone segments of the discharge path, combined, for SFR1, and from 2.2 yr to 98 yr for SFR3, for the situation in 3000 AD.

SKB's upper-bound estimates for t_{wr} are close in magnitude to the values calculated here. Their lower-bound estimates are significantly higher, by a factor of about 30 for SFR1 and close to 90 for SFR3. This difference is mainly due to the inclusion of more pessimistic relationships between transmissivity and aperture in the present calculations.

If only the present SRM results for the Hjerne model (as used by SKB) are considered, the lower-bound estimates for t_{wr} are very close to SKB's: roughly 1 year for SFR1, and 2 years for SFR3. Thus the main uncertainty in lower-bound estimates of t_{wr} appears to be related to the aperture-transmissivity relationship that SKB has adopted.
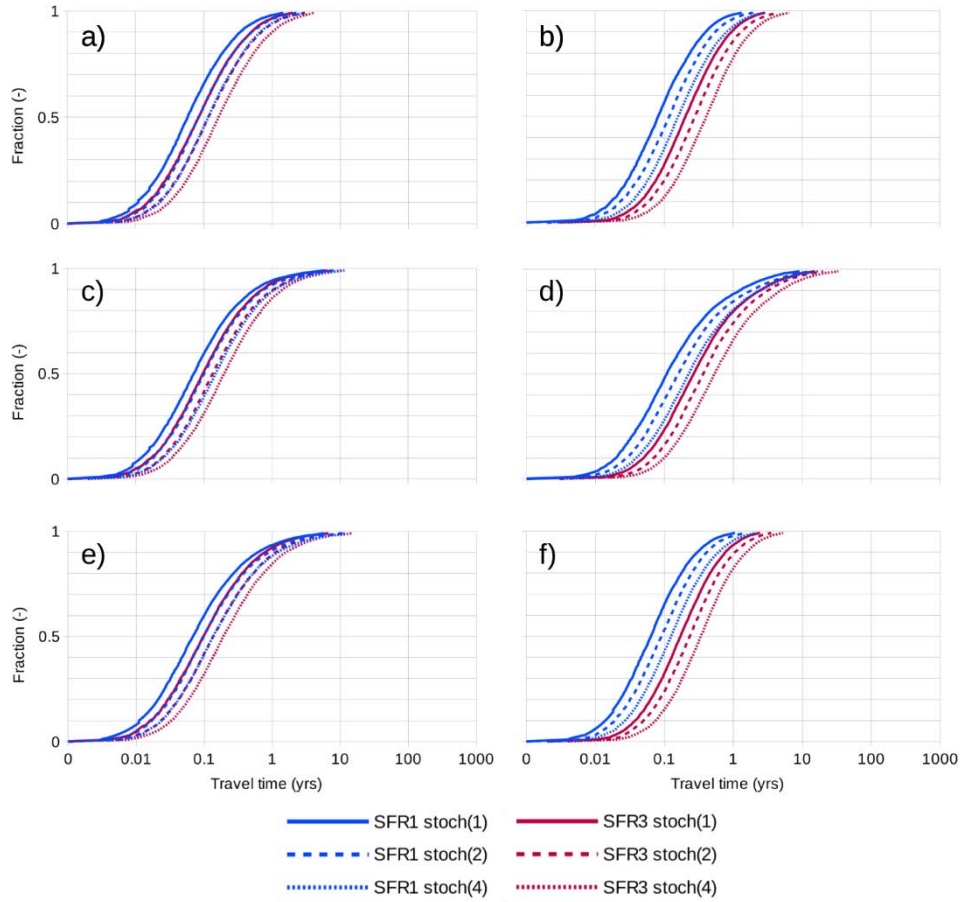
Figure 6: Cumulative distributions of advective travel times in the rock mass (left column, plots a, c, & e) and deformation zone (right column, plots b, d, & f) portions of the discharge path, for SFR1 and SFR3, for the stochastic aperture model. The top row (a & b) shows results for Case RM, the middle row (c & d) shows results for Case PDZ, and the bottom row (e & f) shows results for Case PDZ-RM. The legend indicates the aperture model (Äspö, Hjerne, cubic-law, or stochastic) with the number of pathways *N* for the rock mass segment in parentheses.

The cubic-law model considered as an alternative here is an extreme case, and thus likely unrealistic. However the Äspö model is a realistic alternative that leads to faster travel times. Based on the results for this case, t_{wr} values as low as 0.1 year for SFR1, and as low as 0.2 yr for SFR3, should be considered as reasonably pessimistic lower bounds.

2.2.2. Transport resistances

Distributions of transport resistance F_r are compared for the same set of calculation cases in Figure 7. The different aperture models have no effect on the outcome, as expected based on the mathematical assumptions as mentioned above.

The transport resistance for SFR3 is systematically higher than for SFR1, due to its deeper depth (so longer path through the deformation zones, and correspondingly lower hydraulic gradients through the rock mass).

For the rock mass portion of the discharge path, all three calculation cases (RM, PDZ, and PDZ-RM) produce values as low as 100 y/m for SFR1, when flow is dominated by a single pathway ($N = 1$). Increasing the number of pathways N has a less than linear effect on the transport resistance.

When variable properties of the rock mass are taken into account (Case RM or Case PDZ-RM) higher values can be obtained for a fraction of the realizations. However lower values of F_r are prevented, apparently by the limiting effect of other SRM model segments on flow through the repository.

The transport resistance in the deformation zone is higher than that of the rock mass, by nearly an order of magnitude. Thus deformation zones are predicted to provide the dominant portion of the overall transport resistance, both for SFR1 and SFR3. This is in contrast to the expected results based on prior modelling of high-level radioactive waste repositories, located much deeper in the bedrock. The difference is apparently due to the relatively high hydraulic conductivity of the shallower bedrock, compared with that for the proposed high-level-waste repository at Forsmark.

The overall transport resistance predicted by the SRM is roughly in the range 500 y/m to over 100,000 y/m for SFR1, and 1500 y/m to over 100,000 y/m for SFR3 (the upper bounds are not important for safety assessment calculations). This is lower than SKB's estimates by roughly a factor of 4 for SFR1 and correspondingly for SFR3. Thus the differences are not great and SKB's estimates can be regarded as reasonable. But the present results are recommended as more reasonably cautious estimates for safety assessment calculations.
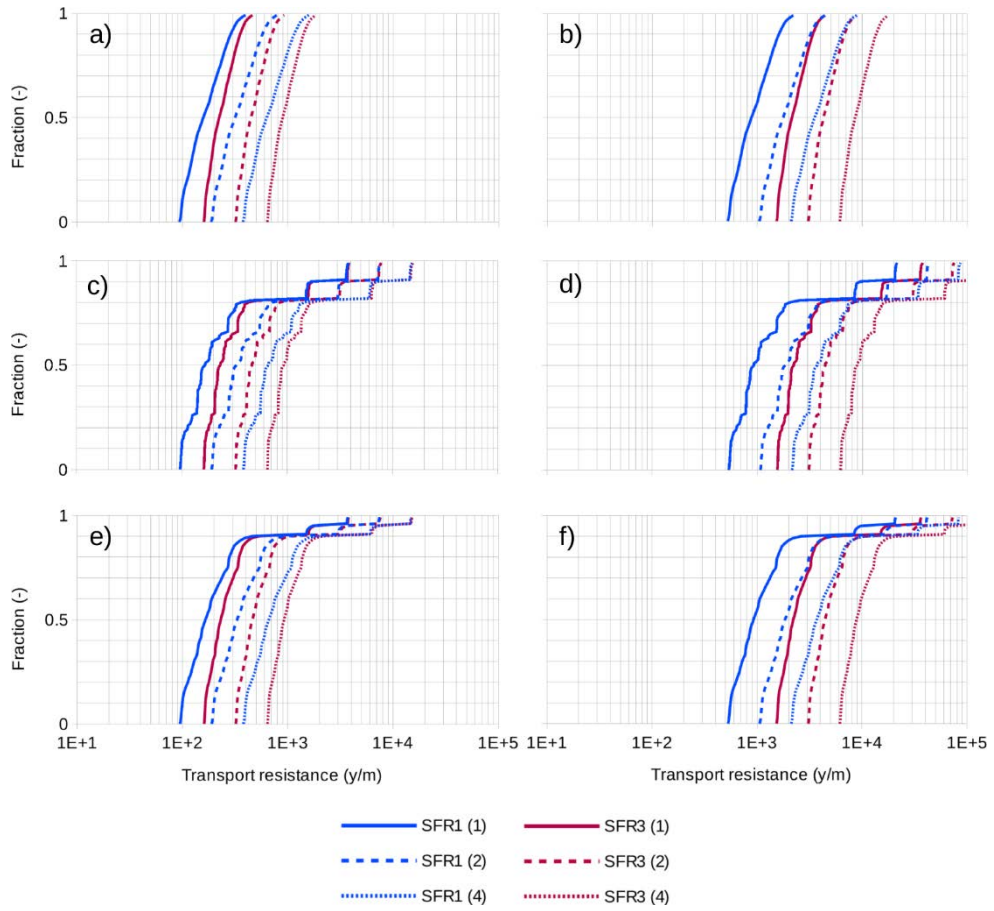
Figure 7: Cumulative distributions of transport resistance F in the rock mass (left column, plots a, c, & e) and deformation zone (right column, plots b, d, & f) portions of the discharge path, for SFR1 and SFR3. . The top row (a & b) shows results for Case RM, the middle row (c & d) shows results for Case PDZ, and the bottom row (e & f) shows results for Case PDZ-RM. The legend indicates the section of the repository (SFR1 or SFR3) and the number of pathways N in parentheses.

3. Hydrogeological aspects of future human actions

Possible future human actions involving water management or underground construction that could affect the groundwater flow system at shallow depths were discussed in the SR-PSU Main Report, mainly qualitatively. This chapter briefly summarizes the previous work by SKB, identifies several potentially significant scenarios for future human actions, and presents simplified quantitative assessments of their potential hydrological consequences.

3.1. Treatment in SR-PSU

Scenarios involving future human actions were discussed in Section 7.7.7 of the SFR-U main report. Actions discussed include:

- Drilling into the repository
- Intrusion wells
- Water management (removal or modifications to the SFR pier),
- Underground construction (tunnel or mine near repository),

SKB's treatment of these issues, and evaluations of the adequacy of this treatment, as assessed in the preliminary phase of SSM's review, are summarized below.

3.1.1. Drilling into the repository

Drilling into the repository is addressed quantitatively in Section 9.4.7 of the SFR-U main report with details given in Sections 5.2.2 through 5.2.4 of the FHA Report (SKB, 2014). This treatment focuses on potential dose resulting from (i) exposure of a drilling crew and (ii) future activities such as construction or cultivations on a drilling detritus landfill. Hydrogeological circumstances do not have a strong bearing on the outcome of these analyses, and therefore no further evaluation is given here. The possibility that such drill holes could be used for domestic or agricultural water supply is considered as part of the intrusion wells scenario.

3.1.2. Intrusion wells scenario

The *intrusion wells* scenario stands out as one of the scenarios that have been assessed in SR-PSU, related to hydrogeological factors that produce doses in excess of the dose corresponding to the risk criterion.

The *intrusion wells* scenario is described in Section 7.6.8 of the SFR-U Main Report and in Section 6.4 of Werner et al. (2013). This considers the possibility of a well for drinking water supply being drilled directly into the repository, sometime after the Baltic shoreline has retreated beyond the repository (ca. 3000 AD).

Results of consequence calculations (given in Section 9.3.8 of the Main Report) show that for a garden-plot household, the annual dose resulting from using drinking water from such a well would exceed the dose corresponding to the risk criterion, for any of the vaults in the early period after 3000 AD, and for most vaults at least until 8000 AD. The exceptions are the BRT and the 1BLA, for which the dose drops off more rapidly. A supplementary calculation shows that the dose for 1BLA, which is initially very high in the base case, is sensitive to the transport properties of U-238, in combination with the flowrates in the 1BLA waste vault.

The risk corresponding to this dose is scaled based on the probability of such a well penetrating a given vault. The method for estimating this probability (described in words rather than as an equation in SKB's report) can be written as:

$$P_{\text{intrusion}} = D_{\text{wells}} \cdot A_{\text{vault}} \cdot f_{\text{depth}}(d_{\text{vault}})$$

where:

D_{wells} = density of wells

A_{vault} = footprint area of each waste vault

d_{vault} = depth below ground surface of a given vault

$f_{\text{depth}}(d_{\text{vault}})$ = fraction of wells that reach or exceed d_{vault}

The values used by Werner et al. (2013) are listed in Table 1. Values of $f_{\text{depth}}(d_{\text{vault}})$ are based on the cumulative frequency of depth for 5,164 wells in northern Uppland (Figure 8). Using these values yields $P_{\text{intrusion}} = 2\cdot10^{-4}$ for a well into the silo, $8\cdot10^{-4}$ for a well into a waste vault in SFR 1, and $3\cdot10^{-4}$ for a well into a waste vault in SFR 3.

Table 1: Factors used by Werner et al. (2013) to calculate probability of well intrusion

Factor	Value	Explanation
D_{wells}	0.5 per km^2	Approximate current density of wells in the Forsmark area
A_{vault} (silo)	800 m^2	Footprint of the silo
A_{vault} (other)	3000m^2	Approximate footprint of other waste vaults
d_{vault} (SFR1)	66 m	Depth of SFR1 below ground surface
d_{vault} (SFR3)	116 m	Depth of SFR3 below ground surface
$f_{\text{depth}}(d_{\text{vault}})$ SFR1	0.5	Based on the cumulative frequency of depth for wells in northern Uppland.
$f_{\text{depth}}(d_{\text{vault}})$ SFR3	0.2	Based on the cumulative frequency of depth for wells in northern Uppland.

In Section 7.6.8 of the Main Report (p. 237), SKB suggests that its treatment of the *intrusion wells scenario* is conservative because the repository is deeper than the typical depth of water supply wells in the Forsmark area. From Werner et al. (2013) and from the above summary, it would seem that well-depth statistics were taken into account in a "realistic" rather than "conservative" way, if all wells are

considered as water-supply wells. However complementary information from SKB (SKB doc ID 1535980) distinguishes between water supply wells vs. "energy" wells (e.g. for heating systems to take advantage of seasonal geothermal gradients). According to this document only 1% of water supply wells go down to 120 m. On the basis of this complementary information, SKB's analysis can be regarded as conservative.
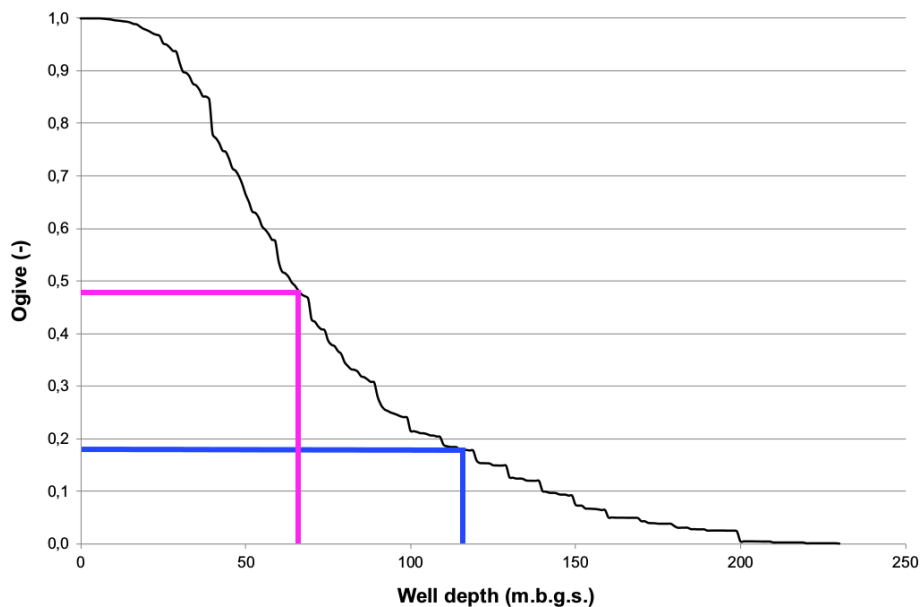
Figure 8: Cumulative frequency (ogive) plot of well depths (meters below ground surface) for 5,164 wells drilled in northern Uppland, from Figure 6-2 of Werner et al. (2013). Magenta line added to show the frequency corresponding to the depth of the SFR (66 m.b.g.s.). Blue line added to show the frequency corresponding to the depth of the SFR (116 m.b.g.s.).

3.1.3. Removal or modifications to the SFR pier

Removal of the SFR pier is discussed in Section 7.7.7 of the Main Report and in Section 5.3 of the FHA Report (SKB, 2014).

The SFR pier is effectively a causeway constructed from coarse, highly permeable materials, atop a natural topographic ridge. Groundwater levels in stand pipes on the pier are generally very close to sea level. SKB argues plausibly that removal or levelling of the coarse materials therefore should not have a significant effect on the local flow pattern at SFR.

Two hydrogeological model representations (Odén et al., 2014; SKBdoc 1395215) compared a case where the groundwater level in the SFR pier is artificially set to be above sea level and with unconstrained contact with the underlying bedrock, versus a more realistic case where groundwater level is low with restricted hydraulic contact to the underlying bedrock. The differences between these cases were

assessed as minor in relation to the situation considered in the high flow in the bedrock scenario.

3.1.4. Underground construction

Underground construction is discussed in Section 7.7.7 of the Main Report (SKB TR-14-01) and in Section 5.4 of the FHA Report (SKB, 2014). The discussion in the FHA Report is limited to qualitative discussion of the impacts of two scenarios:

- FHACC6 – Road or rail tunnel constructed in the vicinity of the repository.
- FHACC7 – A mine in the vicinity of the Forsmark site.

For both of these scenarios, the analysis is limited to two brief paragraphs of qualitative statements, followed by an equally brief summary of the conclusions. These statements and conclusions are repeated in the Main Report.

A road or rail tunnel near the SFR could affect the direction and magnitude of the hydraulic gradient, resulting in larger flows through the waste vaults. The effect could be limited by grouting to limit inflows into such a tunnel, but the possibility cannot be excluded that a tunnel south or east of the repository would affect the hydraulic gradient. SKB considers that the range of possible flows are adequately covered by the high flow in the bedrock scenario.

The possible influence of a mine is considered based on the nearest known area where rock is judged to have at least marginal potential for iron oxide mineralisation, according to SKB's evaluation of ore potential in the area. This area is 3 km inland from the SFR (also on the other side of the Singö Fault). The potential influence on hydrogeological conditions near the SFR is judged to be less than that for the proposed spent-fuel repository, which was analysed by Hellman et al. (2014) and indicated to be negligible.

The Main Report also discusses the possibility of a rock cavern near the repository, which is discussed as a possibility in Sections 4.4.4 and 4.4.12 of the FHA Report. A rock cavern near the repository could affect the hydraulic gradient, particularly if it is kept drained by pumping of groundwater inflows. A cavern could also create new potential transport pathways either to or from the repository. Upconing of more saline water to repository depth could also occur if a subsurface facility is maintained in a rock cavern.

3.2. Analysis

3.2.1. Intrusion wells scenario

The *intrusion wells scenario* is judged to be adequately handled in terms of hydrological issues. However SKB's estimate of the probability of occurrence

$P_{\text{intrusion}}$ is not necessarily conservative. Plausible lines of future evolution could lead to higher values of two of the factors in this calculation, D_{wells} and $f_{\text{depth}}(d_{\text{vault}})$. For example, a warmer climate could plausibly lead to northward shifts in population, and hence more demand for groundwater, at the same time that reduced winter snow accumulations could lead to greater annual fluctuations in groundwater levels, and hence a need for deeper wells. The consequences of such changes for $P_{\text{intrusion}}$ can easily be scoped by considering higher values of D_{wells} and $f_{\text{depth}}(d_{\text{vault}})$.

For example, if the well density doubles so $D_{\text{wells}} = 1.0$ per km^2 and future wells are generally deeper by 20 m, giving $f_{\text{depth}}(66 \text{ m}) \approx 0.25$ and $f_{\text{depth}}(116 \text{ m}) \approx 0.7$, the corresponding probabilities are $P_{\text{intrusion}} = 6 \cdot 10^{-4}$ for a well into the silo, $2 \cdot 10^{-3}$ for a well into a waste vault in SFR 1, and $8 \cdot 10^{-4}$ for a well into a waste vault in SFR 3. These values of $P_{\text{intrusion}}$ can be used to illustrate the sensitivity of SKB's risk calculations to moderately less optimistic assumptions regarding the *intrusion wells* scenario.

3.2.2. Water management by construction of impoundments

One water management scenario not analysed by SKB is the possibility that the SFR pier and/or other artificial causeways in the area could be utilized and modified as part of a dam for a future water impoundment, either for irrigation or as a hydropower resource. Such an impoundment would cause elevated heads over a broader area for infiltration.

Considering how dams for impoundments have been located historically, such an impoundment would most likely make use of existing bedrock topography as well as the artificial causeways left after construction, closure, and abandonment of the SFR.

From examination of the topography and bathymetry, a plausible location for such an impoundment near the SFR could be just west side of the facility, as indicated in Figure 9. This would yield a reservoir with a surface area of about 2 km^2 with depths of 5 m to 10 m, with a need for only a few short sections of berms or dams to connect between existing hillocks and causeways. Such an impoundment would yield approximately a 15 m head difference for small-scale hydropower (either hydroelectric or hydromechanical power utilization), with discharge to nearby lower areas.

Alternatively a smaller impoundment, taking advantage of the existing cooling water channel for the Forsmark nuclear plant and stream flow into that channel, could be built just south of the causeway that leads to the SFR surface facility.

Either situation would create the potential for a head differential of up to 20 m to drive flow through a local groundwater circulation cell, with recharge via a fracture zone located under the impoundment, and discharge via a fracture zone beneath the deeper areas of the present-day seabed, north, north-east, or south-east of the SFR. Thus such a situation would produce an increase in the head differential of 5 m that

was used for the basis of evaluations using the SRM (SSM2917:28, part 2), by up to a factor of 4.

The consequences in terms of the SRM representation are straightforward, because of the linearity of the model. Flowrates through the vaults will increase by a factor of 4, while advective travel times and transport resistance F will decrease by the same factor.
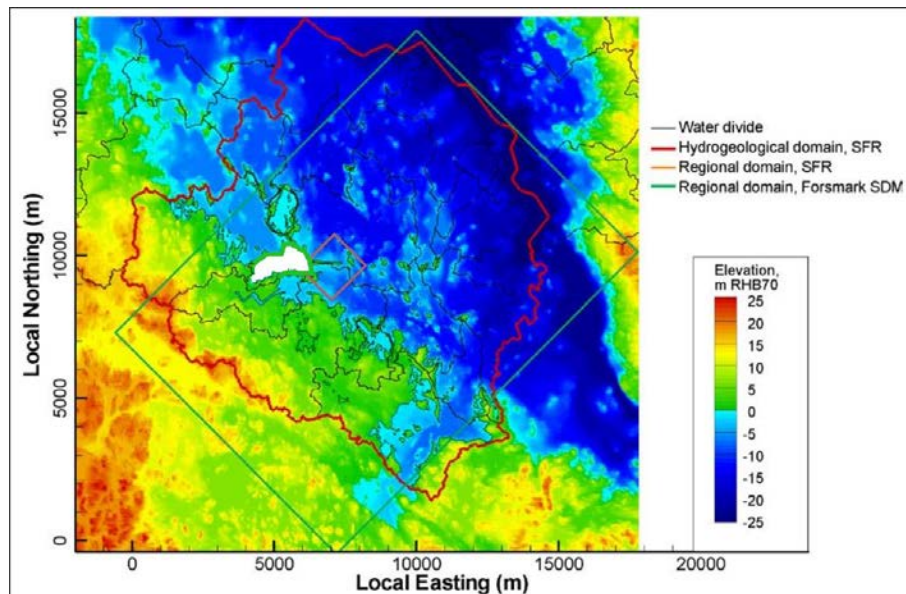
Figure 9: Hypothetical location of a future water impoundment on the west edge of the hydrogeological domain for the SFR modelling, indicated as a white area bordered by green representing berms approximately 5 m RHB70, with elevation and bathymetry of the remainder of the map area indicated by the colour scale.

3.2.3. Quarry or near-surface rock cavern

The analysis by SKB demonstrates that mining for extraction of iron ore or other metals is highly unlikely to occur close enough to have a significant hydrogeological impact on the SFR. However the possibility cannot be excluded that surface excavation could be created while quarrying for building stone, or that a rock cavern could be excavated underground for other purposes such as hydropower generation to balance intermittent sources such as solar or wind power, underground storage of fuel, sequestration of compressible gases, or unforeseen future technologies.

The main hydrogeological effect of such an excavation would occur if a quarry or rock cavern is kept de-watered by pumping of inflowing groundwater, with discharge to a surface impoundment. This could result in an increase of the head gradient through the repository, concordant with the depth of the excavation.

Quarries for building stone are typically less than 20 m deep. For example, the Götemar granite quarry north of Simpevarp in the Oskarshamn region is only 10 to 15 m deep. Present-day rock caverns in the Nordic region can be deeper but are

usually located within a few tens of meters of the bedrock surface according to the FHA Report (SKB TR-14-09).

Set-up of SRM calculation case

To scope the potential effect of a rock cavern on flows through the SFR, a simple calculation case is considered here, of a cavern located within 0.5 km NE of the SFR, with its floor approximately 35 m below the ground level, so that the net difference in hydraulic head for a SRM representation is 40 m.

In place of a vertical fracture zone discharging to the surface as Segment VI of the SRM model (referring to the numbering of segments in Figure 1), this segment is considered to represent a sub-horizontal fracture zone that connects between the rock mass around the SFR and base of the rock cavern. The properties of the discharging deformation zone are based on the sub-horizontal zone ZFMB10.

It is assumed that an underground storage cavern would either avoid a direct intersection with a deformation zone, or use engineering measures such as grouting to limit inflow. In the SRM this is represented by assigning properties based on a 1 m thickness of the rock mass to Segment VII (in place of treating this segment as regolith).

Results

Results of SRM calculations for this case (Figure 10) show an increase of roughly a factor of four to five in median flowrates through the vaults in both the SFR 1 and SFR 3, relative to the results for the main scenario. This increase is mainly due to the increased head gradient. Advective travel times and transport resistance F are decreased by corresponding factors.
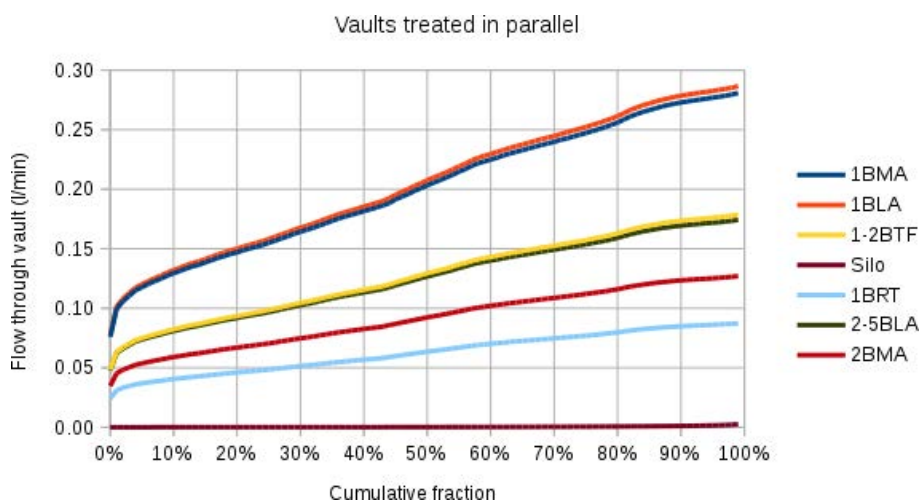
Figure 10: Distributions of flowrates for a simplified representative model of flow to a rock cavern producing a net hydraulic differential of 40 m through the SFR, with ECPM properties for

the recharge and discharge paths, and discharge via a sub-horizontal zone with properties similar to ZFMB10, based on 10,000 realizations. The plot shows flowrates for the case where each of the vaults within each section of the repository are treated as conductors in parallel, and can be compared with the lower plot in Figure 3.

4. Wells downstream of the repository

The *wells downstream of the repository* scenario stands out as one of the scenarios that have been assessed in SR-PSU, related to hydrogeological factors, that produce doses in excess of the dose corresponding to the risk criterion, or doses close to that level. Preliminary review identified this as a scenario that merits further review to assess the conservatism of the hydrogeological analysis, including the potential impact of uncertainty in the shallow bedrock hydrogeological model, and sensitivity to SKB's risk-scaling method.

4.1. Previous analysis by SKB

The *wells downstream of the repository* scenario considers the possibility that future human inhabitants could drill wells downstream of the repository after the Baltic shoreline retreats beyond the repository footprint, and that these future inhabitants would then utilize water from these wells for domestic purposes. The analysis is summarized in Section 7.6.7 of the SFR-U Main report, with details given in Section 6.4 of Werner et al. (2013)

The land in the vicinity of the SFR is expected to stay below Baltic Sea level for at least 1000 years after closure, so this scenario does not arise until after 3000 AD.

The analysis considers the possibility that wells could be drilled in the direct vicinity of the repository any time after as soon as land has emerged to at least 1 meter above sea level. A *well interaction area* is delineated as an area where flow pathways passing through the repository have a high density, within a depth interval from 10 to 80 m below present-day sea level. This depth interval corresponds into a typical depth for a bedrock well in this area.

The risk contribution from this scenario takes into account the probability of drilling in the well interaction area:

$$P_{\text{interaction}} = D_{\text{wells}} \cdot A_{\text{interaction}}$$

where:

$A_{\text{interaction}} =$ the area of the well interaction area

and D_{wells} is the density of wells as defined previously for the *well intrusion* scenario. The value used for $A_{\text{interaction}}$ in SKB's risk assessment is 0.26 km^2, yielding a value $P_{\text{interaction}} = 13\%$.

The results for this scenario are presented in Section 9.3.7 of the main report. For one category of exposed group (a garden plot household), the total dose comes close to this risk-equivalent dose from around 3500 AD to 5000 AD, at which point the risk criterion is briefly exceeded. For other types of exposed groups the dose remains well under the level that corresponds to the risk criterion.

The dose and consequent risk to future humans depend on the concentration of radionuclides in water pumped from a well. To support estimation of concentrations, Werner et al. (2013) modelled capture of radionuclides for a sample of 9 wells

located within the well interaction area. Their analysis was based on the DarcyTools base case model set-up for 5000 AD as described by Öhman and Vidstrand (2014). For each well, a steady-state flow solution was calculated for a nominal pumping rate of Q_{well} = 700 L/d withdrawn from the highest-conductivity grid cell penetrated by the well. Then forward particle tracking was used to determine the fraction of flow paths passing through any given vault v that arrives at the well. This fraction (denoted f_v for brevity in this report) is taken as the *radionuclide capture ratio*: i.e. the fraction of the rate of radionuclides released from a given vault that would arrive at the well.

The results of these calculations are given in tabular form in Appendix 3 of Werner et al. (2013). The numerical values are plotted here in Figure 11.

From Figure 11 it can be seen that, for most wells and most vaults, the capture ratio f_v is less than 10%. Average values over the ensemble of nine wells are generally below 5% for any given vault. However one well (Well 29) receives more than 30% of the radionuclide flux from 2BTF and 1BLA, 23% for 1BTF, and 17% for 1BMA. Two other wells (Wells 23 and 25) receive more than 10% of the radionuclide flux from particular vaults in SFR 3.

The concentration of radionuclides in the drinking water for safety assessment can then be calculated as:

$$C_{rn} = \sum_v \frac{R_v f_v}{Q_{well}}$$

where R_v is the radionuclide flux (expressed in in Becquerels per unit time).
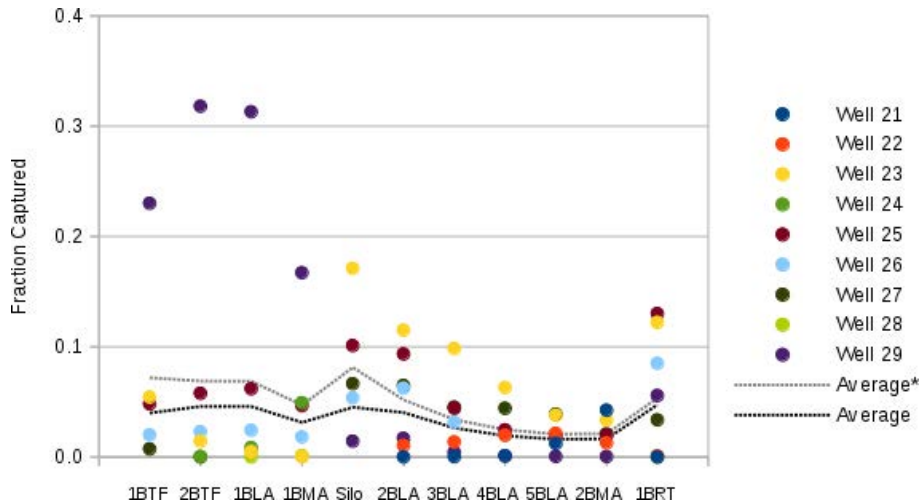
Figure 11: Fraction of tracked particles from each vault, arriving to nine different wells (Wells 21–29) for a simulated pumping rate of 700 L/d, in the base-case model for 5000 AD as described by Öhman and Vidstrand (2014). Plot based on numerical values given in Tables A3-2 and A3-3 of Werner et al. (2013). The gray dotted line labeled "Average*" shows average values for each vault as calculated by Werner et al. (2013), excluding wells with zero arrivals

from a given vault. The black dotted line labeled "Average" is the average including all nine wells.

Werner et al. (2013) recommend using a value $f_v = 10\%$. They also consider the sensitivity of the radionuclide capture to pumping rate, by extending this analysis to a series of increasing pumping rates Q_{well} for one well (Well 29). They state that the relation between capture ratios f_v and Q_{well} is linear for most SFR facility parts, so the effect of increasing capture is offset by dilution by the greater pumping rate.

A plot of these results (Figure 12) shows that this relation is indeed linear or sub-linear (logarithmic slope equal to 1 or less) for four of the vaults (1BRT, 1BMA, 1BTF, and 2BTF). However for the remaining vaults, the logarithmic slope of capture ratio vs. Q_{well} is greater than 1, and approaches 1.5 for the higher values of Q_{well}. The implications of this are discussed in the analysis below.
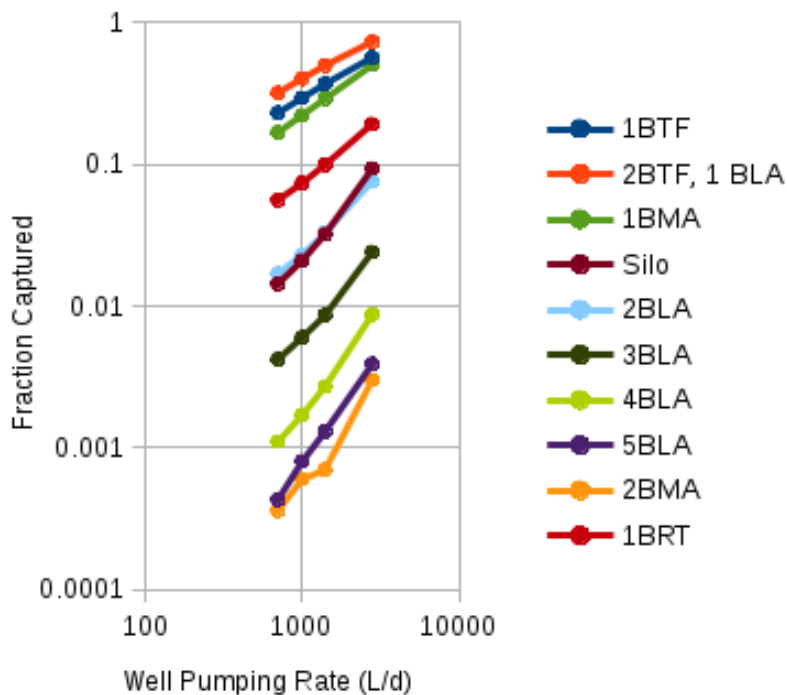
Figure 12: Influence of pumping rate on capture ratios for tracked particles from each vault, for a selected well (Well 29) in the base-case model for 5000 AD as described by Öhman and Vidstrand (2014). Plot based on numerical values given in Tables A3-4 of Werner et al. (2013). The values for 2BTF and 1BLA are very close numerically, and indistinguishable on this plotting scale, so have been plotted as a single line.

4.2. Analysis

The analysis by Werner et al. (2013) is reasonably conservative with respect to the results of the single hydrogeological modelling case on which it was based, but it does not consider the potential impact of uncertainty in the shallow bedrock

hydrogeological model, nor does it fully take into account uncertainties related to future density of well densities in the area, or capture ratios as a function of well location and pumping rates.

4.2.1. Uncertainty in capture ratios

For estimating capture ratios, only a single hydrogeological model set-up has been used. This was the base case model set-up for 5000 AD as described by Öhman and Vidstrand (2014), considering just a single realization of the DFN model.

Within that model set-up, only nine well locations have been tested. These were chosen by an *ad hoc* procedure to be within an area that is relatively likely to received discharge from the SFR. One of these nine wells produces anomalous results, in that capture ratios f_v for three vaults in SFR 1 are more than 6 times the average value of f_v for the ensemble, and more than 3 times the value of f_v that was used for consequence calculations based on this scenario.

The possibility cannot be excluded that even higher values of f_v would be obtained by considering more well positions and additional realizations of the DFN model, up to the maximum possible value $f_v = 100\%$. While such an extreme value of f_v is unlikely for a randomly located well within the downstream well interaction area, the value $f_v = 30\%$ is plausible as it arises even from the very limited ensemble of simulations.

The sensitivity cases with respect to Q_{well} (Figure 12) indicate that, contrary to the summary of results by Werner et al. (2013), f_v could be roughly proportional to $Q_{well}^{3/2}$ rather than scaling linearly with $Q_{well.}$. This implies that with increasing pumping rates, the radionuclide concentration in the well could increase roughly in proportion to the square root of Q_{well} (rather than remaining constant). Thus for a factor of 4 increase in Q_{well}, the concentration C_{rn} could double as a result of enhanced capture.

A conservative assessment of the potential dose from a downstream well should therefore consider an increase in C_{rn} of at least a factor of 2 (reflecting possible effects of enhanced capture by higher pumping rates) and preferably 3 (reflecting the effects of spatial heterogeneity indicated by the single realization considered). An even more conservative assessment, taking into account both of these factors, could consider a factor of 6 increase in C_{rn}.

4.2.2. Sensitivity of risk scaling method

As discussed above in connection with the intrusion wells scenario, the risk scaling method is sensitive to assumptions in its two factors: well density D_{wells} and the interaction area $A_{interaction}$.

The first factor, D_{wells}, has been estimated based on the present-day density of wells

in the area. A factor of two increase in well density is certainly plausible for a more populated future landscape.

The second factor, $A_{\text{interaction}}$, has been estimated from a single hydrogeological model set-up using a single realization of DFN model. A larger interaction area is certainly plausible, but this implies a larger spread of flow paths emanating from the repository, and thus likely would be associated with smaller capture ratios f_v which would lead to smaller radionuclide concentrations in the dose calculations. Thus it seems unnecessary to consider larger values of $A_{\text{interaction}}$, as the effect in the risk scaling is likely to be offset by a reduction in the corresponding dose.

5. Impact of seasonal fluctuations on far-field transport

SKB hydrogeological modelling in support of SR-PSU do not include seasonal fluctuations in the groundwater levels. Considering the shallow depth of the facility, seasonal fluctuations in the water table could potentially contribute significantly to dispersion in the far-field.

Periodic fluctuations in groundwater levels can conceivably affect dispersion and early arrivals of radionuclides in the biosphere. In the Baltic environment, tidal influences are a minor influence. More significant fluctuations occur due to seasonal storm surges and weather cycles.

5.1. Analytical solution

As part of the investigation of possible effects, analytical models were considered. A literature search found that Jaiswal et al. (2011) published a general analytical solution for one-dimensional advective-dispersive transport with time-varying diffusion coefficients and velocity:

$$\frac{\partial C}{\partial t} = \frac{\partial}{\partial x}\left\{D(x,t)\frac{\partial C}{\partial t} - u(x,t)C\right\}$$

where:

C = concentration

$D(x,t)$ = dispersion coefficient as a function of distance x and time t

$u(x,t)$ = advective velocity as a function of distance x and time t

For the case of initial condition of $C = 0$ throughout the system and a uniform point source $C = C_0$ at $x = 0$ starting at $t = 0$, with uniform $D(x,t) = D_0$ but time-varying velocity $u(x,t) = u_0 f(mt)$, with m a constant, the solution of Jaiswal et al. (2011) can be written as:

$$C(x,t) = \frac{C_0}{2}\left\{erfc\left(\frac{xf(mt) - u_0 T}{2\sqrt{D_0 T}}\right) + exp\left[\frac{u_0 x}{D_0}f(mt)\right]erfc\left[\frac{xf(mt) + u_0 T}{2\sqrt{D_0 T}}\right]\right\}$$

where T is a time-dependent variable defined by the integral transformation:

$$T = \int_0^t f^2(m\tau)d\tau$$

For the simple periodic case in which velocity varies as a sine wave about a mean value:

$$f(mt) = 1 + asin(mt)$$

where a is an amplitude factor for the temporally variable component of velocity, this evaluates as:

$$T = t + \frac{2a}{m}[1 - cosmt] + \frac{a^2}{2}\left[\frac{t - sin(2mt)}{2m}\right]$$

It may be noted that when the amplitude factor $a = 0$, $T = t$ and the solution simplifies to:

$$C(x,t) = \frac{C_0}{2}\left\{erfc\left(\frac{x - u_0 t}{2\sqrt{D_0 t}}\right) + exp\left[\frac{u_0 x}{D_0}\right]erfc\left[\frac{x + u_0 t}{2\sqrt{D_0 t}}\right]\right\}$$

which is the familiar solution for steady-state flow with velocity u_0.

5.2. Results and discussion

The analytical solution described above was evaluated for the idealized situation where groundwater velocities vary over an annual cycle (i.e., $m = 2\pi /(1$ year)), and for a representative mean velocity $u_0 = 5$ m/yr, while varying the amplitude factor a and the dispersion coefficient D_0.

Results of these calculations are shown in Figure 13. The plot in the upper left corner of the figure shows the case of steady flow ($a = 0$), with effective dispersion controlled entirely by the dispersion coefficient D_0.

For a small seasonal variation in groundwater velocity ($a = 0.1$) combined with low dispersion coefficient $D_0 = 1\times10^{-7}$ m²/s, as shown in the second plot in the left-hand column, the main effect is a steeper increase in early arrivals, at distances of 20 m or 50 m which could be representative of radionuclide transport distances through the rock mass. However the overall spread of arrival times is similar to that for the steady-flow case. Thus the effective far-field dispersion for the entire solute arrival curve is not strongly affected by this degree of seasonal variation.

A higher value of $D_0 = 1\times10^{-6}$ m²/s combined with increasing seasonal amplitudes for groundwater velocity (plots in right column) leads to more pronounced effects on the magnitudes of early arrivals, although the effective far-field dispersion still is not strongly affected.

For the case where the amplitude of the seasonal fluctuations is half of the mean groundwater velocity (plot for $a = 0.50$ in the lower right-hand corner of Figure 13), an initial peak concentration of more than 10% of the source concentration can arrive as early as 1.5 years after release, compared with around 5 years for the case with $a = 0.10$.

This analysis does not take into account the effects of matrix diffusion and sorption which would delay arrivals of radionuclides overall. These mechanisms would delay the arrival of transient peaks produced by the combination of dispersion and variable velocity, in these results. The overall effect would likely be to "smooth out" the effects of variable velocity.
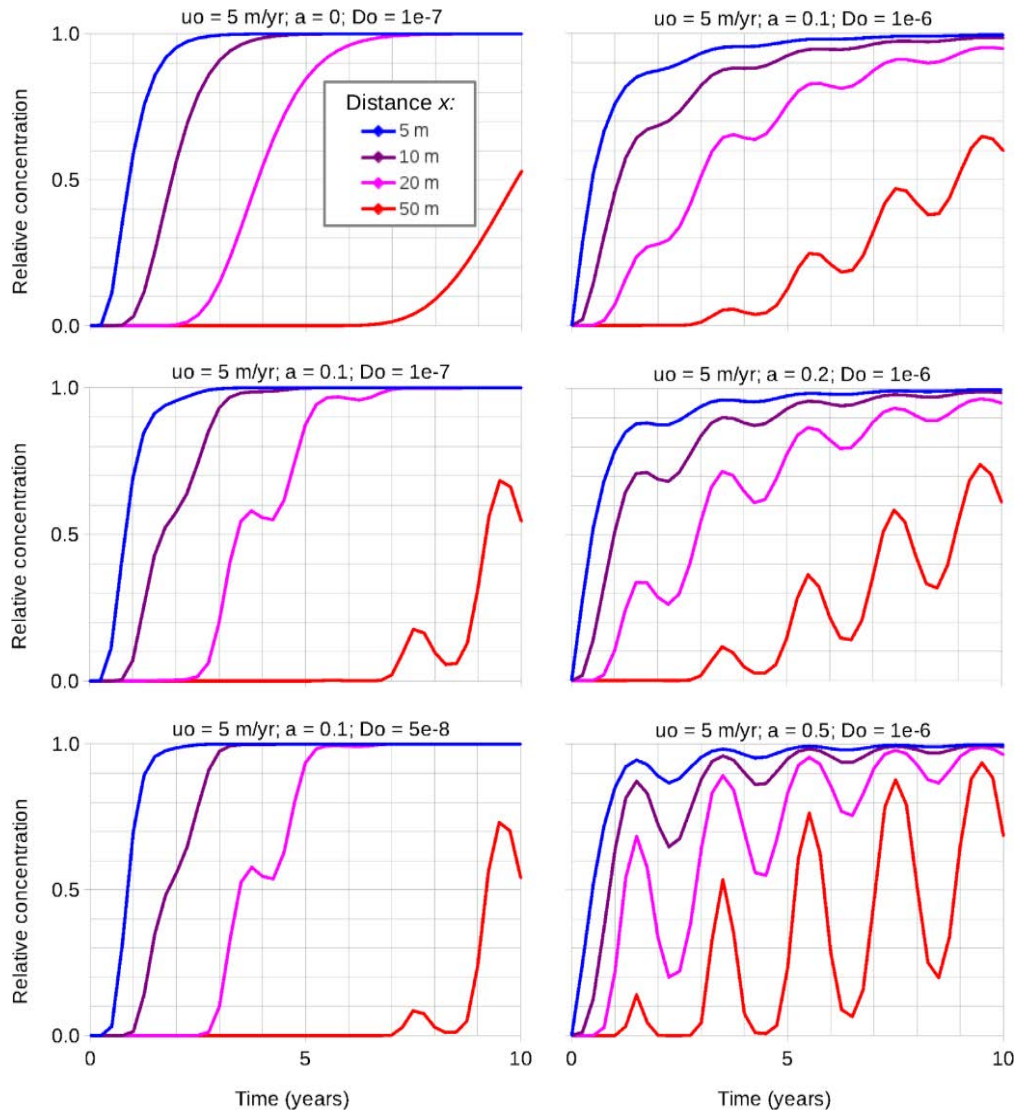
Figure 13: Influence of time-varying velocity on relative solute concentration C/C_0 in a 1-D transport path at different distances x from the source, for a flow field with mean velocity $u_0 = 5$ m/y, with an annually varying component of amplitude au_0, for different values of a and the dispersion coefficient D_0, as indicated in the text above each plot. Different colour lines indicate the distance from the source, according to the legend given in the uppermost left plot.

However, so far as sorption is reversible, local concentrations produced by seasonal groundwater surges near the advancing radionuclide migration front would act as sources for radionuclide migration during the rest of the year.

Analytical solutions taking into account variable groundwater velocities along with matrix diffusion and sorption are seemingly not available, based on the literature survey carried out for this project. Numerical calculations using simple 1-D particle-tracking models or network particle-tracking models with explicit treatment of matrix diffusion (such as given by Geier, 2005) could clarify the significance of this issue.

6. Conclusions

Estimated distributions of transport parameters based on a simplified representative model (SRM) approach are presented in Chapter 2. Transport resistance in brittle deformation zones (fracture zones) is found to be a significant part of the overall transport resistance, which must be taken into account in order to obtain values comparable to those obtained by SKB. This is in contrast to the expected results based on prior modelling of high-level radioactive waste repositories, located much deeper in the bedrock.

The treatment of brittle deformation zones in this analysis is highly idealized, and does not take into account complications of fault zone architecture such as presence of gouge or breccias with alteration. The apparent significance of these zones was not obvious from SKB's analyses, which presented integrated results from a complex model in which these features were embedded.

Consequences of future human actions are evaluated in Chapter 3. More conservative estimates are recommended for the probability of the *intrusion wells scenario*, considering the possibility of future population increases and corresponding demand on groundwater resources, including more and deeper wells.

Scoping calculations for the scenario of a water impoundment (not evaluated by SKB) indicate that this could increase flowrates through the waste vaults by about a factor of 4, while advective travel times and transport resistance would decrease by the same factor.

Construction of a 40 m deep rock cavern within half a kilometre of the SFR could lead to an increase of similar magnitude in flowrates through the vaults, and corresponding decreases in advective travel times and transport resistance.

SKB's evaluation of the *wells downstream scenario* appears to be non-conservative because evidence of greater-than-linear scaling of capture ratios, as a function of well pumping rates, were overlooked. A conservative treatment should consider a factor of two increase in concentrations (reflecting possible effects of enhanced capture by higher pumping rates) and preferably 3 (reflecting the effects of spatial heterogeneity), or more conservatively, a factor of six to take both of these factors into account. The risk scaling method for this scenario could also be viewed as mildly optimistic, as it fails to take into account a possible future increase in well densities.

The possible influence of seasonal fluctuations in groundwater levels has been investigated in a preliminary way, making use of an analytical solution for 1-D advective-dispersive transport for temporally varying groundwater velocities. The results indicate that effective dispersion in the far field is not substantially affected, but seasonal variations can have a significant effect on early arrivals, for the transport mechanisms considered. This analysis did not account for matrix diffusion or sorption, which were not accounted for in the available analytical solutions. Further analysis using particle-tracking methods in 1-D systems or simple fracture networks should provide more definitive conclusions on the potential significance of seasonal groundwater variations for far-field transport.

7. References

Abarca, E., Idiart, A., de Vries, L.M., Silva, O., Molinero, J., and von Schenk, H., 2013. Flow modelling on the repository scale for the safety assessment SR-PSU. SKB TR-13-08, Svensk Kärnbränslehantering AB.

Geier, J., 2017. Hydrogeological assessment and calculations to support the review of SR-PSU. In SSM Report 2017:28, SSM's external experts' review of SKB's safety assessment SR-PSU - hydrogeology, geochemistry and bentonite – Main review phase. Swedish Radiation Safety Authority, Stockholm.

Geier, J., 2018. Simplified representative model calculations of effects of uncertainty in rock mass hydrogeological properties on flows through SFR vaults. SSM project memorandum, 27 May 2018.

Geier, J., Lindgren, G., Tsang, C., 2019. Simplified representative models for long-term flow and advective transport in fractured crystalline bedrock. *Hydrogeology Journal*, vol. 27, p. 595-614.

Hellman, H., Vidstrand, P., and Sassner, M., 2014. Hydrogeologisk utredning rörande befintlig SFR och planerad utbyggnad. SKBdoc 1346469, Version 1.0.

Jaiswal, D.K., Kumar, A., and Yadav, R.R., 2011. Analytical solution to the one-dimensional advection-diffusion equation with temporally dependent coefficients. Journal of Water Resource and Protection, v. 3, p. 76-84. doi:10.4236/jwarp.2011.31009

Kautsky, U. (ed.), 2001. The biosphere today and tomorrow in the SFR area. SKB R-01-27, Svensk Kärnbränslehantering AB, Stockholm.

Odén, M., Follin, S., Öhman, J., and Vidstrand, P., 2014. SR-PSU Bedrock hydrogeology. Groundwater flow modelling methodology, setup and results. SKB R-13-25, Svensk Kärnbränslehantering AB, Stockholm.

SKB, 2013. Site description of the SFR area at Forsmark at completion of the site investigation phase, SDM-PSU Forsmark. SKB TR-11-04, Svensk Kärnbränslehantering AB, Stockholm.

SKB, 2014. Handling of future human actions in the safety assessment SR-PSU. SKB TR-14-08, Svensk Kärnbränslehantering AB, Stockholm.

SKBdoc 1395200: TD05-Effects in ECPM translation. SKB Promemoria (PM) publication. Version 1.0, 2013-05-16. Svensk Kärnbränslehantering AB, Stockholm.

SKBdoc 1395214: TD08- SFR3 effect on the performance of the existing SFR1. SKB Promemoria (PM) publication. Version 2.0, 2013-05-16. Svensk Kärnbränslehantering AB, Stockholm.

Sohlenius, G., Strömgren, M, and Hartz, F., 2013. Depth and stratigraphy of regolith at Forsmark. SR-PSU Biosphere. SKB R-13-22, Svensk Kärnbränslehantering AB, Stockholm.

Werner, K., Sassner, M., and Johansson, E., 2013. Hydrology and near-surface hydrogeology at Forsmark –synthesis for the SR-PSU project. SKB R-13-19, Svensk Kärnbränslehantering AB, Stockholm.

Öhman, J., Bockgård, N., and Follin, S., 2012. Site investigation SFR. Bedrock hydrogeology. SKB R-11-03, Svensk Kärnbränslehantering AB, Stockholm.

Öhman, J., and Follin, S., 2010a. Site investigation SFR. Hydrogeological modelling of SFR. Data review and parameterisation of model version 0.1. SKB P-09-49, Svensk Kärnbränslehantering AB, Stockholm.

Öhman, J, and Follin, S., 2010b. Site investigation SFR. Hydrogeological modelling of SFR. Model version 0.2. SKB R-10-03, Svensk Kärnbränslehantering AB, Stockholm.

Öhman, J., Follin, S., and Odén, M., 2013. Site investigation SFR. Bedrock hydrogeology – Groundwater flow modelling. SKB R-11-10, Svensk Kärnbränslehantering AB, Stockholm.

Öhman, J., Follin, S., and Odén, M., 2014. SR-PSU Hydrogeological modelling TD11 – Temperate climate conditions. SKB P-14-04, Svensk Kärnbränslehantering AB, Stockholm.

Öhman J, Vidstrand P, 2014. SR-PSU Bedrock hydrogeology. TD12 – Water-supply wells in rock. SKB P-14-05, Svensk Kärnbränslehantering AB.

Authors: Joel E. Geier, Clearwater Hardrock Consulting, Corvallis, USA

Evaluation of hydrogeological risks associated with water-supply wells in a future warmer climate

Abstract

Consequences of a future warmer climate for groundwater demand, relative sea level changes and potential saline intrusion are considered. Predicted seasonal temperatures and precipitation based on regional climate modeling of the near future (on the order of centuries) are used to identify crops that could be suitable for cultivation and to estimate the consequent potential future demands on groundwater resources for irrigation.

Predicted future climates for realistic global-warming scenarios are expected to produce higher mean monthly temperatures, longer growing seasons, and reduced or negligible snow accumulations during a shorter winter season. Although the climate models typically indicate greater annual precipitation, this may be insufficient to meet an increased water demand for irrigation of crops suitable to the predicted future climate, mainly due to the longer growing season.

Cultivation and irrigation of such crops using well water would likely exceed the available groundwater resources, even if only part of the future arable land is cultivated intensively. Comparison with similar cases from coastal agricultural areas in temperate climates indicates that local drawdowns due to intensive irrigation would draw water from the direction of the sea, leading to inland movement of brackish water as well as upconing of deeper brines. Such intensive water use would ultimately be limited by salt-water intrusion making individual wells unusable. However case studies from the most similar environments indicate that the response of irrigators may be simply to abandon such wells, and drill new wells nearby. Such practices could maintain saline conditions around the current SFR and its proposed extension for an extended period into the future.

Contents

1. Introduction

The Swedish Radiation Safety Authority (SSM) has been reviewing an application by the Swedish Nuclear Fuel and Waste Management Co. (SKB) to expand an existing underground repository for low- and intermediate-level radioactive waste, the SFR. In support of this review, Clearwater Hardrock Consulting has used simplified representative models (SRMs) to address questions related to hydrogeology that were identified in previous stages of SSM's review. This included an assessment of conservatism in SKB's "wells downstream of the repository" scenario (see companion review by Geier, 2019). Further consideration of this topic has yielded questions about the potential influence of a future, warmer, drier climate, possibly leading to coastal saltwater intrusion, on the assumptions used in this scenario.

A future warmer climate in the northern Baltic region can reasonably be anticipated as the consequence of global climate change, as considered in predictive climate modeling by Kjellström et al. (2009) for Forsmark and similar work by Pimenoff et al. (2011, 2012) for the Olkiluoto site in Finland. This could lead to increased demand for fresh groundwater near the coast for agricultural, household, and industrial uses. This could be exacerbated if the balance between future precipitation and evapotranspiration changes, leading to reduced potential recharge. Lower levels of fresh groundwater result in a need for deeper fresh water wells. However, it can also result in inland movement of brackish waters from the Baltic, driven by density differences. This process should be offset at least in part by land rise due to ongoing post-glacial isostatic rebound (Påsse, 2001), but global climate change is also expected to bring an increase in global sea levels due to melting of polar ice sheets. Additionally, groundwater depletion in the Forsmark area could cause up-coning of older saline groundwaters, including relict waters from the Littorina Sea and more ancient, deeper brines.

The balance among these various processes needs to be taken into account to assess the likely extent of salt-water intrusion, and to formulate reasonable predictions of how this could influence future patterns of well drilling, well pumping, and hence affect radiation risk due to leaching of radionuclides from the SFR. For the hydrogeology of the Forsmark area, account must also be taken of the likely correlation between pumped intervals of water wells, and high-yield fracture zones that could connect directly or indirectly to the sea floor.

To improve the basis for addressing these concerns, the following approach is taken:

- Identification of plausible sequences of evolution for seasonal temperatures and precipitation based on regional climate modeling, for situations corresponding to the "global warming" and "extended global warming" climate scenarios considered by SKB (2014).
- Estimation of irrigation well requirements for typical crops suitable for these expected warmer future climates (this analysis does not consider the potential needs of crops for particular soils, but only climate requirements).
- Survey of relevant case studies of salt-water intrusion in temperate regions of Eurasia and North America, focusing especially on coastal regions with crystalline bedrock, to identify typical patterns of response in terms of well depths and well density for a given population.

Analyses of these topics are presented in the following three chapters. Overall conclusions are presented in the final chapter.

2. Plausible future climates

Regional climate modeling by Kjellström et al. (2009) yielded predictions of temperatures and precipitation for a future warmer climate. They compare results from the experiments for all three cases with simulation of the recent past (RP-r) climate simulation (reference period 1961–1990).

The model variant considered here (labelled WARM-r-veg by Kjellström et al., 2009), takes into account projected changes in vegetation due to the warmer climate. The main projected change in vegetation for the Baltic region is a northward expansion of areas with temperate deciduous broadleaf forest and a northward shift of boreal evergreen conifer forest into areas that currently are characterized by boreal shrubs or arctic grasses.

2.1. Future temperatures

For the warm-climate scenario, mean monthly temperatures in Sweden in winter and early spring are predicted to increase by 4 C to 6 C, relative to simulations of the recent past (Figure 1). Late spring, summer and fall temperatures are predicted to increase by 2 C to 3.5 C.

The predicted increase in late fall, winter and spring temperatures is enough to reduce the period with mean temperatures below 0 C from five months (November through March) to just two months (January and February), when the mean monthly temperature is just barely below freezing (–1 C) according to the simulations.

Such a situation would imply little or no snow accumulation during the winter, i.e. any snow would likely thaw during freeze-thaw cycles over a period of one day to a few weeks. This implies that all or nearly all precipitation during the winter months would quickly either run off as overland flow and stream discharge or infiltrate as groundwater recharge, rather than being retained as snow/ice on until a spring thaw. This, together with the longer growing season, could in turn lead to greater demands on groundwater resources for irrigation and other uses.

Some discrepancies between the model of recent past climate (RP-r) and recent observed temperatures across Sweden may be noted by comparing the solid red and green lines in from Figure 1. Recent observations indicate significantly more extreme variation (warmer summers and colder winters) than yielded by the model of the recent past. If this variation carries over into the expected future, warmer climate period, then summers could be hotter than predicted, and also winters could be colder, with the prospect of retaining more snow pack.
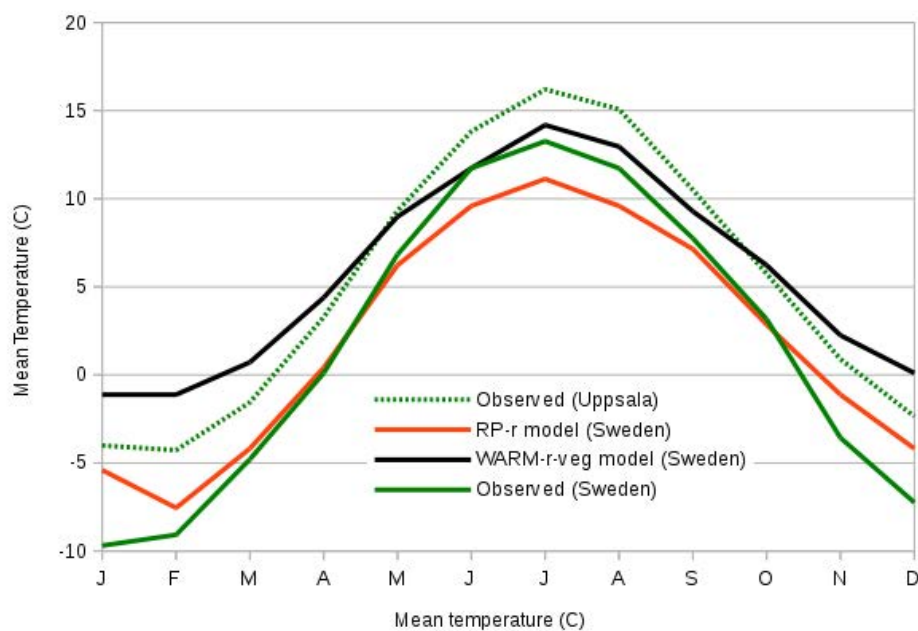
Figure 1: Mean monthly temperatures in Sweden predicted for simulations of a warmer future climate (variant WARM-r-veg) compared with simulations of the recent past (RP-r) and observations for the reference period, based on digitized data presented graphically by Kjellström et al. (2009, Figure 3-7). Recent observed temperatures from Uppsala for 1901-2000 are also shown for comparison as a dotted green line (based on Brandefelt, 2013, Figure 2-4)

Observed temperatures within the Uppland region near Forsmark are generally warmer than the average over Sweden as a whole. This can be seen from the recent historical data for Uppsala (about 50 km south of Forsmark), included as a dotted green line in Figure 1.

Climate model predictions for a roughly 100 km x 100 km square region (corresponding to 9 grid cells in the RCA 3 model) around Forsmark are presented in Section 4.2.1 of Kjellström et al. (2009). On this scale, the model-calculated temperatures for the recent past (Figure 2) show good agreement with observations, only slightly under-predicting summer high temperatures and winter low temperatures by 1-2 degrees C.

Table 1: Monthly temperatures observed and predicted for the region. Data digitized from SKB TR-09-04, Figure 3-7 (for observed and predicted future warm climate in Sweden) and SKB TR-13-05 Figure 3-36 (current Forsmark and future warm climate at Forsmark). Errors in digitization are estimated as ±0.2 C based on the resolution of the plots.

Month	Temperature (C)				
	Current Forsmark	Future warm climate at Forsmark	RP-r model (Sweden)	Warm-r-veg model (Sweden)	Observed Sweden
January	-4.2	-0.1	-5.4	-1.1	-9.7
February	-4.4	+0.1	-7.6	-1.1	-9.1
March	-1.4	+2.5	-4.2	+0.7	-4.8
April	+3.2	+7.7	+0.4	+4.4	+0.1
May	+8.3	12.4	+6.2	+9.0	+6.8
June	14.0	15.9	+9.6	11.7	11.7
July	15.7	17.7	11.1	14.2	13.3
August	14.3	16.9	+9.6	13.0	11.7
September	10.6	13.2	+7.1	+9.3	+7.8
October	+6.5	+8.7	+2.9	+6.2	+3.2
November	+1.5	+3.6	-1.1	+2.2	-3.6
December	-2.2	+0.9	-4.2	+0.1	-7.2
Annual average	+5.2	+8.3	+2.1	+5.8	+1.7

2.2. Future precipitation and snow cover

Model predictions of monthly precipitation (Figure 3) predict an overall increase of 137 mm (or 20%) in annual precipitation (Table 2), with the additional amount coming mainly in the cooler part of the year (October through June). Close to half of this increase might be due to an upward bias in the model which is apparent from the model results for the recent past. Kjellström et al. (2009) suggest that part of this discrepancy might be due to undersampling of winter precipitation, and they note generally high uncertainty in estimates of future precipitation. The minimum values for the warmer climate case indicate a possibility for conditions that are locally drier than the recent past, during the summer months of July through September.
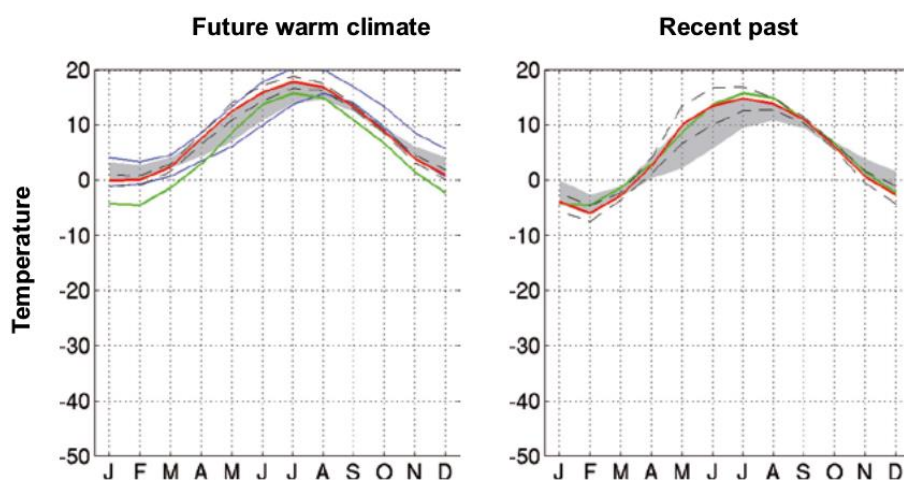
Figure 2: Simulated temperatures for a model of a future warmer climate (red line in graph at left) and a model of the recent past (red line in graph at right), for a 3 x 3 grid centered on the grid box of the RCA 3 climate model that contains Forsmark. In both graphs, the solid green line shows local observed data for the recent period 1961–1990. Dashed lines indicate spatial variability in the 3 × 3-grid, representing ±1 standard deviation calculated from the 9 grid boxes. The gray area represents the absolute maximum and minimum of the 9 grid boxes. The solid blue lines for the future warm climate represent a ±1 standard deviation of the spatial variation from for three additional simulations for the 21st century. Excerpted from Figure 3-36 of SKB (2014) and Figure 4-7 of Kjellström et al. (2009)

For a future warm climate, the predicted temperatures in the Forsmark area are on average 2.6 C higher than for Sweden as a whole (Table 1). The future warming is stronger in winter than in summer, leading to a likelihood of the snow season around Forsmark being much shorter, with greatly reduced snow cover or even a complete lack of snow cover (Figure 4). Winter precipitation that falls as rain will mostly run off immediately rather than being stored on land as snow. This leads to greatly reduced potential for a spring runoff peak due to snowmelt.

Taken together, these results indicate a longer, warmer or hotter growing season with potential for crops that require water over longer periods. This is likely to be combined with reduced rainfall over middle/late parts of the growing season, when these crops have developed more leaf area for evapotranspiration. The minimal water storage as snow cover during winter, both near Forsmark and farther inland, means that stream flows could decline quickly after spring rains. All of these factors point toward a potentially increased demand for groundwater for irrigation and/or household use in the later part of the season. Relatively high uncertainty in the model predictions of future precipitation means that the potential for much drier and/or variable summer precipitation patterns could accompany some stages of a warmer future climate.

Table 2: Monthly precipitation observed and predicted for the region. Data digitized from SKB TR-13-05 Figure 3-36). Errors in digitization are estimated as ±0.5 mm based on the resolution of the plot.

Month	Precipitation (mm)		
	Current Forsmark	RP-r model (Sweden)	Warm-r-veg model (Sweden)
January	36.8	48.5	62.3
February	26.7	42.2	59.7
March	28.4	40.1	55.6
April	32.6	46.8	56.0
May	32.6	47.2	65.6
June	40.9	62.3	78.6
July	63.5	71.0	78.1
August	71.9	66.9	61.8
September	61.4	58.1	58.1
October	49.3	57.7	72.3
November	53.5	58.1	75.2
December	43.9	63.5	75.6
Annual average	541.5	662.3	789.9
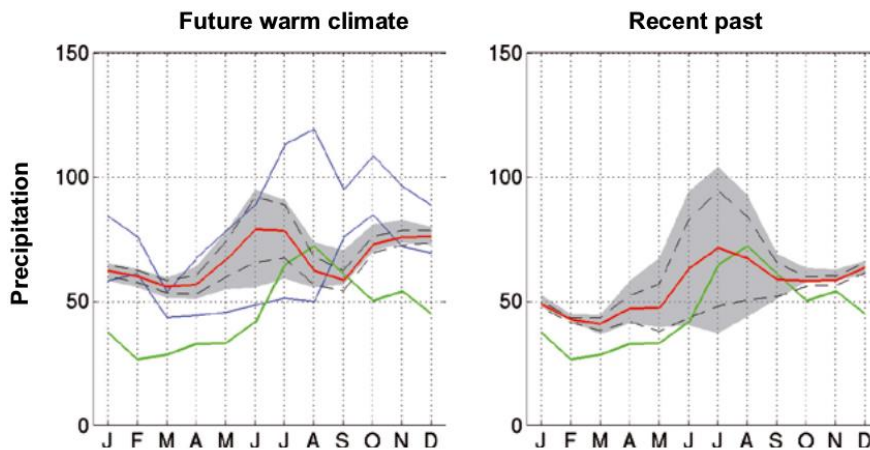
Figure 3: Simulated precipitation (in mm) for a model of a future warmer climate (red line in graph at left) and a model of the recent past (red line in graph at right), for a 3 x 3 grid centered on the grid box of the RCA 3 climate model that contains Forsmark. In both graphs, the solid green line shows local observed data for the recent period 1961–1990. Dashed lines indicate spatial variability in the 3 × 3-grid, representing ±1 standard deviation calculated from the 9 grid boxes. The gray area represents the absolute maximum and minimum of the 9 grid boxes. The solid blue lines for the future warm climate represent a ±1 standard deviation of the spatial variation from for three additional simulations for the 21st century. Excerpted from Figure 3-36 of SKB (2014) and Figure 4-7 of Kjellström et al. (2009).

Figure 4: Predicted snow cover (in meters) for a model of a future warmer climate (red line in graph at left) and a model of the recent past (red line in graph at right), for a 3 x 3 grid centered on the grid box of the RCA 3 climate model that contains Forsmark. Dashed lines indicate spatial variability in the 3 × 3-grid, representing ±1 standard deviation calculated from the 9 grid boxes. The gray area represents the absolute maximum and minimum of the 9 grid boxes. Excerpted from Figure 3-36 of SKB (2014) and Figure 4-7 of Kjellström et al. (2009).

3. Potential future irrigation demands

To predict potential future agricultural water demand in the Forsmark area, we first consider which types of crops could reasonably be grown in the area in the predicted future climate, then consider the water demands of those crops and the fraction of arable land.

3.1. Climate constraints on future crops

A simple and practical way to do this is to consider what crops are grown presently in areas that have similar climates, especially in terms of the predicted annual temperature variation and length of growing season.

Based on the models of Kjellström et al. (2009), the future warmer climate at Forsmark is predicted to have average monthly temperatures and precipitation similar to the Alsace-Lorraine region of France around Nancy (Figures 5 and 6), in terms of having short winters with mean temperatures around zero Celsius, and moderately warm summers. The Leipzig area in central Germany also has a similar annual temperature range but receives less precipitation overall, particularly in the winter months.

Both Nancy and Leipzig have relatively long growing seasons compared with present-day Forsmark, typically starting in mid-April when mean daily temperatures rise above 10 C (about a month earlier than typical for the Uppland region) and lasting for about 200 days into late October (about 50 days longer than the growing season in Uppland).

This allows production of crops that require a longer growing season such as sugar beets, soybeans, maize (corn), and a wide variety of vegetables including melons and tomatoes, along with shorter-season crops that are commonly grown in Uppland such as small grains (barley, oats, and wheat), rapeseed, and potatoes. Long-season forage crops for livestock, such as alfalfa, are also possible to grow. The milder winters in these regions, with average temperatures close to or barely below freezing, also permit cultivation of semi-hardy fruit trees, nut trees, and wine grapes, although not frost-sensitive fruits such as citrus, peaches, apricots, or olives.

The predicted cumulative precipitation during the growing season is plotted in Figure 7. Even for relatively dry years in the predicted future warmer climate, the cumulative precipitation over the length of the growing season is greater than for the present-day climate at Forsmark, but could be less than that for Nancy, France or Leipzig, Germany in the present.
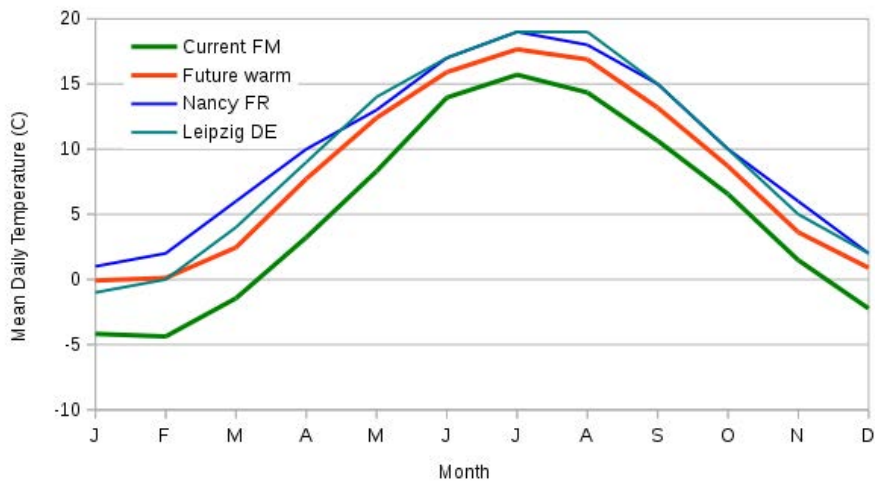
Figure 5: Comparison of present and future warm-climate temperatures around Forsmark (Kjellström et al., 2009), versus present-day temperatures in the Alsace-Lorraine regions (Nancy FR) and central Germany (Leipzig, DE).
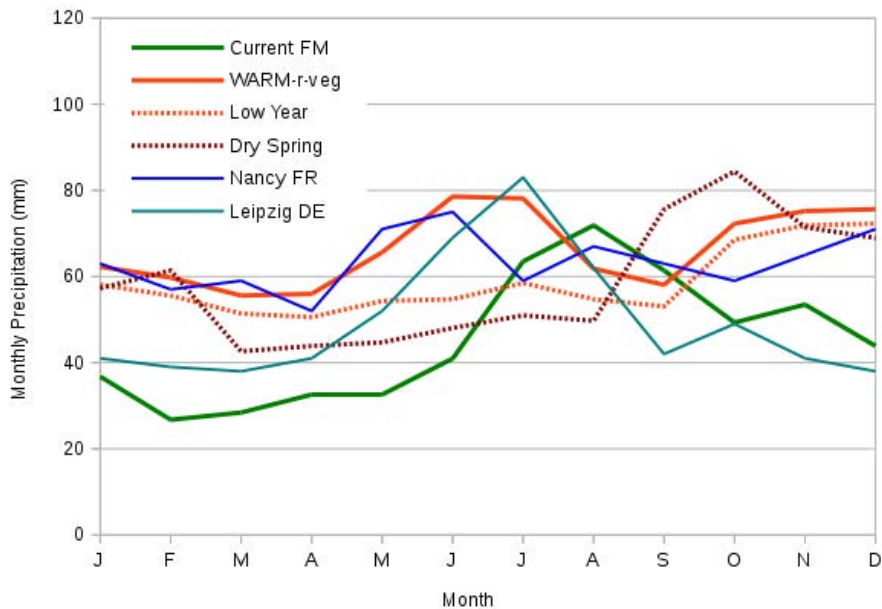
Figure 6: Comparison of present and future warm-climate precipitation around Forsmark, versus present-day precipitation in the Alsace-Lorraine regions (Nancy FR) and central Germany (Leipzig DE). Future warm-climate predictions are shown for the model case WARM-r-veg mean results (Kjellström et al., 2009), as well as two illustrative cases with lower precipitation: A "low year" based on the lower bound of annual variation given by (Kjellström et al., 2009) and a year with a relatively dry spring and summer.

15
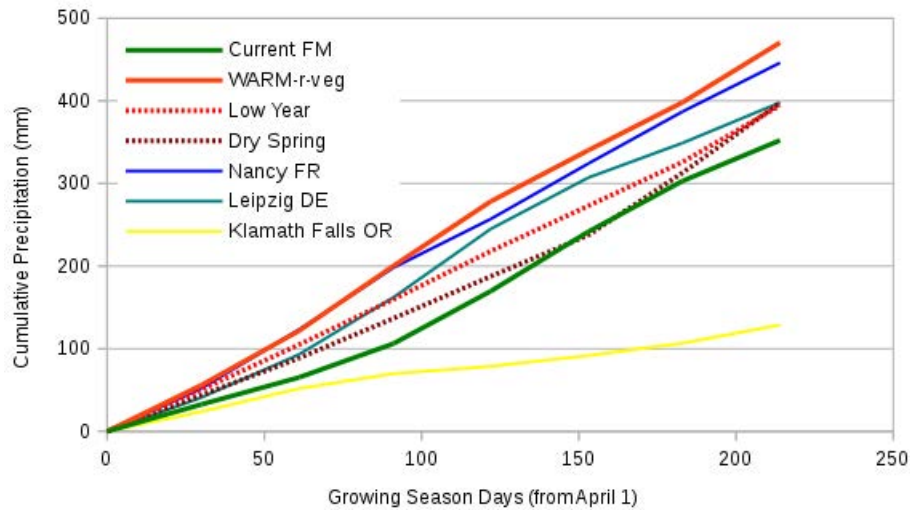
Figure 7: Comparison of present and predicted future warm-climate precipitation during the growing season around Forsmark, versus present-day precipitation in the Alsace-Lorraine regions (Nancy FR) and central Germany (Leipzig DE). Future warm-climate predictions are shown for the model case WARM-r-veg mean results (Kjellström et al., 2009), as well as two illustrative cases as in Figure 6 (dotted lines). In addition, data are shown for a semi-arid region in the western United States of America (Klamath Falls OR) where agricultural production depends primarily on irrigation.

3.2. Seasonal water requirements for potential crops

Table 3 gives examples of seasonal water requirements for various crops that could be viable for production in the predicted future warm climate at Forsmark. From this tabulation, it can be seen that the short-season crops typically grown in the Forsmark area today (such as barley, oats, potatoes, or peas) tend to have smaller water requirements when compared to longer-season crops such as sugar beets, maize and alfalfa.

The crop water needs listed in Table 3 can be compared with the predicted cumulative precipitation during the growing season as plotted in Figure 7. It can be noted that the present-day precipitation at Forsmark is adequate for a few short-season crops such as peas, but marginal to inadequate for other crops currently grown on a small scale in the region, such as barley and potatoes, if not for retained soil moisture from late-spring snow-melt, supplemented in some cases by irrigation from wells or surface-water resources. For the longer-season crops that would become possible in a future, warmer climate, irrigation could be a necessity.

Table 3: Seasonal crop water needs for selected crops that could be viable in the Forsmark area for a future warmer climate. Values taken from Brouwer and Heibloem (1986). Minimum values generally correspond to crop requirements in relatively cool, humid climates while the maximum values correspond to hotter and less humid conditions, with more rapid evapotranspiration.

Crop	Water need over growing period	
	Minimum (mm)	Maximum (mm)
Alfalfa	800	1600
Maize	500	800
Tomato	400	800
Sugarbeet	550	750
Potato	500	700
Soybean	450	700
Barley/Oats/Wheat	450	650
Melon	400	600
Onion	350	550
Bean	300	500
Pea	350	500

3.3. Potential irrigation well requirements

Effective precipitation P_e available for crops is generally less than the total precipitation P due to the combined effects of runoff, infiltration below the root zone, and surficial evaporation of light precipitation. For monthly precipitation in the range P = 50 mm/month to 80 mm/month, effective precipitation is typically in the range $0.4P$ to $0.5P$ (Brouwer and Heibloem, 1986).

Based on this approximation, and considering crops such as alfalfa, maize or tomatoes as realistic possibilities for a warmer future climate, the growing-season water deficit could be 600 mm or more, leading to an annual demand of 6×10^6 litres per hectare of cropland, or roughly 30,000 L/ha per day, for a nominally 200-day growing season.

Irrigation efficiency ranges from around 60% to 90% depending on the method used for water application. For 75% efficient irrigation, the amount of water needed would be 40,000 L/ha per day. The corresponding pumping rate required for an irrigation well would be 28 L/min per hectare of irrigated cropland served by that well.

This projected water demand for intensive cultivation of long-season crops is very high in relation to the well scenarios considered in the SR-PSU safety assessment. Öhman and Vidstrand (2014) considered wells with a daily pumping rate Q_{well} = 700 L/d as representative of the type of well that could supply a single household with a subsistence garden plot. Intensive cultivation of long-season crops could require groundwater extraction at nearly 60 times that rate, per hectare.

However, this rate of extraction could be feasible for wells that are favorably located, particularly wells drawing from high-permeability fracture zones. Modelling results by Öhman and Vidstrand (2014) indicate that steady-state flows from 7600 up to 213,000 L/d could be sustained by wells located near future arable land at Forsmark (Figure 8). A well with capacity in the middle of this range would be sufficient to irrigate 2 ha of crop land, and a high-producing well would be sufficient to irrigate 5 ha.
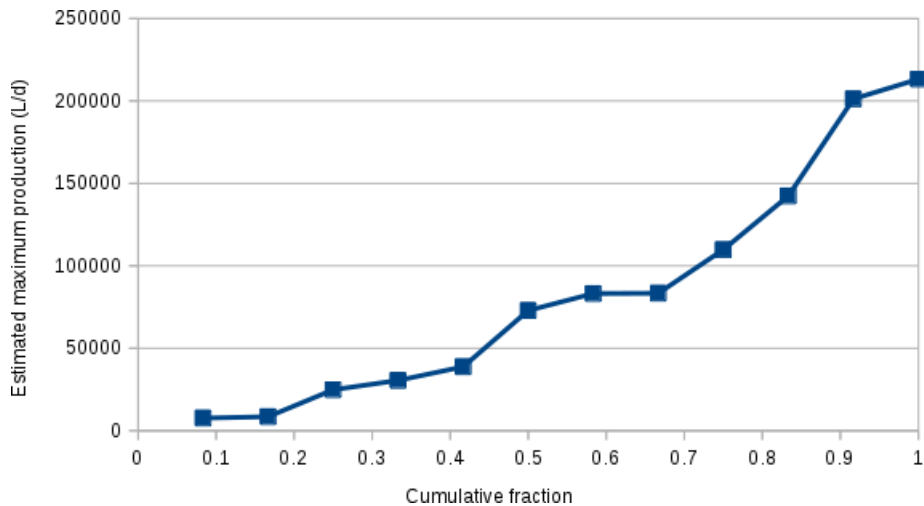
Figure 8: Estimated maximum production for a sample of 12 wells located near future arable land at Forsmark. Based on calculated data given in Table 4-1 of Öhman and Vidstrand (2014).

3.4. Potential agricultural demand for groundwater

The amount of future irrigated crop land in the Forsmark area is limited by the distribution of suitable regolith types (Figure 9) and regolith depth (Figure 10). For mechanized farming methods presently used in regions with climates similar to the predicted warmer future climate at Forsmark, crops would likely be limited to clayey till, peat, clayey silt, and clay, and excluding more rocky strata such as boulder-rich till, sand/shingle or glaciofluvial deposits.

The minimum regolith depth depends on the type of crop. Peas and small grains such as wheat and barley typically have effective root zones less than 1 m deep, but for soybeans and alfalfa, this can be close to 1.4 m, with maximum root depths approaching 2 m (Fan et al., 2016). Thus cultivation of the more water-intensive types of crops considered here would likely be limited to areas with regolith at least 2 m deep.

From visual inspection of Figures 9 and 10, most of the area near the present-day Baltic coastline would have regolith of suitable type and depth for such crops. Graphical analysis of a 2 km x 11.5 km rectangular strip along the coastline, as part of this study, indicated that 59% would be arable according to these criteria. Taking a value of 60% as a round value, and If this land is all utilized for crop production, the spatially averaged water usage for irrigation would be:

(40 000 L/ha per day) x 60% = 24,000 L/ha per day

A 0.5 km wide strip of land stretching for 1 km along the coast, farmed and irrigated at this rate, would require pumping 1.2×10^6 L/d (14 L/s), likely drawing water from multiple wells.
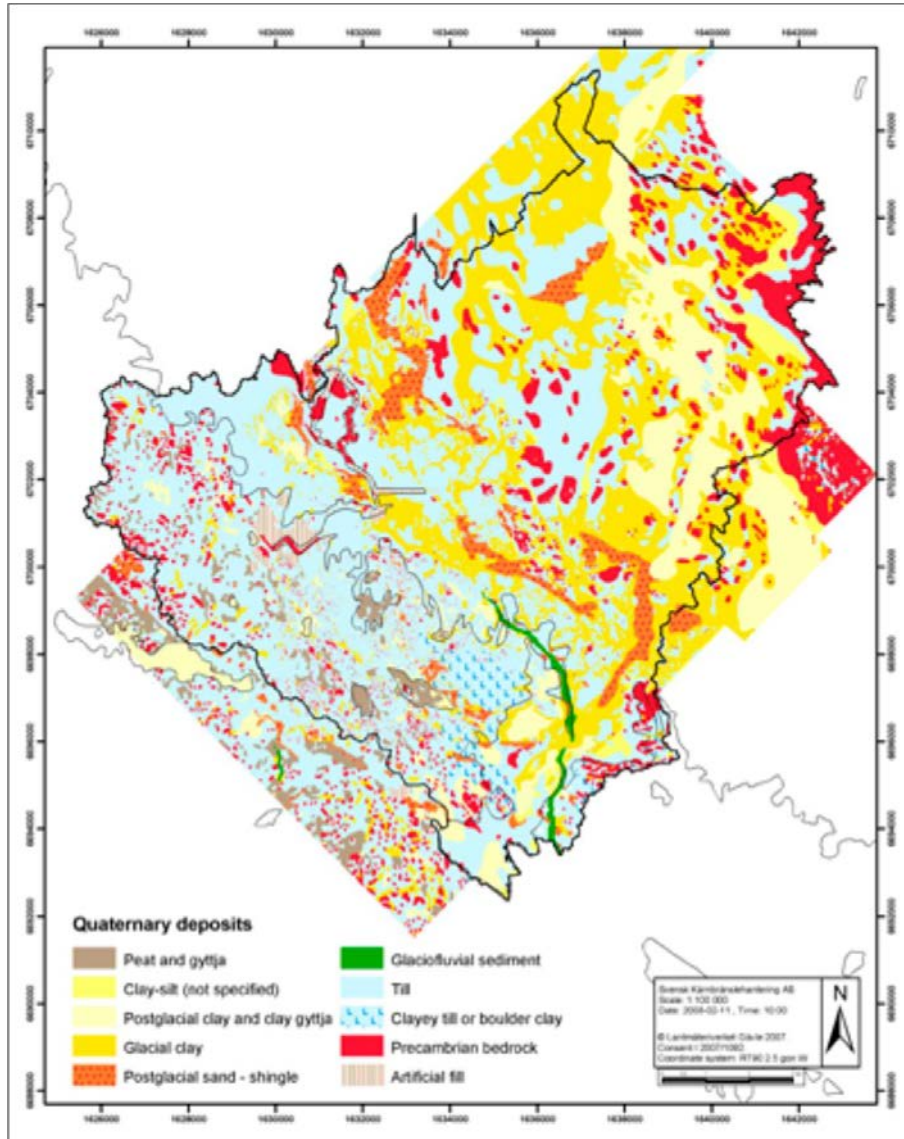
Figure 9: Distribution of Quaternary deposits in the Forsmark area, including areas presently covered by lakes, streams, or the Baltic. From Figure 2-14 of Hedenström et al. (2008).
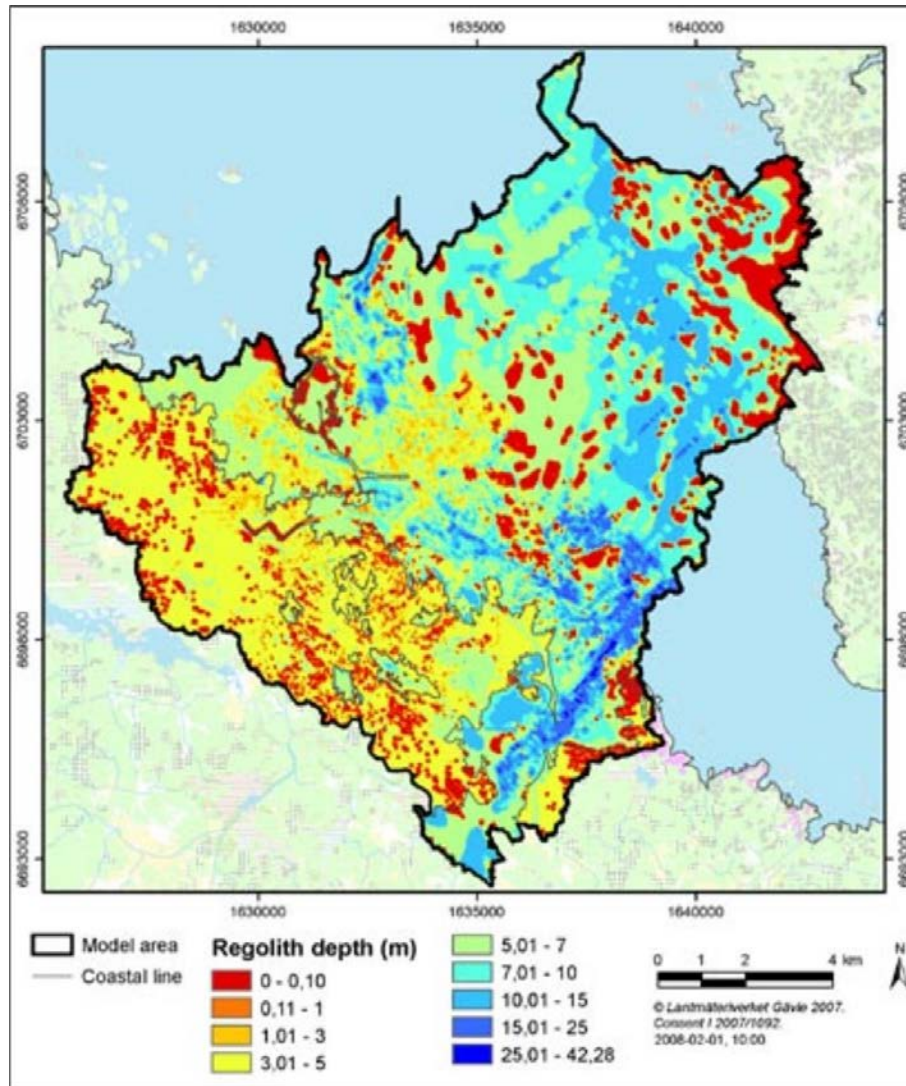
Figure 10: Estimated regolith depth at Forsmark. From Figure 4-1 of Hedenström et al. (2008).

This can be compared with the natural seaward flow of groundwater driven by the local topographic gradient. As a simple calculation based on Darcy's law:

$$Q = -K_r \, A \, \Delta h / \Delta L$$

using a nominal hydraulic conductivity for the shallow fractured bedrock of $K_r = 1.5 \times 10^{-6}$ m/s (Bosson et al., 2010) and a topographic gradient:

$$\Delta h / \Delta L = (-25 \text{ m}) / (5 \text{ km}) = -0.005$$

the natural seaward flow through the uppermost 50 m of fractured bedrock under such a strip would be:

$$Q = (1.5 \times 10^{-6} \text{ m/s}) (50 \text{ m}) (1000 \text{ m}) (-0.005) (1000 \text{ L/m3}) \approx 0.4 \text{ L/s}$$

Thus groundwater extraction for irrigation at this rate would be about 40 times the natural seaward flow. Such a high rate of extraction would require substantial

drawdown of the local water table, and might not even be possible. Even a 25 m drawdown across the farmed coastal strip, leading to a local gradient:

$$\Delta h/\Delta L = (-50 \text{ m}) / (5 \text{ km}) = -0.010$$

would at best double the flow of groundwater originating as meteoric precipitation from inland. This simple calculation indicates that the amount of land and type of crops that could be irrigated in a future warmer climate at Forsmark will ultimately be limited by the hydraulic conductivity of the shallow bedrock, which limits long-term flows to irrigation wells.

Future agriculture, under this scenario, would be limited by groundwater availability, either to a smaller fraction of the arable area, or to crops that require less water during the growing season. This practical limit would be reached when groundwater exploitation is maximized by sustained pumping of multiple wells that produce local drawdowns approaching the depth of the relatively conductive, shallow bedrock.

4. Potential for future saline intrusion

Groundwater extraction in coastal situations may lead to saline water intrusion. As illustrated conceptually in Figure 11, drawdown of freshwater in the upper part of a coastal aquifer allows inland migration of the freshwater/saltwater interface, and local upconing of the denser saline waters toward pumped wells. This phenomenon has been documented in numerous coastal situations around the world. Relevant examples from temperate situations are summarized below.
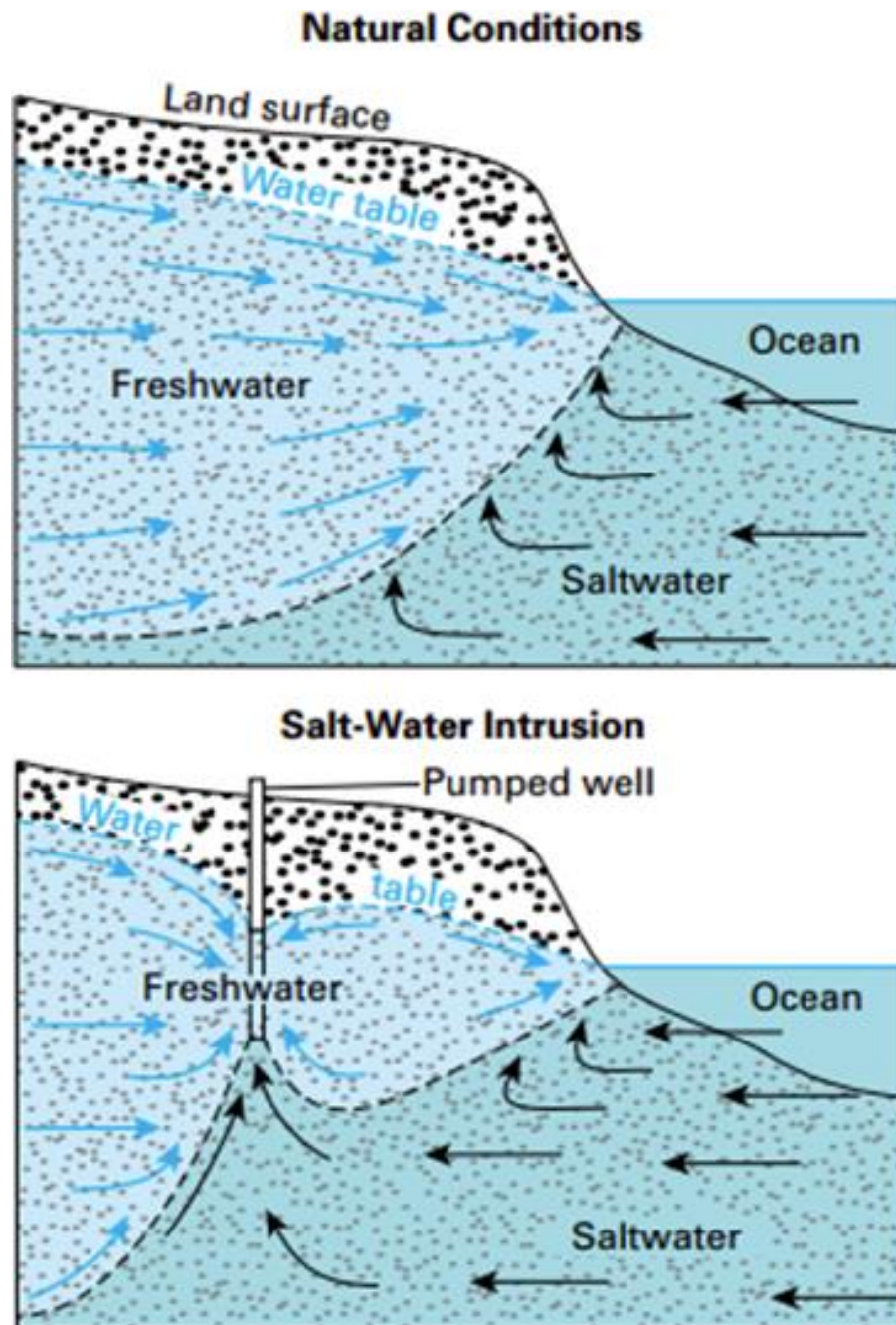
Figure 11: Conceptual illustration of salt-water intrusion due to groundwater extraction in a coastal aquifer (illustration from U.S. Geological Survey).

4.1. Temperate examples of salt-water intrusion

Examples of salt-water intrusion from temperate climates include the coast of Laizhou Bay southeast of Beijing (Wu et al., 1993) and multiple locations along the coast of the United States and Canada (Barlow and Reichard 2010). Most of these cases are in coastal plains with deep, unconsolidated sediments and/or sedimentary aquifers, including Laizhou Bay as well as coastal regions of and New York and New Jersey on the Atlantic coast of the United States.

Salt-water intrusion is a long-standing issue in The Netherlands, where the subject has been studied extensively and has motivated fundamental scientific understanding of the topic (including development of the Ghijben-Herzberg relation in the late 1880s, relating the water-table elevation to the depth of the freshwater–saltwater interface as a simple function of the relative densities). However the cause of salt-water intrusion in The Netherlands is due to the centuries-old practice of reclaiming low-lying lands from the sea, by a complex system of canals, polders, and wind-powered pumping stations (Oude Essink, 2001). This situation thus differs from the most likely factors driving future salt-water intrusion in the Forsmark area.

The Puget Sound region near Seattle, Washington, discussed briefly by Barlow and Reichard (2010), is similar to Forsmark in some respects. This region was also subject to continental glaciation within the last 15 ka, which left similar types of glacial and post-glacial deposits atop crystalline bedrock. Due to the restricted communication of Puget Sound with the ocean via a relatively narrow strait, daily tidal amplitudes are smaller than along the ocean coast (typically less than ±1.5 m), but still significantly greater than on the northern Baltic. Important hydrologic differences include much steeper topography with mountains up to 2000 m within 50 km of the shoreline, and very high annual precipitation (965 m/y in Seattle).

A survey of wells in coastal areas of Washington by Dion and Simioka (1984) found that salt-water intrusion around Puget Sound was typically localized and usually affected only individual wells, rather occurring as a broad front. Wells that developed high salinity were frequently abandoned, leading to uncertainty in the long-term persistence of salt-water intrusion.

The Florida carbonate aquifer of north-eastern Florida and south-eastern Georgia, on the Atlantic coast of the United States, is an example of more strongly heterogeneous rock in which vertical flow along fracture zones has allowed salt water to move upward from deeper, saline aquifers into shallower aquifers where water-supply wells are located (Barlow and Reichard, 2010). The role of strong heterogeneity governed by fracture zones, in otherwise relatively low-permeability bedrock, is in some ways analogous to the expected role of the system of subhorizontal and subvertical fracture zones at Forsmark.

However the causes of salt water intrusion in this area are complicated by a network of canals for surface-water drainage which have significantly lowered the regional water table. Furthermore these canals have sometimes acted as a route for direct infiltration of seawater to the unconfined surficial aquifer during storm surges from hurricanes and tropical storms of lesser magnitude, prior to the late 1940s when water control structures were installed. Such a situation is not expected for the future climate scenarios for Forsmark.

Thus none of the examples found in this survey of the literature are directly comparable to the situation predicted for Forsmark over the next 500-1000 years.

The situation around Puget Sound in the state of Washington may be most similar in terms of future agricultural and domestic use being limited and affected by salt-water intrusion, in an area with shallow crystalline basement overlain by glacial/postglacial deposits and with limited tidal influence. However there are significant differences in annual precipitation and topographic gradients.

4.2. Influence of rising sea levels on salt-water intrusion

Salt water intrusion near Forsmark could potentially be driven by rising sea levels caused by melting of land ice and thermal expansion as the global climate continues to warm in the near future.

Pimenoff et al. (2012) predicted a maximum global mean sea level rise of 1 m over the next 500 years, based on consideration of a range of carbon-emissions scenarios. The corresponding annual rate of sea level rise (2 mm/y) would be more than offset by ongoing land uplift at a rate of ca. 7 mm/y (SKB TR-13-05).

Pimenoff et al. (2012) note that the climate models used in their analysis did not consider potential collapse of the Antarctic ice sheet, so their evaluation of future sea level rise may not be fully conservative. However modelling by Chang et al. (2011) indicates that the effect of rising sea level is transient for confined aquifers, if the ambient recharge remains constant, because eventually the groundwater field farther inland adjusts to the point where the freshwater drives the fresh/salt-water interface back to its original position.

Thus even if the rate of sea level rise in the next 500 years (when climate change is expected to be fastest) is enough to outstrip the rate of land rise, this is not likely to produce long-term salt water intrusion.

5. Conclusions

Predicted future climates for realistic global warming scenarios can be expected to produce higher mean monthly temperatures, longer growing seasons, and reduced or negligible snow accumulations during a shorter winter season.

Models of future climate for these situations generally predict enhanced precipitation on average, rather than drier conditions. However the expected longer growing season may lead to significant shortfalls in natural precipitation, for crops suitable to the expected future climate. Compared with crops currently cultivated in the region today, the most important difference might be a longer growing season with consequent greater need for water.

Intensive cultivation and irrigation of such crops using well water would likely exceed the available groundwater resources. The degree of local groundwater drawdown depends on the extent of exploitation. However future irrigation demands clearly could exceed the natural coastward flow of freshwater, even if only part of the arable land is cultivated.

Local drawdowns due to intensive irrigation would draw water from the direction of the Baltic, eventually leading to inland movement of brackish water as well as upconing of the deeper brines. Such intensive water use would ultimately be limited by severe salt-water intrusion, leading to abandonment of wells with high salinity.

On this basis, and considering similar cases in the Puget Sound region of Washington, USA, it is reasonable to expect that future withdrawals of groundwater in a future warmer climate will proceed until intrusion of saline water leads to local abandonment of wells. Such practices could maintain saline conditions in the current SFR and its proposed extension, indefinitely into the future, and therefore should be considered in the safety assessment.

6. References

Barlow, P.M., and Reichard, E.G., 2010. Saltwater intrusion in coastal regions of North America. *Hydrogeology Journal* v. 18, no. 1, p. 247–260.

Brandefelt, J., Zhang, Q., Hartikainen, J., and Näslund, J-O., 2013. The potential for cold climate conditions and permafrost in Forsmark in the next 60,000 years. SKB TR-13-04, Svensk Kärnbränslehantering AB.

Brouwer, C., and Heibloem, M., 1986. Irrigation Water Needs. Irrigation Water Management Training Manual No. 3. Food and Agriculture Organization of the United Nations, Rome, Italy.

Chang, S.W., Clement, T.P., Simpson, M.J., and Lee, K.K., 2011. Does sea-level rise have an impact on saltwater intrusion? Advances in Water Resources, v. 34, no. 10, p. 1283-1291. https://doi.org/10.1016/j.advwatres.2011.06.006

Dion, N.P., and Simioka, S.S., 1984. Seawater intrusion into coastal aquifers in Washington, 1978. Water-Supply Bulletin 56, Washington Department of Ecology, Olympia, Washington, USA.

Fan, J., McConkey, B., Hong, W., and Janzen, H., 2016. Root distribution by depth for temperate agricultural crops. Field Crops Research v. 189, p. 68–74. http://dx.doi.org/10.1016/j.fcr.2016.02.013.

Geier, J., 2019. Assessment of transport parameters and hydrogeological aspects of future human actions. SSM report 2019:16, Strålsäkerhetsmyndigheten, Stockholm.

Hedenström, A., Sohlenius, G., Strömgren, M., Brydsten, L., and Nyman, H., 2008. Depth and stratigraphy of regolith at Forsmark. Site descriptive modelling, SDM-Site Forsmark. SKB Report R-08-07, Svensk Kärnbränslehantering AB, Stockholm.

Kjellström, E., Strandberg, G., Brandefelt, J., Näslund, J.-O., Smith, B. & Wohlfarth, B., 2009. Climate conditions in Sweden in a 100,000 year time perspective. SKB Technical Report TR-09-04, Svensk Kärnbränslehantering AB, Stockholm.

Khublaryan, M. G., FrolovI, A. P., and Yushmanov, O. Seawater intrusion into coastal aquifers. *Water Resources* 35(3):274-286, doi: 10.1134/S0097807808030032

Odén, M., Follin, S., Öhman, J., and Vidstrand, P., 2014. SR-PSU Bedrock hydrogeology. Groundwater flow modelling methodology, setup and results. SKB R-13-25, Svensk Kärnbränslehantering AB, Stockholm.

Oude Essink, G.H.P., 2001. Salt water intrusion in a three-dimensional groundwater system in The Netherlands: A numerical study. *Transport in Porous Media* v. 43, p. 137–158.

Pimenoff, N., Venäläinen, A., and Järvinen H. 2011. Climate scenarios for Olkiluoto on a time-scale of 120,000 Years. Posiva Report 2011-4. Posiva Oy, Eurajoki, Finland.

Pimenoff, N., Venäläinen , A., and Järvinen, H., 2012. Climate and sea level scenarios for Olkiluoto for the next 10,000 years. Posiva Report 2012-26. Posiva Oy, Eurajoki, Finland.

Påsse, T., 2001. An empirical model of glacio-isostatic movements and shore-level displacement in Fennoscandia. SKB R-01-41.

SKB, 2014. Climate and climate-related issues for the safety assessment SR-PSU. Technical Report TR-13-05. Svensk Kärnbränslehantering AB, Stockholm.

Sohlenius, G., Strömgren, M, and Hartz, F., 2013. Depth and stratigraphy of regolith at Forsmark. SR-PSU Biosphere. SKB R-13-22, Svensk Kärnbränslehantering AB, Stockholm.

Werner, K., Sassner, M., and Johansson, E., 2013. Hydrology and near-surface hydrogeology at Forsmark –synthesis for the SR-PSU project. SKB R-13-19, Svensk Kärnbränslehantering AB, Stockholm.

Wu, J., Xue, Y., Liu, P., Wang, J., Jiang, Q., and Shi, H., 1993. Sea-Water Intrusion in the Coastal Area of Laizhou Bay, China: 2. Sea-Water Intrusion Monitoring. *Ground Water* 31(5):740 - 745. DOI: 10.1111/j.1745-6584.1993.tb00845.x

Öhman J, Vidstrand P, 2014. SR-PSU Bedrock hydrogeology. TD12 – Water-supply wells in rock. SKB P-14-05, Svensk Kärnbränslehantering AB.

2019:16

The Swedish Radiation Safety Authority has a
comprehensive responsibility to ensure that
society is safe from the effects of radiation.
The Authority works to achieve radiation safety
in a number of areas: nuclear power, medical care
as well as commercial products and
services. The Authority also works to achieve
protection from natural radiation and to
increase the level of radiation safety
internationally.

The Swedish Radiation Safety Authority works
proactively and preventively to protect people
and the environment from the harmful effects
of radiation, now and in the future. The Authority
issues regulations and supervises compliance,
while also supporting research, providing
training and information, and issuing advice.
Often, activities involving radiation require
licences issued by the Authority. The Swedish
Radiation Safety Authority maintains emergency
preparedness around the clock with the aim of
limiting the aftermath of radiation accidents
and the unintentional spreading of radioactive
substances. The Authority participates in
international co-operation in order to promote
radiation safety and finances projects aiming
to raise the level of radiation safety in certain
Eastern European countries.

The Authority reports to the Ministry of the
Environment and has around 300 employees
with competencies in the fields of engineering,
natural and behavioural sciences, law, economics
and communications. We have received quality,
environmental and working environment
certification.